Technology
ystems and Electric Drives

TECHNISCHE UNIVERSITÄT WIEN
Vienna University of Technology

DISSERTATION

Sensorless Rotor Magnet Temperature Estimation of Permanent Magnet Synchronous Motors

wissenschaftliche Arbeit zur Erlangung des akademischen Grades eines
Doktor der technischen Wissenschaften (Dr. techn.)

unter der Leitung von
Ao. Univ. Prof. Dipl.-Ing. Dr. Thomas Wolbank

eingereicht an der Technische Universität Wien
Fakultät für Elektrotechnik und Informationstechnik

von
Dipl.-Ing. Martin Dimitrov Ganchev
Matrikelnummer: 9726585

1. Gutachter: Prof. Dr. Thomas Wolbank
2. Gutachter: Prof. Dr. Gojko Joksimović (University of Montenegro)

Wien, im November 2013

Abstract

Owing to their high power density, good efficiency and high dynamics, permanent-magnet synchronous machines (PMSMs) find increasing acceptance in the industry, energy generation and in electric and hybrid-electric vehicles applications. The most widely-used rare-earth magnet in PMSMs is neodymium-iron-boron (NdFeB) since it is characterized with high energy density. However, neodymium magnets reveal very low thermal stability which is predominantly expressed is lower remanence flux density and reduced intrinsic coercivity upon temperature increased. Since the magnets in a PMSM are exposed to high temperature differences, an online monitoring of the magnet temperature becomes very meaningful in order to increase the quality of control and the reliability of the machine. Due to rotation, direct measurement of the magnet temperature is an inherently cumbersome task associated with high additional costs. In the current thesis, a method for estimating the magnet temperature in (PMSM's) without using any temperature sensors is proposed. The method presents a robust and inexpensive solution to monitor the magnet temperature in the motor under normal operation. The main idea is based on exploitation of saturation effects in the d-axis of the steel stator core that are produced by the d-current, the q-current and the rotor flux excitation. Procedures are proposed where by meaningful application of the voltage pulses in the d-axis of the motor, the resulting d-current response is made function of the magnetization level of the magnets. Thus, a temperature dependent variation in the magnetization level of the permanent magnets is reflected in a variation of the d-current slope.

The analytical discussions and the corresponding experimental validation are successively introduced. First, a magnet temperature monitoring based on a single positive voltage pulse in the d-axis of the motor and zero load current is investigated. This approach is generally valid and applicable in control setups where the motor speed varies in a narrow range. For applications characterized by wider speed range, a speed compensation approach is developed that implies a combination of a voltage pulse in the positive and negative d-axis of the motor, whereby a symmetry of speed dependent induced voltages can be achieved in a manner that the difference of the d-current responses from the positive and negative pulse is not affected by the motor speed. Finally, under consideration of cross-saturation effects and the influence of the q-current on the d-current response, a q-current compensation approach is introduced and temperature monitoring under various load conditions is demonstrated.

Contents

1 Introduction – State of the Art

Electric motors account for about 40% of the total electricity consumption, which implies that almost every second power station produces energy solely for electric motor driven systems. Therefore, every step to increase the energy-efficiency of electric motors or of electric motor driven systems contributes greatly to the reduction of the global energy consumption. For example, according to a working paper of the International Energy Agency (IEA), by improving the efficiency of electric motors by 1%, the annual electricity demand would decrease in the order of 75TWh, [1]. At present, the most common type of electric motors is AC induction machine (IM). These are cheap, robust, easy to maintain and the first choice to operate pumps, fans, compressors and conveyors at fixed speed. Another big advantage of the induction motors is their excellent overloading and field weakening capability. Furthermore IMs are greatly standardized in terms of frame size, output torque, speed, insulation, and protective coatings. For this type of machines there exists clear international energy-efficiency testing standard (IEC60034-2-1, September 2007). However, despite of their enormous benefits, IMs reveal a narrow scope for further energy-efficiency expansion as this is a very mature technology. Recent improvements imply the use of copper instead of aluminium for the conductor bars and end rings in rotors. This allows a gain of almost one efficiency class within the same frame size, however the manufacturing process adds considerable cost to the motor end user price, since it is much more difficult to cast copper in precise forms as the melting temperature of copper is 1083°C [1].

In many industrial applications and motor driven consumer products, there is still unexhausted potential for reduction of the power consumption by replacing IMs with more energy efficient motor technologies. In IMs, because of a fundamental operational principle, a part of the stator current is required to induce rotor currents in order to produce rotor flux. From the energy efficiency point of view, this results in an inherent lagging power factor. In the last two decades, motor technology development has been rapidly moving towards machines using rotor permanent magnetization, referred to as permanent magnet (PM) machines. In general, due to the sinusoidal back EMF waveform, a counterpart of an induction motor is considered a permanent magnet synchronous motor (PMSM). In contrast to IM, in PMSM the rotor flux is produced by permanent magnets and does not need stator currents, which leads to reduced motor losses and a torque current ratio of 10% to 30% higher than a comparable induction motor,[2]. Due to their bigger power density and higher acceleration ratio, PMSMs are

already considered the first choice in motion control applications demanding high dynamics and as traction drives in electric and hybrid electric vehicles (E&HV). However, in most industrial applications PMSMs are still not considered mature alternative to IMs. The major drawbacks of PMSM, both of economical and technological character, are directly related with the permanent magnets.

High performance permanent magnets are made of alloys containing rare-earth elements. The mining process of rare earths is cost intensive and environmental damaging, and the found mineable deposits are concentrated in a few areas. Hereby, China posses 30 % of the world's rare earth metal deposits. The country has almost an exclusive market monopoly position since it produces more than 95% of the world's rare earth elements. Recently, China has repeatedly been introducing export quotas for rare-earth metals following protectionism economic policy for its own manufacturing industry. Thus, the world's production of PMSMs is nowadays strongly dependent of the Chinese magnet manufacturers. Rising concerns related to future supply shortage hinder a broader acceptance and distribution of PMSMs. Moreover, from technological point of view, a major concern in PMSM is the thermal stability of the permanent magnets together with performance degradations that occur due to oxidation or poor mechanical rigidity. However, by introducing fault prediction monitoring techniques, the reliability of PM drives can be continuously improved pushing further their utility.

The current thesis addresses the subject matter related to the thermal stability of permanent magnets in PMSM by presenting a novel robust method for estimation of the magnet temperature in a machine under normal operation.

1.1 Problem Outline

The magnet temperature influences significantly the performance of a machine since the remanence flux density of the magnet decreases when its temperature increases. This implies a decrease of the rotor flux excitation and consequently a decrease of the rotor flux linkage in a PMSM upon a temperature rise in the machine interior. A decrease of the rotor flux linkage will lead directly to lower electromagnetic torque output. In other words, the motor torque capability and the efficiency will vary with the temperature. This is a very undesirable fact that should be accounted for in the motor control, especially when the motor is designed and foreseen to work in a wide temperature operating range.

Neodymium magnets are due to their high energy density, the mostly widely used magnets nowadays in PM machines. Nevertheless the resistivity of these magnets is

relatively low giving rise to considerable eddy current losses especially when the motor is driven by pulse-width-modulated (PWM) inverter. In high torque and speed operation, eddy current and hysteresis losses are responsible for an abundant temperature rise in the magnets. This has been a subject of detailed investigation in the following works [3]–[10]. A pioneer work investigating directly the temperature effects in PM motors using neodymium magnets can be considered [11]. The paper reports an investigation on reduction of torque capability and efficiency upon rotor temperature increase for five PM motors characterized by different topologies. Assuming a nominal torque of 1 per-unit quantity (pu) at 20°C rotor temperature, at rotor temperature of -40°C the torque of the machines is given in the range of 1.03pu to 1.07pu at rated speed and current limit set to 1pu. At rotor temperature of 160°C the torque of the machines drops to values between 0.84pu and 0.88pu. Furthermore, in this temperature range the efficiency of the motors would vary up to 20%. Although the results originate from the year 1995, there is no significant improvement of these values and therefore they can be considered to a great extent exemplary.

From motor control point of view, in speed controlled PM drives a decrease of the rotor flux linkage is compensated by higher reference torque value provided by the speed controller, while in a torque controlled drive it leads directly to a lower torque output than the required one. Although this process is reversible with respect to the temperature, there are many torque control applications where a varying motor torque output is not acceptable. In torque controlled PM drives a constant nominal torque can be maintained when the reduction of rotor flux linkage is compensated by an additional stator current in the machine which depends on the degree of change of the rotor flux linkage. The compensation can be realized straightforward if there is a torque sensor available but usually this is not the case since such sensors are very expensive or impossible to be mounted due to their size. Another approach implies knowledge of the actual magnet temperature. Thus, by knowing corresponding demagnetization curves or the flux density temperature coefficient of the magnet, a relatively exact estimation of the degree of change of the rotor flux excitation can be obtained for a given temperature.

The knowledge of the magnet temperature is not only a control issue concerning the torque capability of the motor but also a safety issue. It is a fact that the magnet intrinsic coercivity H_{ci} is a function of the temperature itself, as its absolute value decreases while the temperature increases. Therefore, at higher temperatures, excessive currents in the machine can lead to irreversible demagnetization of the magnets [11]. In general, the machine design should ensure that no irreversible demagnetization will occur in the machine under the expected operating conditions, [12]. Considering both aspects,

constant torque output and prevention of irreversible demagnetization of the machine, it can be concluded that an online detection of the actual temperature level of the permanent magnets can significantly improve the performance, reliability, life cycle and exploitation of a PM machine.

1.2 State of the Art

Due to rotation, measuring directly the temperature of the permanent magnets is very cumbersome. The most common techniques include battery powered devices [13]–[22], infrared sensors, [23]–[26], and slip rings [27], [28]. Carrying out such measurements is rather expensive and their application is limited to laboratory and experimental setups since specific instrumentation is normally required. Recently, significant efforts have been performed to develop techniques which do not require any temperature sensors to obtain the rotor temperature in PM machines. Such techniques have been already reported in various papers. The most common approach is a thermal model of the machine. Thermal models imply good knowledge of the geometry, cooling system and especially on the material specific parameters, and therefore their application is rather limited to industrial usage with known environmental and operating conditions. Furthermore depending on the model complexity, accuracy and number of input parameters, a real-time execution, parallel to the motor control software routines, may require increased computing and data acquisitioning capability which can lead to additional hardware costs. Novel approaches and issues of PM machine thermal modelling are given and discussed in [29]–[41]. Another known approach to detect magnet temperature is a flux observer. This has been demonstrated in [42] for an interior permanent magnet synchronous motor (IPMSM). By observing the rotor flux, the amount of the demagnetization can be calculated and thus the rotor temperature. The main drawback of the proposed method, as stated by the authors themselves, is the necessity of precise acquisition of the machine's and the inverters' parameters [42] whereby the machine's non- linearity e.g. caused by saturation has to be taken into account. The nonlinear relation between current and flux is defined by a look-up-table (LUT). The accuracy of the method is extremely sensitive to the quality of acquisition of the terminal voltage of the machine. It characterizes further with decreased accuracy while load gets lower. Rotor flux observer based on Extended Kalman Filter (EKF) is presented in [43] for PM reluctance machine and PMSM. Here again the method sensitivity is strongly limited. It is dependent on exact prior knowledge of the motor parameters and how sinusoidal the back EMF is. An active parameter estimation method by using high frequency signal injection is demonstrated in [25], [26]. This

approach is based on changes in the high frequency stator and rotor resistances due to temperature variation and concludes indirectly the temperature level in the permanent magnets. The robustness and accuracy of the temperature estimation procedure is strongly influenced by the non-ideal behaviour of the inverter (dead time, dc link voltage variation etc.). Furthermore, the accuracy of method decreases when the difference between the stator windings and the magnet temperature increases which is normal at high dynamic drive applications. The demonstrated experimental validation has been carried out in the low speed range, with measurements done at maximum speed of 900rpm. Therefore, with the published results it is difficult to evaluate the degradation of the method accuracy at higher speeds.

In this context, the current thesis sets as an objective to demonstrate a novel robust technique for estimation the temperature of the permanent magnets in a PMSM.

1.3 Scientific Contribution of the Thesis

The new method proposes an original approach for magnet temperature estimation in a PM machine without using any additional sensors other than conventional current and rotor position sensors. The physical principles of the method together with its analytical formulation are given in the current work, backed by extensive experimental validation. The objective with respect to already existing methodologies is to achieve:

- higher accuracy and robustness
- wider applicability range
- easy implementation and integration in a space vector or other control routines
- lowest possible negative impact on the machine normal performance

The main idea of proposed magnet temperature estimation approach is to detect changes in the degree of saturation in the d-axis of the machine which are caused by variation in the magnetization level of the permanent magnets. These changes are reflected in the slope of the d-current response upon a voltage pulse in the d-axis of the machine. The thesis goes through different stages of development and research findings and demonstrates the method potential in terms of adjustability, implementation, and applicability. It gives an instruction set on method commissioning and tuning possibilities in order to achieve best possible results for a given machine. Furthermore, definitions of trade-offs, constraints and limitations are pointed out regarding data acquisitioning, computing capability and software implementation.

1.4 Outline of the Thesis

The thesis is structured in six chapters as described in the following.

In Chapter 1 main problems related to demagnetization effects due to temperature increase in PMSM are identified. State-of-art solutions for sensorless estimation of the magnet temperature in PMSM are given creating a context for the presented research efforts.

Chapter 2 gives a brief introduction into basic permanent magnet characteristic which are relevant to the subject matter of the current thesis. It gives insight in the material behaviour related to exposure to opposing external field and various operating temperatures as it is the case in PMSMs. It outlines major trends regarding the usage of permanent magnets in electrical machines.

Chapter 3 gives insight in the space vector theory for electrical machines since the analytical formulation and theoretical analyses of the proposed method are given in space vector quantities. It describes basic modelling approaches of PMSMs used further in Chapter 4 to describe analytically the machine behaviour upon voltage pulse generation. A short introduction into the field oriented space vector control for PMSMs is given too, since this is the control scheme used to demonstrate method feasibility and its integration in a motor control routine.

Chapter 4 describes basic aspects of the experimental setup before introducing in detail the three basic approaches of the proposed magnet temperature estimation procedure. The first approach is related to low speed or constant speed applications where the estimation of the magnet temperature is carried out by applying a single voltage pulse in the positive d-axis of the motor. The second approach considers applicability at a wider speed range where countermeasures are demonstrated to overcome undesired influence of the speed on the accuracy of the estimated temperature. The first two approaches require that the q-current is zero upon applying a voltage pulse in the d-axis of the machine while the third approach describes an estimation of the magnet temperature of PMSM under load conditions.

Chapter 5 is dedicated to realization issues related to the hardware and software implementation of the proposed magnet temperature estimation. It describes the motor test bench that has been specially built for the current investigation and proposes a software implementation for the magnet temperature estimation routines. Furthermore, it describes the design and assembly of a rotor temperature monitoring device that has

been used to validate the feasibility of the proposed temperature sensorless estimation technique.

Chapter 6 gives overall conclusions and discussions on various aspects of the proposed method including applicability and potential improvements.

2 Permanent Magnets – Global Behaviour

In the following a brief introduction into basic characteristics of permanent magnets is given. Reversible and irreversible demagnetization effects are discussed with respect to opposing external field and temperature variation. A summary of the mostly used permanent magnet materials in PM machines is presented.

2.1 Magnetization Characteristics

Permanent magnets have a small number of important characteristics that define the materials performance and capabilities. Flux density B versus magnetizing force H characteristic gives information on the parameters most commonly used in the magnetic circuit design of PMSM. Figure 2-1 demonstrates a linear B versus H loop for a permanent magnet.

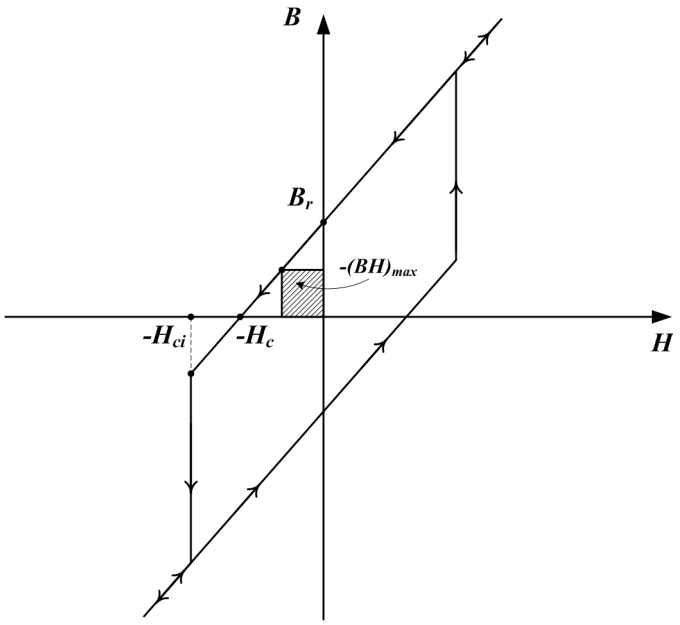

Figure 2-1: Magnetization characteristic of a magnet; Linear B versus H plot.

The magnitude of B when the magnetizing force is zero is called remanent flux density B_r or just remanence. H_c stands for the coercive force, also called coercivity, and is the magnetizing force required to reduce that the flux density to zero. One of the most important properties of a magnet is the so called intrinsic coercivity H_{ci}. It indicates the

maximum demagnetizing force that the magnet can withstand. Over the value $-H_{ci}$, magnetization of the magnet changes in the opposite direction. In a machine, a magnet operates predominantly in the second quadrant of the hysteresis loop between B_r and $-H_c$, commonly referred to as normal demagnetization curve.

Another important characteristic of a magnet is its maximum energy product $-(BH)_{max}$. The maximum energy product can be figuratively visualized by the largest rectangular that can be drawn under the demagnetization curve, as shown in Figure 2-1. It is a figure of merit that indicates the strength of the magnet and its ability to produce flux density in a given volume of space.

The flux density of a magnet is a result of the magnetizing force H and the intrinsic ability of the magnetic material to produce flux, referred to as intrinsic flux density B_i. A linear presentation of the B_i versus H plot is given in Figure 2-2. The second quadrant of the B_i versus H plot is known as intrinsic demagnetization curve. The intrinsic demagnetization curve crosses the B-axis at B_r, as the normal demagnetization curve, and the H-axis at the point of magnet intrinsic coercivity $-H_{ci}$. In the second quadrant the intrinsic demagnetization curve is always above the normal demagnetization curve, see Figure 2-3. The intrinsic and the normal demagnetization curve are related to each other through the equation $B_i = B - \mu_0 H$, where μ_0 is the magnetic constant (the magnetic permeability of vacuum), which has a value of 1 unity in the CGS system and a value of $4\pi\times10^{-7}$ Webbers/Ampere meter (Wb/Am) in the SI system. The normal demagnetization curve of a magnet is primarily used in designing the motor air gap and the magnetic circuit, while the intrinsic demagnetization curve is used to determine how the magnet intrinsic magnetization changes due to temperature variation or when the magnet is exposed to external opposing field. Measurements of a normal and intrinsic demagnetization curve are demonstrated for example in [44], page 20.

An intrinsic demagnetization curve of a real magnet does not contain an abrupt change at $-H_{ci}$ but a gradual transition that looks like a knee in the curve, as shown in Figure 2-3. The location of the knee is of great interest to the motor designer since beyond the knee point the magnet starts to lose magnetization permanently. By reaching $-H_{ci}$ the magnet is considered fully permanently demagnetized, there is no spontaneous magnetization and $B_i = 0$. Therefore, to keep the normal demagnetization curve linear, without occurrence of a knee in the second quadrant, it is very desirable when $-H_{ci}$ is moved out into the third quadrant, as in Figure 2-1 and Figure 2-3, ($|-H_{ci}| > |-H_c|$).

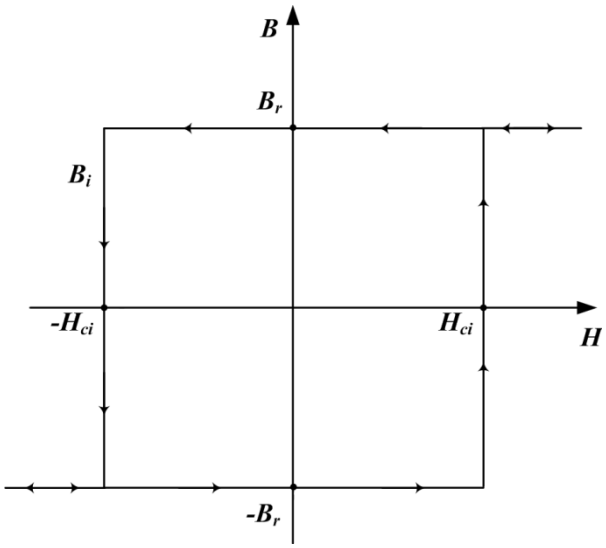

Figure 2-2: Intrinsic magnetization characteristic; linear presentation.

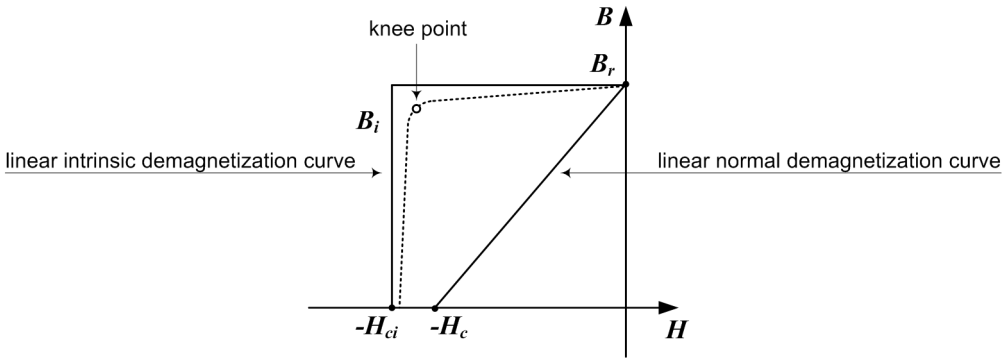

Figure 2-3: Intrinsic demagnetization curve versus normal demagnetization curve of a magnet; linear presentation.

2.2 Magnet Operation at Constant Temperature

Assuming a constant temperature, the magnetization characteristics of a magnet can be considered constant. In Figure 2-4, the point $\boldsymbol{a}$ on the normal demagnetization curve represents the actual working point of the magnet in the absence of external field. This is the intersection of the magnet load line and the normal demagnetization curve. The slope of the load line is denominated $P_c = \mathrm{B}/\mu_0 H$, commonly referred to as permeance coefficient. It is determined by the magnetic circuit and the shape of the magnet. The permeance coefficient P_c becomes smaller when the ratio between the length of the

magnetization direction (thickness of the magnet) and the surface area of a pole decreases. Furthermore, the magnet operating point is influenced by the air gap and the leakage flux of the circuit. A smaller air gap or a longer magnet, or a reduced leakage flux will generate a move from $\boldsymbol{a}$ to $\boldsymbol{c}$ along the demagnetization curve, as demonstrated in Figure 2-4. In order to reflect performance on the intrinsic demagnetization curve, a vertical is drawn from $\boldsymbol{a}$ as shown in Figure 2-4. The crossing point with the intrinsic demagnetization curve occurs at point $\boldsymbol{b}$, whereby the load line drawn from the origin to $\boldsymbol{b}$ has a slope $P_{ci} = B_i/\mu_0 H$ which is equal $P_c + 1$ when there is no externally applied field. The slope P_{ci} is referred to as intrinsic permeance coefficient.

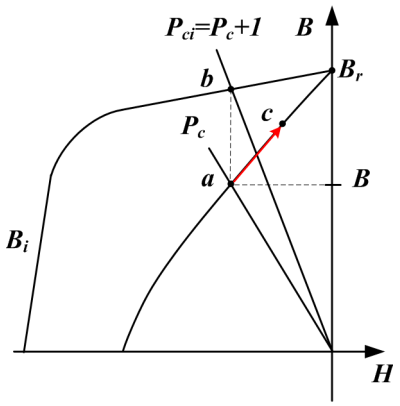

Figure 2-4: Operating point and load line for a magnet in the absence of external field.

2.2.1 Reversible Demagnetization upon External Field

The flux density of a magnet changes in the presence of an external field. In order to predict the degree of change, both the normal and the intrinsic demagnetization curves of the magnet material are required, [44], [45]. The intrinsic permeance coefficient P_{ci} is determined solely by the magnetic circuit topology, however it considerably affects the performance of the magnet in the presence of external field. By exposing the magnet to an opposing external field $-H_e$, the load line moves sideway but it preserves its slope, as depicted in Figure 2-5. The intersection point $\boldsymbol{c}$ of the new load line with the intrinsic demagnetization curve is projected down to the normal curve in order to obtain the new level of flux density and consequently the resulting loss ΔB due to the external field. Upon removal of $-H_e$, no change in the intrinsic magnetization will occur, since the point of intersection with the intrinsic demagnetization curve $\boldsymbol{c}$ is above the knee point in the example demonstrated in Figure 2-5. Although in a real magnet the intrinsic flux density B_i will change upon the external field $-H_e$, this change is reversible as

long as ***c*** is above the knee point. Under dynamic magnet operation, upon applying and removal of $-H_e$, the magnet operating point moves between ***b*** and ***c***. The portion of the curve between the points is called recoil line. A recoil line is indeed a very narrow loop but it is a useful approximation to consider it as a line, as proposed in [46].

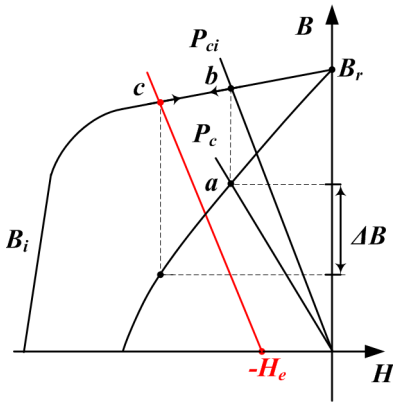

Figure 2-5: Operating point and load line shift for a magnet in the presence of external field.

2.2.2 Irreversible Demagnetization Due to External Field

Shifting or changing the slope of the load line in a way that the intersection with the intrinsic demagnetization curve is under the knee point leads to permanent change of B_i. The process is known as irreversible demagnetization. This is demonstrated in Figure 2-6. A load line is shifted due to an external field or its slope is changed by changing the magnetic circuit geometry so that the operating point moves from ***a*** to ***b*** where ***b*** is beyond the knee point, the change in B_i is permanent. Upon removal of the load line disturbance, the magnet returns not to ***a*** but to operating point ***c***. Subsequent application and removal of the load line disturbance will cause the magnet to operate reversibly along the new recoil line between point ***b*** and ***c*****,** as described more detailed in [46] page 93 paragraph 2.

Once irreversible loss has occurred, restoring the original level of B_i for a given magnet can be achieved only by fully remagnetization of the material. However, remagnetization is reasonable only if the load line disturbance that has caused the irreversible change of B_i, is considered abnormal with respect to the expected magnet operating conditions. Otherwise, the magnet is considered cycled and stabilized at a reduced energy for a given external field maximum level that can occur under normal operation.

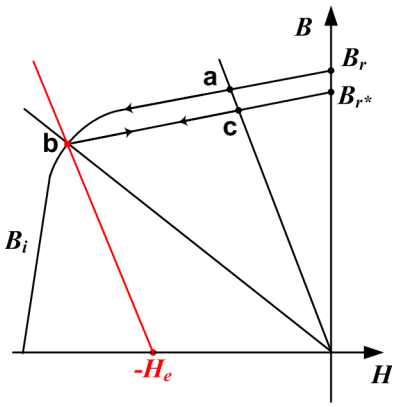

Figure 2-6: Change in operation with load line slope or position; occurrence of irreversible demagnetization; source [46] page 94, Figure 4.10.

2.3 Magnet Operation under Varying Temperature Conditions

In the previous section it was assumed that a magnet demagnetization curve does not experience any changes besides the one caused by exposure to an external field. Specifically, for the motor designer it would be extremely facilitating to work with a magnet type whose demagnetization curve remains unchanged under normal operating conditions. Unfortunately, this is never the case since the magnet magnetization is a function of the temperature. The temperature dependency of the magnetization is reflected in the demagnetization characteristics of the magnet and should be accounted for in the machine design. For a given load line, defined by the magnetic circuit design, the change of the flux density B upon short term temperature excursion from room temperature can be reversible or irreversible. This is demonstrated in Figure 2-7 where an example of demagnetization curves of a neodymium magnet at three different temperatures is depicted together with the change in the magnet operating point as a function of the temperature. At 20°C and for the drawn load line, the operating point ***a*** lies above the knee point. When the temperature rises to 40°C, the operating point moves to ***b***. As a consequence, the flux density B will decrease from B_a to B_b. Since the operating point ***b*** is above the knee point too, the resulting loss $\Delta B_{(40°C)} = B_a - B_b$ remains reversible. Thus, by returning to a magnet temperature of 20°C, the loss is fully recovered. If the temperature increases further to 100°C the magnet operating point moves to point ***c*** which is below the knee point of the corresponding demagnetization curve. As a consequence, if the magnet temperature drops again to 40°C and further to 20°C, the magnet will operate at points ***d*** and ***e*** correspondingly and not at points ***b*** and ***a***. A magnet operation at points ***b*** and ***a*** is only possible by remagnetizing the material.

The operating points ***d*** at 40°C and ***e*** at 20°C are the intersections of the load line with the so called "minor" demagnetization curves within the "major" B versus H loop, as described in detail by Campbell in [46], page 64. This state is characterized with reduced operating flux densities, since the loss $\Delta B = B_a - B_e$ is irreversible. Further cycling in the demonstrated temperature range (20°C to 100°C) will cause the magnet to operate reversibly along the new recoil line defined by points ***e***, ***d*** and ***c***. Thus, the magnet is considered to be stabilized at a reduced energy,[46].

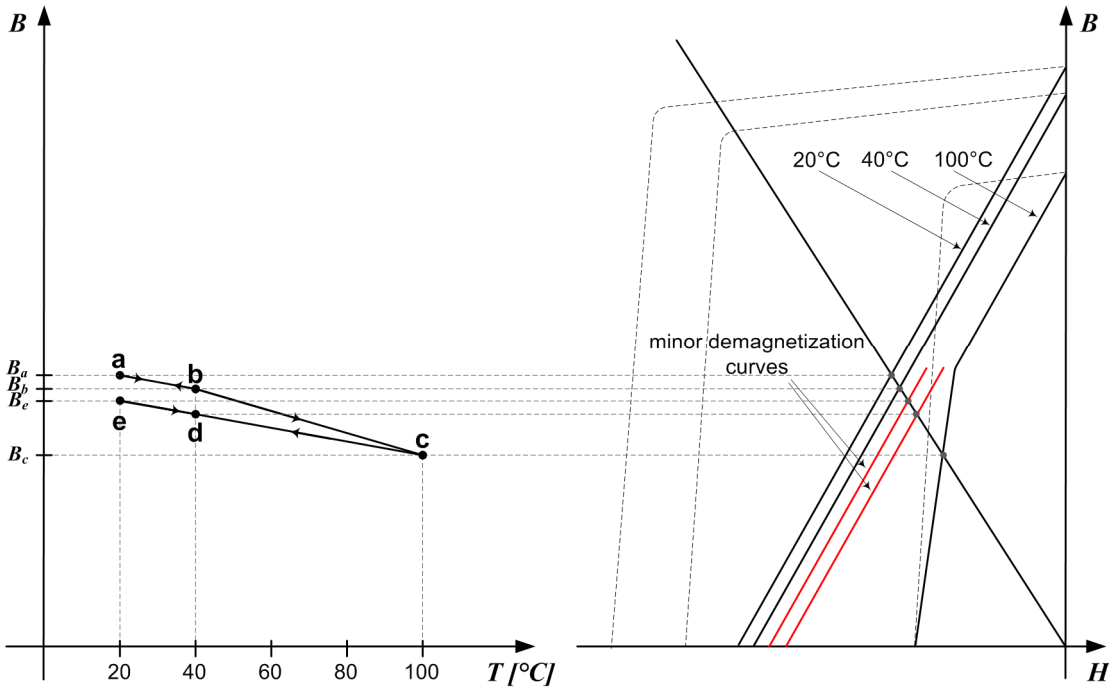

Figure 2-7: Change in magnet operation with temperature; the form and progression of the depicted demagnetization curves are exemplary for a neodymium magnet; as reference is used source [46], page 74, Figure 3.14.

For convenience, the temperature dependent reversible effect is often represented as reversible temperature coefficient that is defined in the following manner:

$$\alpha = \frac{B_{r(T)} - B_{r(20°C)}}{B_{r(20°C)}(T - 20°C)} * 100[\%/°C], \tag{2-1}$$

where $B_{r(20°C)}$ is the remanence at room temperature stabilized by cycling the magnet at least to a temperature level of T. The reversible flux density temperature coefficient

represents the change of the remanence as a percentage of the initial room temperature value per °C.

Together with the change in the flux density along temperature, Figure 2-7 demonstrates another important thermal characteristic of a magnet and that is the change of the intrinsic coercivity H_{ci} with temperature. This is another very important thermal effect that strongly influences the applicability of a permanent magnet. For neodymium magnets typically the intrinsic coercivity H_{ci} decreases when the temperature increases. This is strongly undesirable effect as it means that at higher temperatures the magnet gets vulnerable to strong opposing external fields. In a PMSM this means that at higher rotor temperatures excessive machine currents can lead to irreversible demagnetization of the magnets which results in permanent degradation of the motor performance.

Similar to the reversible flux density temperature coefficient defined in (2-1), there is a reversible temperature coefficient of coercivity β defined in analogical way:

$$\beta = \frac{H_{ci(T)} - H_{ci(20°C)}}{H_{ci(20°C)}(T - 20°C)} * 100[\%/°C]. \tag{2-2}$$

In the data sheets provided by the magnet manufacturers α and β are normally given for a defined temperature range. Magnetic circuit designers use H_{ci} in combination with β to determine the maximum operating temperature for a material, or in reverse, to determine the minimum acceptable H_{ci} value at the maximum operating temperature and calculate the required room-temperature values, [47].

Another fundamental thermal characteristic of a permanent magnet is the so called *Curie temperature*, T_c. By reaching the *Curie temperature* of a magnetic material, the magnetic moments start losing their alignment so that at a temperature above T_c, the spontaneous magnetization does not exist at all and the material becomes paramagnetic. Therefore a permanent magnet should be operated at maximum temperature much below its characteristic T_c value.

2.4 Permanent Magnets for Motor Applications

Nowadays the most important application for permanent magnets is found in rotating electric machines. There are different kinds of PM motor topologies, however the most commonly used one implies permanent magnet assembly in the rotating part. For sake of clarity and better understanding, adverse external field and temperature effects on permanent magnets were separately considered so far. In a PM motor, the magnet is

simultaneously exposed to elevated temperatures and external opposing fields, the armature reaction. Therefore, any expected degradation of the magnetic properties, both reversible and irreversible, reflected in the demagnetization curve for given operating range and conditions, should be well considered in the machine design. From machine designer point of view, a good magnetic material suitable for PM machine is characterized predominantly by following key characteristics:

- High energy product in order to achieve high air gap flux density. The size of the machine can be reduced by maintaining high torque density in the machine.
- High intrinsic coercivity $-H_{ci}$ which is directly related with high resistance to demagnetization from the motor's own armature winding, [46].
- Low reversible flux density temperature coefficient, which means smaller changes in the demagnetization curve within wide operating temperature range, extremely appreciated by both motor and control designer.
- Low reversible coercivity temperature coefficient for better stability and lower risk for irreversible demagnetization upon elevated operating temperatures.

Unfortunately, there is still no magnetic composite that fully satisfies the combination of all desired characteristics without being too expensive or suffering insufficient availability in terms of raw materials. Nowadays there are three major type of permanent magnets considered in different kind of motor applications: Ceramic ferrites, Samarium-cobalt ($SmCo_5$ and Sm_2Co_{17}) and neodymium-iron-boron ($Nd_2Fe_{14}B$).

Ceramic ferrites have been for long time commercially available and one of the first magnets used in the early evolutionary stage of PM machines. Ferrite magnets are manufactured mainly of strontium or barium ferrites and iron oxide. Although they have very high reversible temperature coefficient and relatively low energy density, they are a "conservative" good choice due to their stable low price and abundance of raw materials. For many years they were ousted by the high energy rare-earth magnets Sm_2Co_{17} and $Nd_2Fe_{14}B$. Recently they are undergoing new revival since rare-earth elements, the base for SmCo and NdFeB magnets, start experiencing some supply perturbations. Ceramic ferrites have relatively high electric resistance and consequently lower eddy current content upon operation at high speeds.

NdFeB is currently the most widely-used rare-earth magnet in electric motors. The good acceptance of the magnet is justified by its high intrinsic coercivity and big maximum energy product. PMSMs manufactured with neodymium magnets characterize with very high power density. The motor size is significantly reduced by maintaining an excellent

torque capability. There are two types of neodymium magnets commonly produced commercially: sintered and bonded. Sintered magnets are made from dry granules of elemental materials which are compacted under pressure in a metal die and then heated at high temperature to fuse the granules together, while bonded magnets are made from magnetic metal powder mixed with a polymer [48]. Although bonded magnets have lower energy compared to their sintered counterpart, they reveal significant advantage in terms of simplified assembly in the motor. Neodymium magnets have relatively high coercivity temperature coefficient but this has been tolerated because of their potentially low costs and high energy density. The stability shortcomings have to be further accounted for in the machine design.

In this relation, the Samarium-cobalt magnets are much more stable and can be operated at much higher temperature than neodymium magnets, nevertheless they reveal some other disadvantages such as very high price and low mechanical integrity (easy to chop). Therefore, their usage in electric motors is quite limited to specific applications characterized with over average high operating temperature range, such as aerospace, and military applications [49], [50].

Table 2-1: Comparison of properties of magnetic materials used in electric motors; Sources: [44], [51]–[56]

Properties / **Magnet**	**B_r (T)**	**H_{ci} (kA/m)**	**BH_{max} (kJ/m^3)**	**T_c (°C)**	**α (%/°C)**	**β (%/°C)**
Ceramic Ferrite	0.23÷0.43	150÷380	8.5÷34.5	450	-0.20	+0.27
$SmCo_5$	0.8÷1.0	1200÷2000	110÷190	750	-0.05	-0.3
Sm_2Co_{17}	0.95÷1.15	450÷2000	175÷240	800	-0.03	-0.2
Sintered $Nd_2Fe_{14}B$	0.9÷1.4	750÷2000	200÷440	310	-0.10	-0.60
Bonded $Nd_2Fe_{14}B$	0.6÷0.7	600÷1200	60÷100	470	-0.07	-0.40

Table 2-1 summarizes major magnetic properties of permanent magnets used in electric machines. The table gives maximum, minimum and average values from data sheets currently provided by permanent magnet manufacturers and reflects to a great extent the

actual properties improvements of materials that are commercially available. In the last 20 years the material research has brought indeed the most properties improvements in the neodymium magnets composite. Although the magnet has been suffering recently some image loss due to eventual supply perturbations resulting from monopolist manufacturing policy, it is still considered the material with the highest potential as it makes possible the production of PM machines with high energy density at relative low price. However, the use of NdFeB magnets in PMSM reveals persisting challenge for the motor control engineers because of the magnet low thermal stability influencing the motor performance. In order to increase the intrinsic coercivity H_{ci} of neodymium magnet composites at high temperatures, rare-earth element Dysprosium (Dy) can be added. Adding Dy to $Nd_2Fe_{14}B$ inevitably leads to a reduction of the magnet maximum energy product $(BH)_{max}$. However, resource problems related to low extraction ratio of Dy from rare-earth mineral ores are considered more serious than the decrease in maximum energy product, [57]. There is still persistent challenge how to handle thermal stability of PM machines with NdFeB magnets. The solution given in the current work focuses on detection of the magnet temperature and is seen as an auxiliary technique for adaptive control that can improve performance and ensure safety operation of PM machines.

3 Permanent Magnet Synchronous Machine - Modelling and Control

The analyses of the proposed magnet temperature estimation are predominantly carried out utilizing various space vector models of PMSM. Such models describe the machine behaviour under steady-state and transient operation which makes them very suitable for the current investigation. Therefore, an insight in the space vector theory and modelling of PMSM is given in this chapter. The space vector theory was originally introduced by Kovács, however more comprehensive and extended approach was given for example by Vas in his books [58]–[60] which are considered here as main reference works. The control scheme used through the whole experimental and validation process is a conventional space vector field oriented control, therefore an introduction to basic aspects of the field oriented current control of PMSM are presented as well. All quantities and machine parameters, if not differently stated, are given in this work in per-unit system.

3.1 Space Vector Theory

For any instantaneous values of the currents in a three-phase distributed stator windings displaced symmetrically by 120° degrees from each other, under the assumption of linear magnetic conditions, the resulting stator magnetomotive force (m.m.f.) is sinusoidal distributed in the machine. Thus, a stator current space vector $\underline{i_s}$ can be introduced that represents the stator m.m.f. spatial displacement in the machine:

$$\underline{i_s} = \frac{2}{3}\left(i_a + i_b\underline{a} + i_c\underline{a}^2\right). \tag{3-1}$$

where $\underline{a}$ is spatial operator $\underline{a} = e^{j2\pi/3}$, and i_a, i_b and i_c are the instantaneous stator phase currents in the machine respectively. For arbitrary stator phase currents, the stator current space vector $\underline{i_s}$ gives the maximum magnitude and the angle of maximum magnitude of the m.m.f. sinusoidal distribution produced by the three phase windings, as depicted in Figure 3-1. Upon steady-state excitation with sinusoidal nominal currents, the current space vector rotates with constant angular speed ω in the positive direction in space and has constant amplitude of 1. The projections of the current space vector $\underline{i_s}$

on the stator phase axes directly yield the instantaneous values of the stator phase currents.

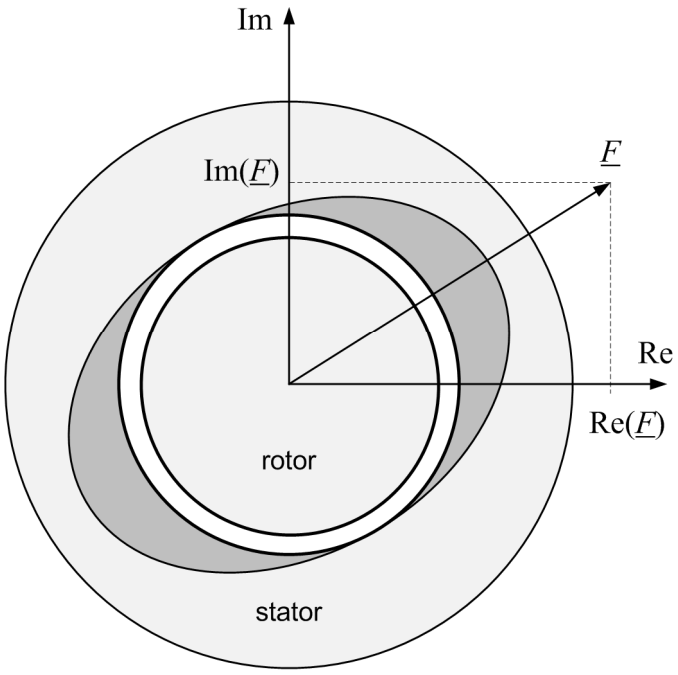

Figure 3-1: The physical meaning of the stator current space vector. The stator current space vector points in direction of maximum m.m.f.

Considering a stationary reference frame fixed to the stator with a real and imaginary axis denoted α and β respectively, the stator current space vector $\underline{i}_s$ can be decomposed in two phase components:

$$\underline{i}_s^s = \left|\underline{i}_s\right| e^{j\gamma_s} = i_\alpha + j i_\beta \,, \tag{3-2}$$

where $\underline{i}_s^s$ denotes the current space vector $\underline{i}_s$ expressed in the stator oriented reference frame and γ_s is the angle of the $\underline{i}_s$ with respect to the stator oriented reference frame. Analogously to the stator oriented reference frame, the stator current space vector $\underline{i}_s$ can be expressed in a reference frame fixed to the rotor with a real and imaginary axis denoted d and q respectively. In the space vector machine analysis, it is a common praxis to transform a vector quantity from the stator to the rotor oriented reference frame and vice versa since a space vector machine equation can only be correctly calculated when all vector quantities are expressed in the same reference frame.

The stator current space vector $\underline{i}_s^s$ expressed in the stator oriented reference frame (α, β), is transformed in the rotor oriented reference frame (d, q) in the following manner:

$$\underline{i}_s^r = \left|\underline{i}_s\right| e^{j\gamma_r} = \left|\underline{i}_s\right| e^{j(\gamma_s - \theta)} = \underline{i}_s^s e^{-j\theta}, \tag{3-3}$$

where $\underline{i}_s^r$ denotes the stator current space vector $\underline{i}_s$ expressed in the rotor oriented reference, γ_r is the angle of $\underline{i}_s$ with respect to the rotor oriented reference frame and θ is the instantaneous angular displacement between the stator and rotor oriented reference frames.

3.2 Space Vector Models of PMSM

The present section gives an introduction to modelling of PMSM with space vector quantities as needed for the analytical approach of the proposed magnet temperature estimation technique. The presented motor equations consider both types of machines, a machine with surface-mounted magnets (Surfaced Permanent Magnet Synchronous Machine - SPMSM) and a machine with buried magnets inside the rotor (Interior Permanent Magnet Synchronous Machine - IPMSM). The section is structured by introducing sets of motor equations graded by their complexity and applied degree of simplification.

3.2.1 Motor Equations Considering Linear Magnetic Conditions

In the following motor voltage equations assuming linear magnetic conditions and exclusion of saliencies are derived. A SPMSM is characterized with a large effective air gap due to the low permeability of the magnetic material, which makes the effect of saliency negligible. Thus, the spatial variation of the magnetizing inductance can be neglected, which significantly simplifies the space vector motor equations. Furthermore, a larger effective air-gap in SPMSM implies lower synchronous reactance. Thus, the so-called load angle δ, the angle between the magnetizing flux linkage $\underline{\psi}_m$ and the flux linkage produced by the magnets $\underline{\psi}_M$, is negligibly small. Indeed a good simplification is to assume that the magnetizing flux linkage in SPMSM equals the rotor flux linkage, $\underline{\psi}_m = \underline{\psi}_M$.

To develop the space vector model of a SPMSM, the stator real voltage equations of a general three phase a.c. machine should be given first

$$u_a = R_s i_a + \frac{d\psi_a}{dt} \tag{3-4}$$

$$u_b = R_s i_b + \frac{d\psi_b}{dt} \tag{3-5}$$

$$u_c = R_s i_c + \frac{d\psi_c}{dt}\ , \tag{3-6}$$

where u_a, u_b, u_c are the instantanous values of the stator phase voltages and ψ_a, ψ_b, ψ_c are the instantaneous values of the stator phase flux linkages and R_s is the stator winding resistance. Similar to the stator current space vector presentation, the stator phase voltages can be given in a space vector form

$$\underline{u}_s = \frac{2}{3}\left(u_a + u_b\underline{a} + u_c\underline{a}^2\right). \tag{3-7}$$

Hence, the machine stator voltage equations (3-4)-(3-6) can be combined in a single space vector voltage equation expressed in the stator oriented reference frame

$$\underline{u}_s^s = R_s\underline{i}_s^s + \frac{d\underline{\psi}_s^s}{dt}\ , \tag{3-8}$$

where $\underline{\psi}_s^s$ is the space vector of the stator flux linkage formulated in the stator oriented reference frame. For a PMSMS, $\underline{\psi}_s^s$ is defined in terms of motor currents and rotor flux linkage ψ_M in the stator oriented reference frame as follows:

$$\underline{\psi}_s^s = L_s\underline{i}_s^s + \psi_M e^{j\theta}, \tag{3-9}$$

where θ is the angle between the stator and rotor oriented reference frame, and L_s is the self-inductance of the stator windings. The stator space vector voltage equation (3-8) can be further expressed in the rotor oriented reference frame by transforming all space vector quantities according to the transformation procedure (3-3):

$$\underline{u}_s^r = \underline{u}_s^s e^{-j\theta} = R_s\underline{i}_s^r + \frac{d\underline{\psi}_s^r}{dt} + j\omega\underline{\psi}_s^r, \tag{3-10}$$

where ω is the angular speed between the stator and rotor oriented reference frames. Upon a transformation in the rotor oriented reference frame the stator flux linkage becomes:

$$\underline{\psi_s^r} = L_s \underline{i_s^r} + \psi_M, \tag{3-11}$$

and formulated in its two-axes decomposed form under the assumption of magnetic linearity and negligible saliency:

$$\psi_d = L_s i_d + \psi_M \tag{3-12}$$

$$\psi_q = L_s i_q. \tag{3-13}$$

Hence, in the rotor reference frame, the d- and q-axis stator voltage components can be given in the following form:

$$u_d = R_s i_d + L_s \frac{di_d}{dt} - \omega L_s i_q \tag{3-14}$$

$$u_q = R_s i_q + L_s \frac{di_q}{dt} + \omega L_s i_d + \omega \psi_M. \tag{3-15}$$

In motor analysis and field oriented space vector control it is a general practice to use the space vector voltage equations formulated in the rotor oriented reference frame. The advantage is straightforward, as in a reference frame fixed to the rotor the stator voltage and current space vectors and the stator flux linkage do not contain dependency of the instantaneous angular displacement between the rotor and stator reference frames θ, whereby machine transient analyses are significantly simplified. Furthermore, as it will be demonstrated in the next sections, space vector motor equations, that consider saliencies and saturation effects in the machine, are more convenient to derive and analyze in the rotor oriented reference frame.

3.2.2 Motor Equations Considering Salient Effects

In SPMSM, due to the negligible armature reaction, the air gap is considered uniform and therefore L_s is not dependent of the rotor position and can be treated as constant coefficient in (3-9)-(3-15). However, due to the machine construction, in IPMSM no smooth air gap can be assumed since there is a magnetic salience. The stator inductance L_s is a function of the rotor position and therefore L_s becomes a complex value in the voltage equations expressed in the stator oriented reference frame (3-10). This drawback can be overcome upon the transformation in the rotor oriented reference frame, where instead of a single value, two different values have to be used, L_d and L_q, that reflect the

different magnetic flux paths seen by the stator current space vector in the direct and quadrature axis of the machine respectively. Thus, the stator flux linkage components from (3-12) and (3-13) become:

$$\psi_d = L_d i_d + \psi_M \tag{3-16}$$

$$\psi_q = L_q i_q. \tag{3-17}$$

Because of the magnets that have nearly the same reluctance as air, in a IPMSM the q-axis flux path presents lower reluctance than the d-axis flux path. Consequently, in IPMSM, $L_q \gg L_d$, while in SPMSM $L_q \approx L_d$. The two axis components of the stator voltage space vector formulated in the rotor reference frame become

$$u_d = R_s i_d + L_d \frac{di_d}{dt} - \omega L_q i_q \tag{3-18}$$

$$u_q = R_s i_q + L_q \frac{di_q}{dt} + \omega L_d i_d + \omega \psi_M. \tag{3-19}$$

These equations are also referred to as Park's model, since Park in his Two-reaction Theory, [61], formulated an analytical approach to model salient pole synchronous machine by transforming stator quantities in rotor oriented space vector and introducing different values for the stator inductance in the direct and quadrature axis of the machine.

3.2.3 Motor Equations Considering Saturation Effects

The voltage equations given in (3-14) and (3-15), and (3-18) and (3-19) are only valid if saturation effects in the stator and rotor steel core, including cross-saturation effects, are neglected and the flux density distribution can be considered sinusoidal. However, due to saturation of the main flux paths the resultant flux density distribution is distorted and contains space harmonics. According to Vas [59], page 325, "*These can be neglected if sinusoidally distributed windings are assumed since only the fundamental sinusoidal component of the flux wave can produce flux linkages with sinusoidally distributed windings. The effects of hysteresis and eddy currents are also neglected. It is important consequence of these assumptions, that despite the magnetic non-linearity, it is still possible to use space-vector or two-axis theories*".

Under consideration of saturation in the main flux paths, the stator self inductances in the d- and q-axis, L_d and L_q, cannot be treated as constant values, since they vary with the saturation. Thus, in contrast to (3-16) and (3-17), the flux linkages ψ_d and ψ_q become nonlinear functions of the current. Therefore, obtaining the time derivative of ψ_d and ψ_q requires the application of the chain differentiation rule:

$$\frac{d\psi}{dt} = \frac{d\psi}{di}\frac{di}{dt}\,, \tag{3-20}$$

whereby the stator voltage equations expressed in the rotor oriented reference frame (3-18) and (3-19) become

$$u_d = R_s i_d + L_d^* \frac{di_d}{dt} - \omega L_q i_q \tag{3-21}$$

$$u_q = R_s i_q + L_q^* \frac{di_q}{dt} + \omega L_d i_d + \omega \psi_M. \tag{3-22}$$

Compared to the absolute inductances L_d and L_q, L_d^* and L_q^* are referred to as differential inductances in the d- and q-axis of the machine and can be expressed with respect to the currents as follows:

$$L_d^* = \frac{dL_d}{di_d} i_d + L_d \tag{3-23}$$

$$L_q^* = \frac{dL_q}{di_q} i_q + L_q. \tag{3-24}$$

3.2.4 Motor Equations Considering Cross-coupling Effects

A machine model described by the voltage equations (3-21) and (3-22) still does not account for cross-saturation effects in the machine. Cross-saturation phenomena results from existence of cross-coupling (mutual) inductances between the d- and q-axis of the machine that arise in the machine upon saturation of the main flux paths. While in SPMSM these can be neglected due to the low armature reactance, in IPMSM cross-coupling inductances are considerable. This has been originally demonstrated by Sneyers in [62] and by Console&Abela in [63], where coupling inductances have been proposed to be strongly considered in further modelling of IPMSM.

By considering cross-coupling between the d- and q-axis, the corresponding flux linkage components ψ_d and ψ_q receive an extra term that accounts for the flux linkage produced by the current in the other axis as follows:

$$\psi_d(i_d, i_q) = \psi_{dd}(i_d) + \psi_{dq}(i_q) + \psi_M \tag{3-25}$$

$$\psi_q(i_d, i_q) = \psi_{qd}(i_d) + \psi_{qq}(i_q)\,, \tag{3-26}$$

where ψ_{dd} is the flux linkage in the d-axis produced by i_d, ψ_{dq} is the flux linkage in the d-axis produced by i_q, ψ_{qq} is the flux linkage in the q-axis produced by i_q and ψ_{qd} is the flux linkage in the q-axis produced by i_d. Analogously to (3-20) and (3-21), applying the chain rule from (3-19) and considering the new coupling flux linkage terms in (3-25) and (3-26) the stator voltage components formulated in the rotor oriented reference frame become

$$u_d = R_s i_d + L^*_{dd}\frac{di_d}{dt} + L^*_{dq}\frac{di_q}{dt} - \omega L_{qq} i_q - \omega L_{qd} i_d \tag{3-27}$$

$$u_q = R_s i_q + L^*_{qq}\frac{di_q}{dt} + L^*_{qd}\frac{di_d}{dt} + \omega L_{dd} i_d + \omega L_{dq} i_q + \omega\psi_M, \tag{3-28}$$

where L_{dd} and L_{qq} are the absolute inductances in the d- and q-axis of the motor, L_{dq} and L_{dq} are the corresponding cross-coupling (mutual) inductances and L^* are the corresponding differential inductances with respect to the current:

$$L^*_{dd} = \frac{dL_{dd}}{di_d} i_d + L_{dd} \tag{3-29}$$

$$L^*_{dq} = \frac{dL_{dq}}{di_q} i_q + L_{dq} \tag{3-30}$$

$$L^*_{qq} = \frac{dL_{qq}}{di_q} i_q + L_{qq} \tag{3-31}$$

$$L^*_{qd} = \frac{dL_{qd}}{di_d} i_d + L_{qd}. \tag{3-32}$$

As already concisely stated in [64], the differential self inductances L^*_{dd} and L^*_{qq}describe the flux variation of one axis as a consequence of the current change in the same axis,

while the differential mutual inductances L_{dq}^{*} and L_{qd}^{*} describe the flux variation of one axis as a result of the current change in the other axis and vice versa. If cross saturation can be neglected, L_{dq}^{*} and L_{qd}^{*} become zero.

The set of voltage equations that can be used to describe the behaviour of a PMSM depends strongly on the degree of magnetic circuit saturation and consequently the assumption that can be made for a given machine.

3.3 Field Oriented Control of PMSM

In the following, an introduction to the Space Vector Field Oriented Control (SVFOC) of PMSM is given. The SVFOC scheme is used in the current investigation to demonstrate applicability and feasibility of the proposed magnet temperature estimation.

3.3.1 Electromagnetic Torque

The electromagnetic torque in a.c. machine is given by the outer product of the stator flux linkage $\underline{\psi}_s$ and the stator current space vector $\underline{i}_s$.

$$t_e = -\mathrm{Im}\left(\underline{\psi}_s \underline{i}_s^*\right) \tag{3-33}$$

$$t_e = \left|\underline{\psi}_s\right| \left|\underline{i}_s\right| \sin\left[\angle\left(\underline{\psi}_s\,, \underline{i}_s\right)\right]. \tag{3-34}$$

For a machine with P pole pairs the expressions have to be multiplied by P. The electromagnetic torque is proportional to the area defined between the vectors $\underline{\psi}_s$ and $\underline{i}_s$ in arbitrary reference frame as demonstrated in Figure 3-2.

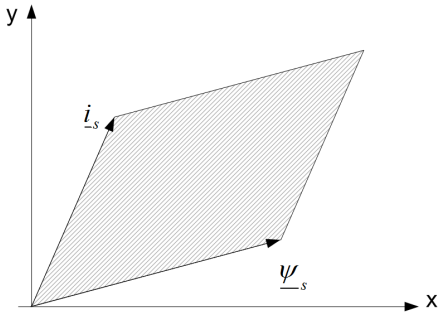

Figure 3-2: Electromagnetic torque production in a.c. machine, source [65].

The stator flux linkage in PMSM comprises of magnetizing flux:

$$\underline{\psi}_s = \underline{\psi}_m \tag{3-35}$$

Thus, according to (3-33) and (3-34), the maximum electromagnetic torque per stator current can be achieved when the stator current space vector $\underline{i}_s$ is perpendicular to the magnetizing flux linkage $\underline{\psi}_m$. By resolving the space vectors into their direct and quadrature axis components, the electromagnetic torque for PMSM is obtained in the rotor oriented reference frame as follows:

$$t_e = (L_d i_d + \psi_M) i_q - L_q i_q i_d. \tag{3-36}$$

Since in a SPMSM the stator armature reactance is relatively small and $L_d \approx L_q$ because of the large effective air-gap, the electromagnetic torque equation from (3-36) can be reduced to

$$t_e = \psi_M i_q. \tag{3-37}$$

If the flux linkage produced by the permanent magnets is assumed constant, the electromagnetic torque output of a SPMSM can be controlled in the rotor oriented reference frame solely by the quadrature-axis stator current component i_q.

In contrast, in IPMSM there is a significant difference between the direct and quadrature reluctance, $L_d \ll L_q$, as mentioned before. This introduces a negative reluctance torque component in (3-36). Thus, in rotor oriented reference frame a maximum torque per stator current in a IPMSM can be obtained by introducing a negative direct-axis stator current component i_d.

$$t_e = \psi_M i_q + \left(L_d - L_q\right) i_q i_d. \tag{3-38}$$

As a consequence, a control strategy for IPMSMS implying a maximum torque per stator current approach is characterized with greater complexity compared to SPMSM. This kind of control strategy is often referred to as Maximum Torque Per Ampere (MTPA) control in the literature. Due to its complexity, MTPA control for IPMSM has been a subject of intensive investigation in recent years, whereby more sophisticated approaches considering saturation effects can be found in [66]–[73]. It should be noted here, that although in the current investigation the motor under test is an IPMSM, no MTPA strategy is pursuit, since this is not a focus of the thesis. Moreover, the IPMSM under test is simply controlled according to (3-37).

3.3.2 Field Oriented Current Control

A field oriented current control implies a decoupled control of the stator direct and quadrature current components in the rotor oriented reference frame. In the rotor oriented reference frame, as already mentioned, the flux linkage produced by the permanent magnets is coaxial with the direct frame axis. Fundamental requirements of the field oriented current control, as depicted in Figure 3-3, are an accurate knowledge of the phase stator currents and the rotor position of the motor. The phase currents i_a, i_b, i_c, are sampled and converted to digital values by an Analog Digital Converters (ADCs). A Clarke transformation routine transforms the phase currents into direct and quadrature components (α, β) in the stator oriented reference frame. The direct and quadrature components are further transformed into the rotor oriented reference frame (d, q) by the procedure described in (3-3), also referred to as Park transformation. The actual closed loop current control is realized in the rotor oriented reference frame by using PI current controller. Thus, the outputs of the current controllers are the direct and quadrature voltage components of a reference voltage space vector $\underline{u}_{s,ref}$ in the rotor oriented reference frame, which is required to produce the reference current components $i_{d,ref}$ and $i_{q,ref}$. The reference voltage space vector $\underline{u}_{s,ref}$ is then transformed into the stator oriented reference frame where via a Space Vector Pulse Width Modulation technique (SVPWM) and by means of a voltage source inverter it is applied to the motor terminals. For the transformation procedure, the angle between the stator and rotor oriented reference frames θ is derived by the mechanical rotor position θ_r obtained by an incremental encoder.

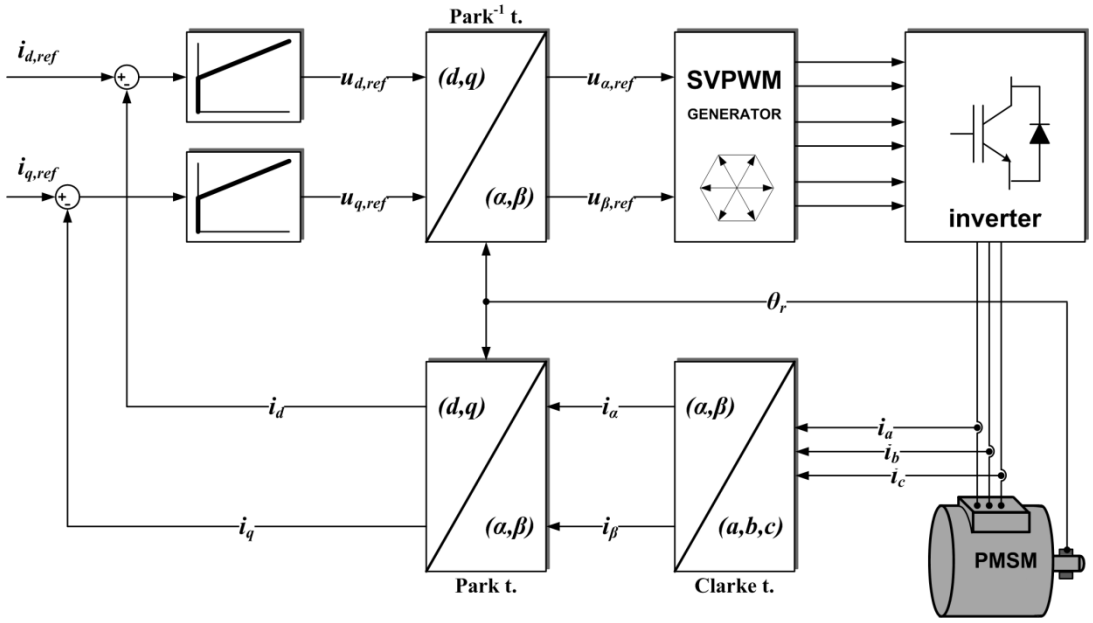

Figure 3-3: Field oriented current control of PMSM in the rotor fixed reference frame.

3.3.3 Space Vector Pulse Width Modulation - SVPWM

A block diagram of the motor control system, as used in the present work, is depicted in Figure 3-4. Although, voltages are impressed in the machine by using a 3-phase voltage source inverter, the stator windings seem to be fictitiously supplied by current sources controlled by the PI current controllers. This assumption is valid as long as the inverter is not saturated, which means that the inverter dc-link voltage V_{dc} is sufficient to "cover" all voltages that arise in the machine under nominal operation (nominal torque at nominal speed).

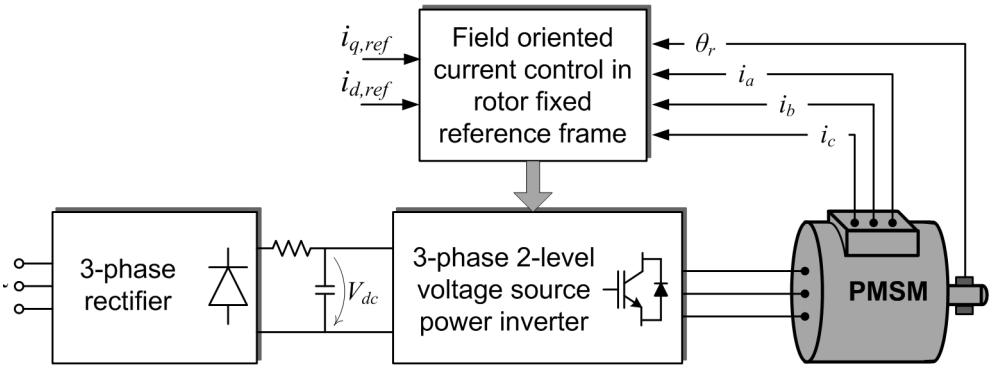

Figure 3-4: Block diagram of inverter fed PMSM drive.

The used voltage source power inverter is a common three-phase two level bridge inverter that feeds a PMSM with star-connected stator windings. Figure 3-5 shows the block diagram of such inverter, where V_a, V_b, V_c are the effective dc voltages applied on the motor terminals. The six switches represent semiconductor power switches, which in the real inverter used in this work are Insulated-Gate Bipolar Transistors (IGBTs).

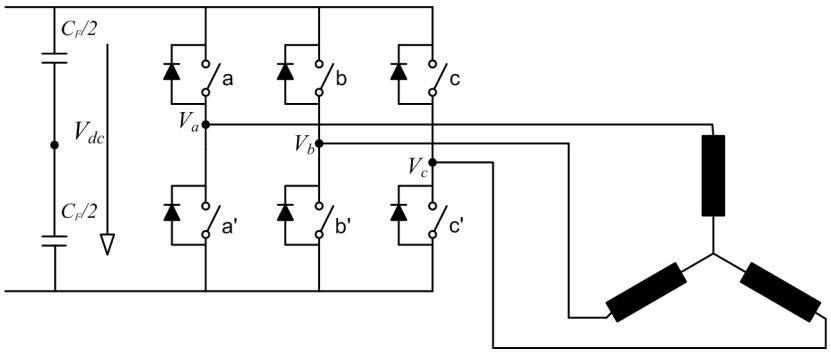

Figure 3-5: Block diagram of a motor with star-connected stator windings fed by three-phase two-level bridge power invert.

The upper and the lower transistor of the same bridge are driven by two complementary signals in a manner that when $\boldsymbol{a}$ is ON, $\boldsymbol{a}'$ is OFF and reverse so that no vertical conduction is possible. Under these constraints, there are eight possible combinations of ON and OFF states for the three upper switches. The eight combinations and the derived output line-to-line and phase voltages with respect to the constant inverter dc-link voltage V_{dc}, as well as the corresponding resultant voltage space vectors, are summarized in Table 3-1.

The eight possible switching patterns generate six non-zero voltage space vectors, also referred to as basic space vectors, and two zero voltage space vectors in the machine. The non-zero voltage space vectors divide the plane of the stator oriented reference frame (α, β) into six sectors as demonstrated in Figure 3-6. The length of each of the six basic space vectors is $2/3V_{dc}$. The angle between any adjacent two basic space vectors is 60 degree. The two zero vectors, which are at the origin, have a length of zero and therefore apply zero voltage to the machine. Thus, a reference voltage space vector $\underline{u}_{s,ref}$, which is generated by the current controller in order to produce a reference stator current space vector $\underline{i}_{s,ref}$ in the machine, is approximated by combination of the eight switching patterns. The approximation procedure is explained in detail by Toliyat and Campbell in [74], chapter 11.

Table 3-1: Switching patterns of three-phase two-level bridge power inverter, source [65].

Voltage vectors	Switching signals			Phase voltages			Line-to-line voltages		
	a	***b***	***c***	V_a	V_b	V_c	V_{ab}	V_{bc}	V_{ca}
$\underline{V}_0$	0	0	0	0	0	0	0	0	0
$\underline{V}_1$	1	0	0	2/3	-1/3	-1/3	1	0	-1
$\underline{V}_2$	1	1	0	1/3	1/3	-2/3	0	1	-1
$\underline{V}_3$	0	1	0	-1/3	2/3	-1/3	-1	1	0
$\underline{V}_4$	0	1	1	-2/3	1/3	1/3	-1	0	1
$\underline{V}_5$	0	0	1	-1/3	-1/3	2/3	0	-1	1
$\underline{V}_6$	1	0	1	1/3	-2/3	1/3	1	-1	0
$\underline{V}_7$	1	1	1	0	0	0	0	0	0

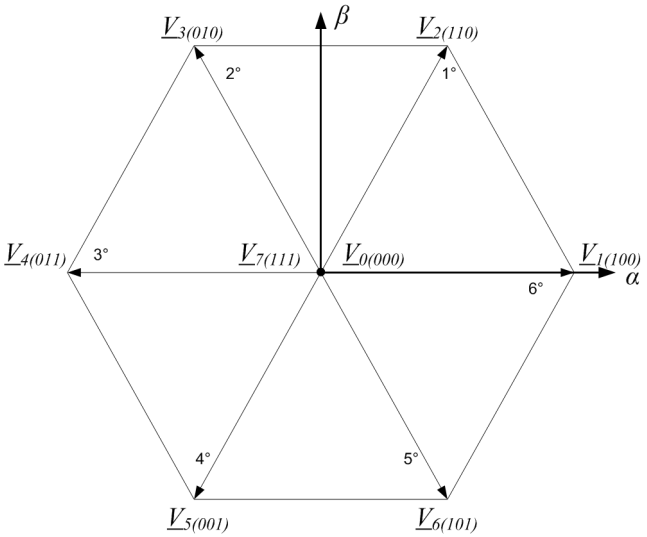

Figure 3-6: Basic inverter voltage space vectors, source [65].

4 Sensorless Estimation of the Permanent Magnet Temperature in PMSM

As outlined in chapter 2 the rotor flux linkage produced by the permanent magnets varies with the temperature. This has a direct influence on the electromagnetic torque production in the machine. According to the electromagnetic torque equations (3-37) and (3-38), constant electromagnetic torque control can be achieved solely when the instantaneous rotor flux linkage is known. Depending on the application and operating conditions, the temperature of the permanent magnets in PMSM can vary in a wide range. Therefore, a precise torque control of PMSM requires accurate information on the degree of change of the rotor flux linkage with the temperature. Since the demagnetization curves for a given magnet provide the change in the magnet magnetization over the temperature, the main challenge in the current thesis is confined to the objective to monitor the temperature of the permanent magnets in a PMSM in online real-time mode.

In the current chapter a novel approach to detect the magnet temperature in a PMSM is proposed without using any temperature sensors that measures directly the temperature of the magnets or the rotor. In the methodology presented here, no extra additional sensors are required than the general current sensors and an accurate knowledge of the rotor position that can be obtained either by encoder or a dedicated sensorless approach.

Basically, the presented method explores the changes in the saturation level of the stator laminated core of the machine upon varying magnet magnetization. Since the permanent magnet flux density depends on the temperature, the saturation level of the stator is indirectly dependent of the magnet temperature as well. The proposed method gives a procedure for estimating the temperature of the permanent magnets in a PMSM by detecting the degree of change in the saturation level of the machine stator core caused by the magnet temperature variation. This is realized here over the machine inductance in the d-axis of the motor. A change in the saturation level of the steel stator core in the d-axis of the motor will result in a change of the d-axis inductance. The approach presented here implies detection of the degree of change of the d-axis inductance by applying intermittently dc voltage pulses in the d-axis of the motor and evaluating the resulting current response. It is found that the slope of the d-current response upon voltage pulse in the d-axis of the motor is distinctive for various temperature levels in the permanent magnets.

The chapter is structured in the following order:

- The machine under test together with the overall experimental setup are briefly presented.
- Basic principles of the proposed temperature estimation procedure are given. A generation of a voltage pulse in the d-axis of the machine at standstill and under rotation is explained. The relationship between the magnet temperature and the d-current response upon a positive voltage pulse in the d-axis of the motor is established.
- Three basic implementation approaches of magnet temperature estimation procedures are analytically discussed and validated by experimental results:
    - Rotor temperature estimation by applying a single positive voltage pulse while the q-current of the machine is kept zero. Suitable for low or constant speed applications.
    - Rotor temperature estimation by applying a positive and negative voltage pulse while the q-current of the machine is kept zero. Suitable for a wide speed range applications.
    - Rotor temperature estimation under load conditions by applying a symmetrical positive and negative voltage pulse. Suitable for a wide speed range applications where the q-current cannot be interrupted.

4.1 Experimental Setup

In the following, a brief insight is provided into general characteristics and aspects of the experimental validation of the presented magnet temperature estimation. The objective is to describe the experimental laboratory framework and to give information on the conditions, instrumentation and techniques as used in the current investigation to verify the feasibility of the proposed method. Basic requirements that an appropriate experimental setup should fulfil are listed as follows:

- A PMSM equipped with online temperature monitoring system that can measure with satisfactory accuracy the absolute temperatures of the magnets and is suitable for a wide operating speed and temperature range.
- Since the method requires active voltage pulse injection, the motor test bench that controls the PMSM under test should provide pulse generation capability where the pulse width t_{pw} can be arbitrary set and the beginning of the pulse can be exactly defined with respect to the mechanical rotor position.

- External instrumentation or motor test bench capability that provides a mechanism for simultaneous sampling of all motor phase currents with at least 500KHz during the voltage pulse duration and can be triggered synchronously to the beginning of the pulse. This is needed since the method's sensitivity and accuracy strongly depends on the correct and precise evaluation of the machine current response upon a voltage pulse injection.

Therefore, for the purposes of the current investigation a specially designed rotor temperature monitoring system is built for a PMSM with temperature sensors located in the rotor. Furthermore, a new motor test bench is designed and implemented with capability to generate voltage pulses at arbitrary rotor position and mechanism to oversample simultaneously all motor phase currents with a sampling frequency of 2MHz.

4.1.1 The Interior Permanent Magnet Synchronous Machine under Test

The validation process is predominantly conducted on a newly designed IPMSM. The challenge is to prove method feasibility on a machine characterized with strong magnetic nonlinearity and salience affects. The machine used in the current investigation is 10KW water cooled PMSM with buried magnets and star connected stator windings. The rotor and stator of the machine are depicted in Figure 4-1 and Figure 4-2 respectively. The stator winding is a single-layer fractional slot distributed with 36 slots and eight poles. The fundamental wave winding factor of the symmetrical winding is ξ_s= 0.9452. The machine parameters are summarized in Table 4-1. The inductances of the machine are measured with LCR-Meter by a slow rotation of the rotor. The measurements are carried on at test frequencies of 100Hz. Thus, the measured minimum and maximum inductances are 4.8mH and 9.4mH respectively.

Table 4-1: Machine parameters of the IPMSM under test.

Nominal power	10kW
Nominal voltage	440V
Nominal current	25A
Phase resistance at 20°C	0.2465Ω
Nominal frequency	320Hz
Nominal speed	4800rpm

The permanent magnets used in the machine are of type NdFeB (VACODYM 655 HR) from Vacuumschmelze. The demagnetization curves provided by the manufacturer are depicted in Figure 4-3. Basic magnetic properties of the material are summarized in Table 4-2. Additionally, the stator flux linkage of the machine is measured as a function of the permanent magnets temperature. The results are depicted in Figure 4-4 and obtained under no-load test at nominal speed by heating-up the machine. In the setup, the permanent magnets temperature is measured directly by the temperature sensors in the rotor and the rotating temperature monitoring device.

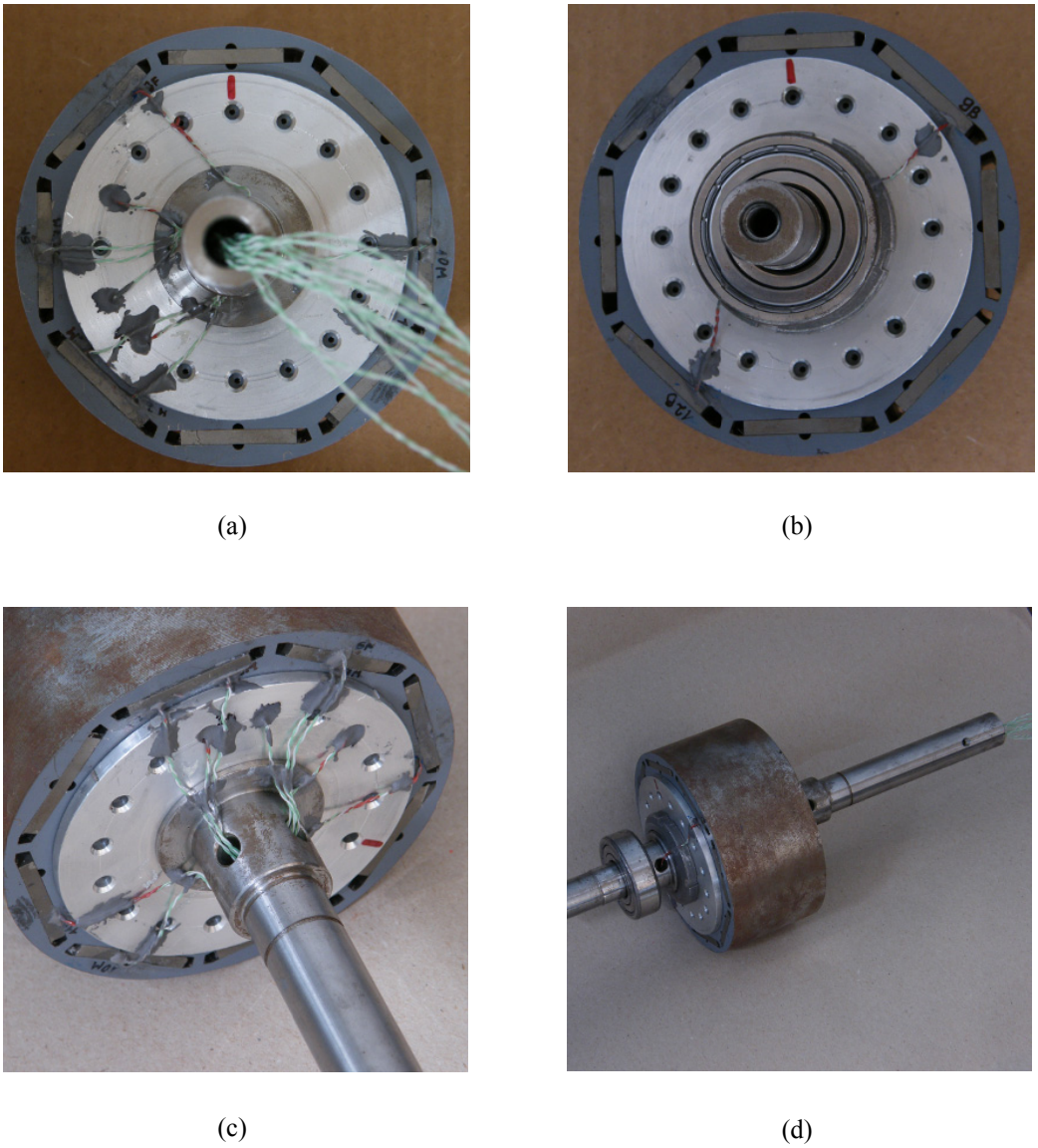

(a) (b)

(c) (d)

Figure 4-1: The rotor of the IPMSM under test equipped with temperature sensors at different locations: a) front profile view; b) back profile view; c) side view; d) plane view.

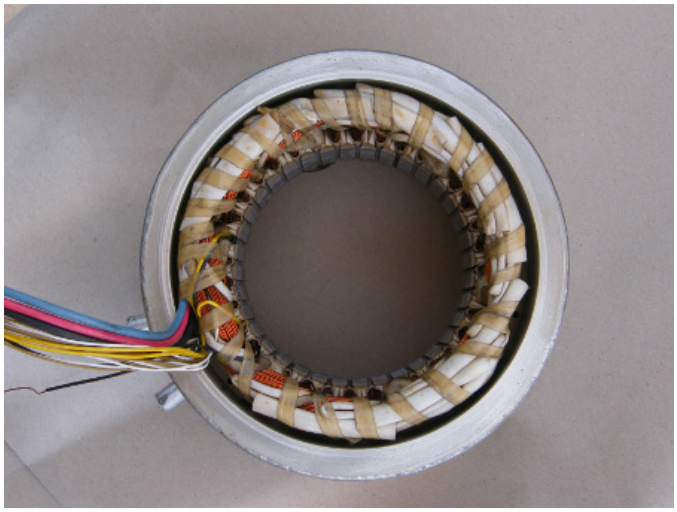

Figure 4-2: The Stator of the IPMSM under test: single-layer fractional slot-distributed stator winding with 36 stator slots and eight poles.

Table 4-2: Properties of the permanent magnet material used in the IPMSM under test (source www.vacuumschmelze.de).

B_r(T)	H_{ci} (kA/m)	BH_{max}(kJ/m^3)	T_{max}(°C)	α (%/°C)	β(%/°C)
1.28	150÷380	315	150	-0.100	-0.55

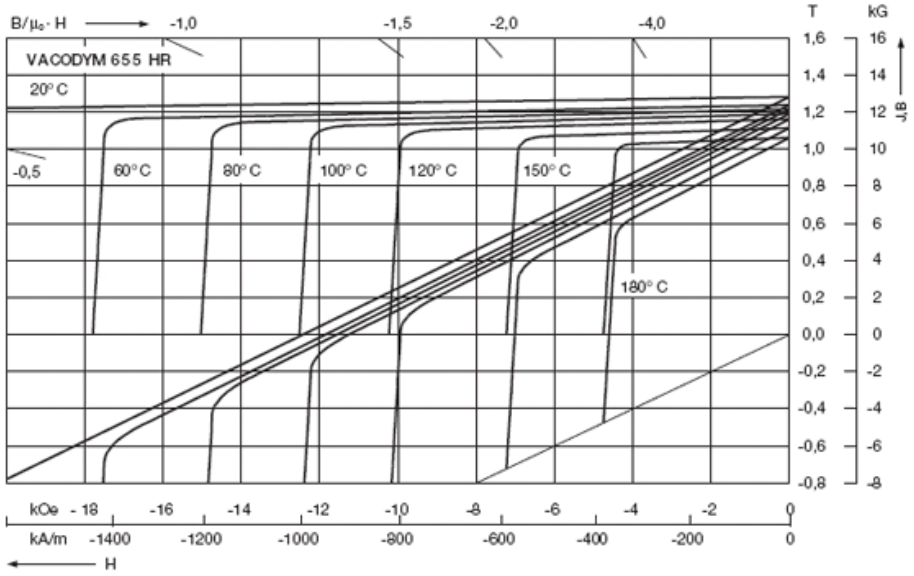

Figure 4-3: Demagnetization curves data sheet of the Nd-Fe-B magnets used in the IPMSM under test (source www.vacuumschmelze.de).

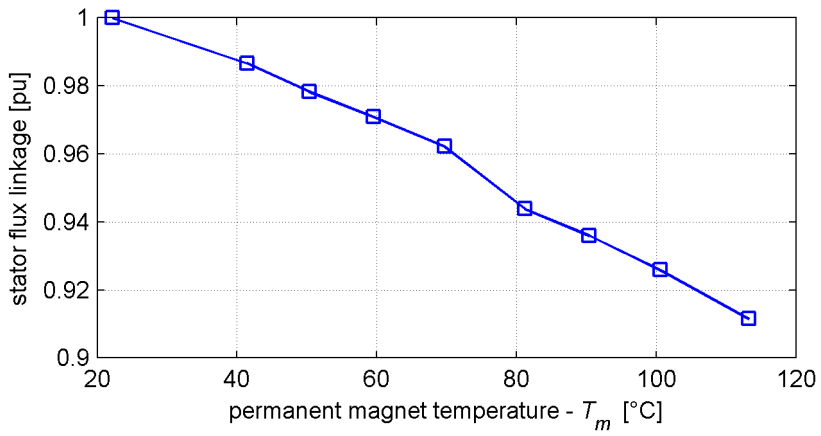

Figure 4-4: Stator flux linkage measured under no-load test as a function of the magnet temperature.

The rotor is specially manufactured to accommodate temperature sensors. Before the magnets were assembled, holes through the rotor lamination with diameter of 2mm were laser drilled in different locations. There are sensors directly fixed to the permanent magnets. As shown in Figure 4-1a and Figure 4-1c, the sensors cabling is led out of the machine through a longitudinal hole inside the rotor shaft. Since one end of the motor shaft is coupled with a load machine and on the other end a rotor temperature monitoring device is fixated, only a hollow-shaft incremental encoder can be used, see Figure 4-5. This is because the data transmission between the rotor temperature monitoring device and a stationary receiver is realized by infrared optical data link, whereby the infrared LED on the device is centred with respect to the motor shaft.

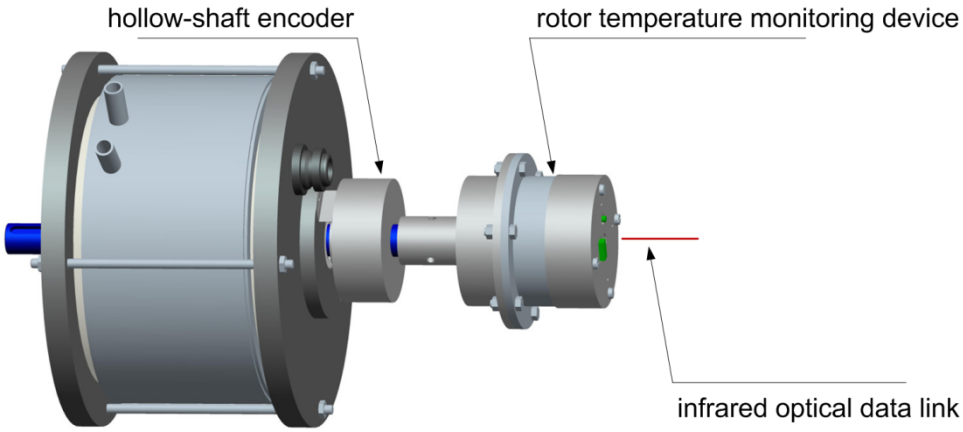

Figure 4-5: CAD design drawing of the investigated IPMSM including the incremental encoder and the rotor temperature monitoring device.

4.1.2 Rotor Temperature Monitoring Device

Although detailed information on the rotor temperature monitoring device is given in chapter 5, for better understanding of the experimental results and measuring conditions, basic device characteristics are pointed out in the following.

The used temperature sensors are thermocouples of type K wired to the battery powered instrumentation fixated to the motor shaft as shown in Figure 4-5. Considering rechargeable NiMH cell, with a single battery charge 6 sensors are simultaneously measured every 100ms for over 9 hours. The purpose of the device is to measure, amplify and digitalize the thermocouple voltages, and transmit the data to a stationary receiver via infrared optical data link. The stationary receiver is connected to a PC that allows online monitoring of the temperature signals.

The used thermocouples are of tolerance class 1, which implies relative tolerance of ±0.36°C. The investigated rotor temperature range is normally between 20°C and 120°C. The overall tolerance of the measured temperature signals is tested to be around 1°C validated in high precision environmental chamber. In general, if not otherwise stated, a reference permanent magnet temperature is built as an average of 6 temperature sensors outputs. The exact location of the sensors is depicted in Figure 4-6 and summarized in Table 4-3. A reference permanent magnets temperature value for a given measurement or a measurement set is realized here by controlling the motor winding currents in a manner that a constant temperature is established across the magnets. For example, the outputs of the sensors for measurements carried out at a reference temperature of 60°C are listed in Table 4-4.

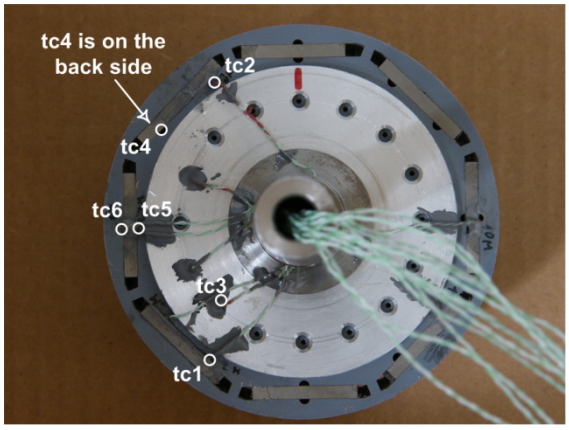

Figure 4-6: The temperature sensors in IPMSM under test that are considered to define a reference permanent magnet temperature.

Table 4-3: Rotor temperature sensors locations, see Figure 4-6.

sensor	location description
tc1	underneath permanent magnet, off-centred
tc2	underneath permanent magnet, lower corner
tc3	rotor yoke, underneath permanent magnet
tc4	underneath permanent magnet, upper corner
tc5	underneath permanent magnet, centred
tc6	above permanent magnet, centred

Table 4-4: Rotor temperature sensors outputs for 60°C reference temperature in degree Celsius.

tc1	tc2	tc3	tc4	tc5	tc6
59.55	60.18	59.87	59.87	59.55	60.50

4.1.3 PWM Inverter

The PWM inverter that is used to control the machine under test is SKiiP 132GD120-3DU from the SKiiP2 product family of SEMIKRON. The inverter is factory equipped with current sensors integrated in each phase leg. According to manufacturer's data sheets, the current sensor has bandwidth of 100kHz and a response time $t_{resp} < 1\mu s$, [75]. An integrated interlock circuit prevents that the TOP and the BOT IGBT of one phase leg are switched on at the same time (internal short circuit). The inverter built-in interlock dead time is $t_{iDT} = 2.3\mu s$, [76]. The interlock dead time does not add to a dead time given by the controller t_{DT}, which in the DSP software is set to $2.5\mu s$. Thus, in the current investigation the actual inverter dead time is $t_{DT} = 2.5\mu s$. Table 4-5 summarizes the inverter delay times, which are relevant for the generation of an effective pulse on the corresponding phase leg output terminal.

Table 4-5: Inverter delay times.

symbol	delay time description	min.	typ.	max.	unit
$t_{d(on)}$	transistor turn-on propagation time, [76]			1.5	µs
$t_{d(off)}$	transistor turn-off propagation time, [76]			1.4	µs
t_{DT}	controller dead time		2.5		µs

Propagation delay between a switching command and an effective voltage pulse

Depending on the direction of the current, the inverter dead time t_{DT} and the turn-on/off transistor delay times cause a delay between the voltage pulse width t_{pw} according to the switching command signal and the effective voltage pulse width $t_{pw(eff)}$ applied to the machine terminals. This is explained with Figure 4-7, where the switching between the upper transistor T1 and lower transistor T2 of single phase leg PWM inverter is demonstrated with respect to the current polarity, the pulse switching command, the gate driver signals DS1 and DS2, and the actual voltage potential at a phase output terminal $\boldsymbol{x}$ (corresponding to phase terminal $\boldsymbol{a}$, $\boldsymbol{b}$, or $\boldsymbol{c}$).

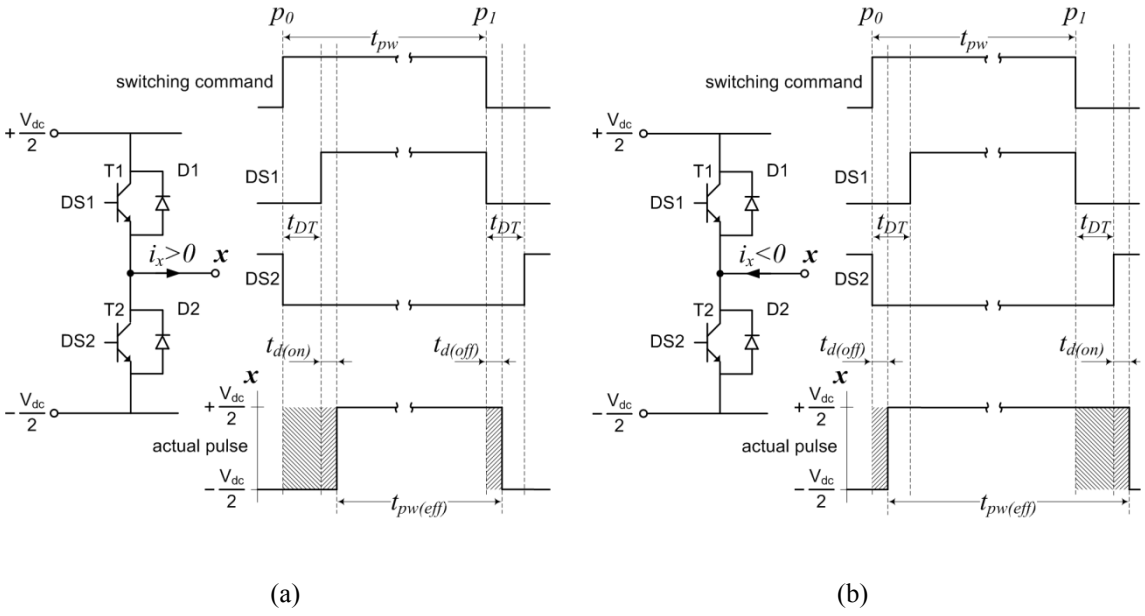

Figure 4-7: Schematic representation of single phase leg PWM inverter; (a) switching command versus effective pulse upon positive phase current; (b) switching command versus effective pulse upon negative phase current.

In Figure 4-7, the beginning and the end of the pulse switching command are denoted p_0 and p_1 respectively, and the pulse switching command duration is denoted t_{pw}. When the phase current i_x flows toward the load ($i_x > 0$), as shown in Figure 4-7a, during the dead time t_{DT} between the falling edge of DS2 and the rising edge of DS1 the freewheeling diode D2 continues the current conduction keeping the output terminal $\boldsymbol{x}$ to the negative rail ($-V_{dc}/2$) until T1 gets ON. This leads to a delay between the start of the switching command and the beginning of the effective pulse. This delay is the sum of the inverter dead time t_{DT} and transistor turn-on propagation delay time $t_{d(on)}$. Upon a transition of T1 from ON to OFF and $i_x > 0$, the freewheeling diode D2 starts conducting, whereby the potential of the output terminal $\boldsymbol{x}$ is brought from the positive

$(+V_{dc}/2)$ to the negative rail $(-V_{dc}/2)$ before T2 gets ON. Thus, the end of the effective pulse is delayed only by the transistor turn-off propagation delay time $t_{d(off)}$, see Figure 4-7a.

Considering a phase current i_x flowing from the load ($i_x < 0$), as shown in Figure 4-7b, upon a transition of T2 from ON to OFF the freewheeling diode D1 starts conduction during t_{DT} bringing the output terminal $\boldsymbol{x}$ to the positive rail $(+V_{dc}/2)$. Thus, the actual pulse is delayed only by the transistor turn-off propagation delay time $t_{d(off)}$. Upon a transition of T1 from ON to OFF and $i_x < 0$, the freewheeling diode D1 keeps conducting the current, whereby $\boldsymbol{x}$ stays at the positive rail $(+V_{dc}/2)$ until T2 gets ON. This leads to an extension of the effective pulse by $t_{DT} + t_{d(on)}$, see Figure 4-7b.

The delay times given in Figure 4-7 do not account for the signal propagation delay due to the additional circuitry between the DSP and the PWM inverter. The controller switching signals are converted and conducted through fibre-optic cable to the inverter signal interface, as demonstrated in Figure 4-8. This introduces an additional delay time t_{d1} between the controller switching command and the gate driver signals DS1 and DS2, which leads to an effective extension of the inverter dead time t_{DT} by t_{d1}. According to the manufacturers' data sheets [77]–[79], the delay time t_{d1} is estimated 210ns for signal rising edge and 280ns for signal falling edge.

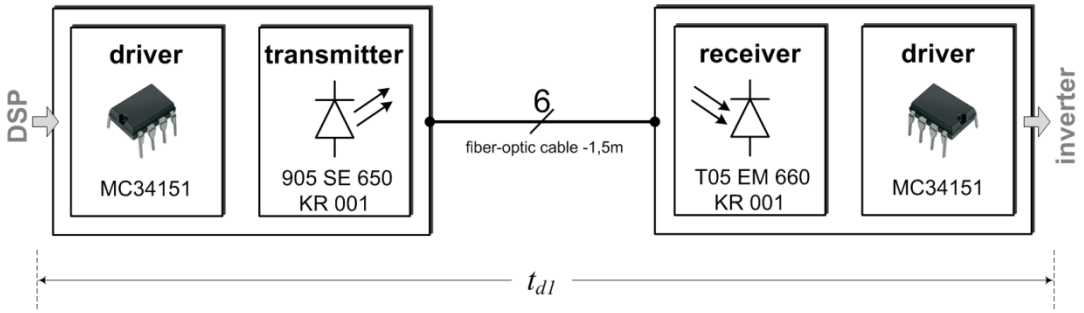

Figure 4-8: The path of the PWM signals from the DSP to the inverter; effective signal propagation delay time t_{d1} resulting from the applied circuitry.

The overall delay time between the start of a switching command and the begging of the effective voltage pulse is very important in the current investigation since this should be strongly considered upon generation of a voltage pulse in the d-axis of the motor, as explained in detail in section 5.1.1. Therefore, a total delay time denoted here as t_{td}, is introduced to combine all delay times between the beginning of the switching command and the effective voltage pulse in the machine. According to Figure 4-7 and Figure 4-8,

the total delay time t_{td} consists of t_{d1}, $t_{d(on)}$ or $t_{d(off)}$, and eventually t_{DT}, depending on the polarity of the pulse and the current in the inverter phase leg.

4.1.4 Motor Test Bench

The hardware setup used in the verification process of the proposed method is depicted in Figure 4-9. The IPMSM under test is mechanically coupled with a speed controlled load motor. A specially designed motor control unit for controlling the test machine has been implemented based on a floating point digital signal processor (C6747). The motor control unit runs a real-time field oriented current control routine as depicted in Figure 3-3. Via a graphical user interface (GUI) running on external PC, the user can define arbitrary reference values for the d- and q-current, $i_{d,ref}$ and $i_{q,ref}$.

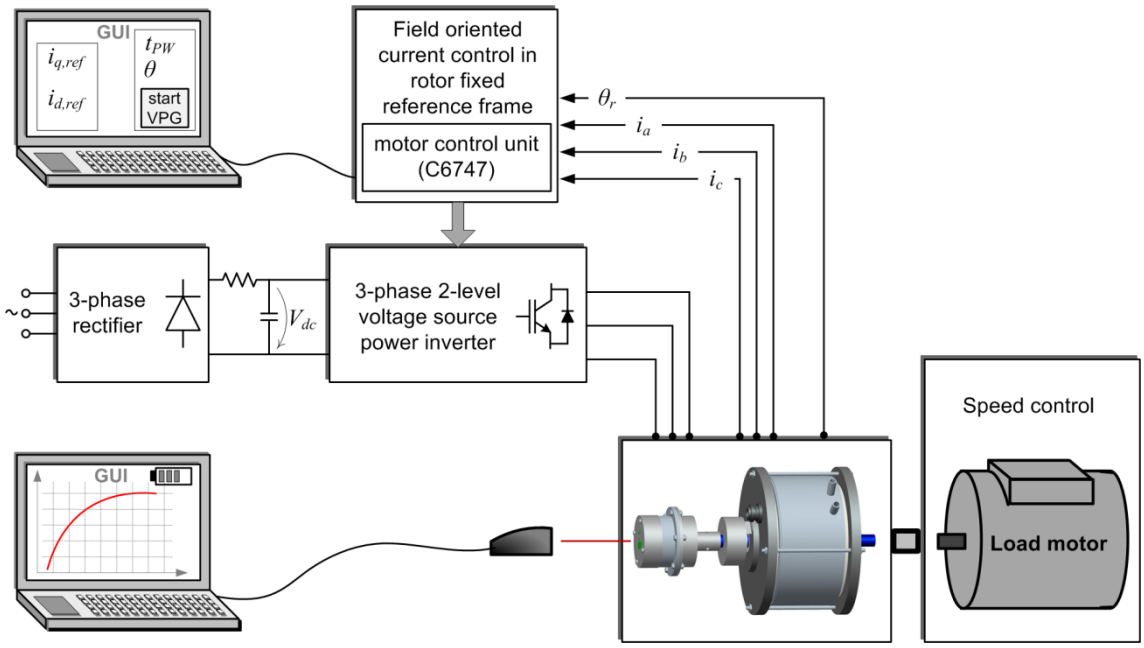

Figure 4-9: Block diagram of the motor test bench used in the current investigation.

Pulse Generation

Additionally to the current controller, a voltage pulse generator (VPG) routine is integrated into the DSP software, as demonstrated in Figure 4-10. The routine can interrupt the space vector current control routine and take the control over the inverter switching commands. The VPG software blocks are programmed to generate a desired switching pattern for a defined time duration t_{pw} that can be arbitrarily changed by the

user via the GUI. The VPG routine can either be triggered directly by the user over designated GUI commands, independent of the rotor position, or indirectly by a rotor position dependent event, see Figure 4-10. It should be noted here that the duration of a voltage pulse, also refer to as voltage pulse width t_{pw}, is meant in this work as the voltage pulse duration defined by the pulse switching commands and not the effective voltage pulse width $t_{pw(eff)}$ seen by the motor as previously discussed.

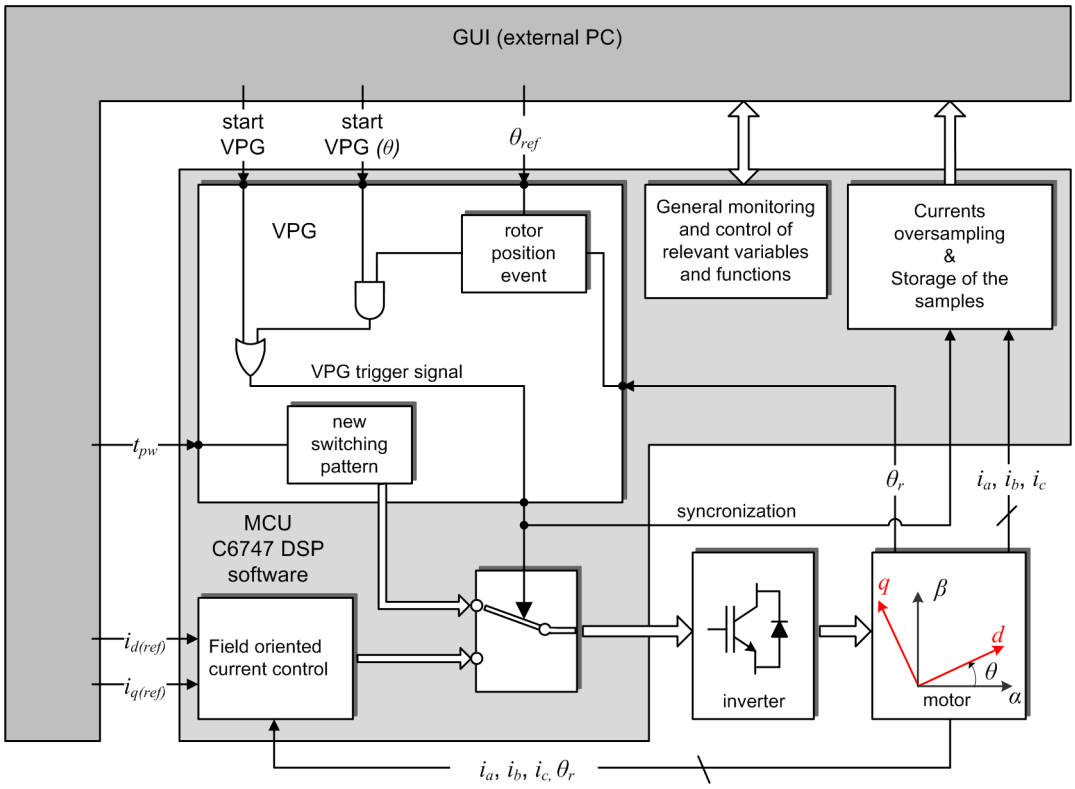

Figure 4-10: Block diagram of the motor control unit DSP software.

Currents Oversampling During Pulse Generation

Since the proposed method is based on evaluation of the d-current response upon a voltage pulse in the d-axis of the motor, an exact time trace of the motor currents during the pulse is required. This is implemented in the presented hardware by a designated oversampling mechanism which is triggered with the beginning of the VPG routine and ends automatically when the control is passed back to the field oriented current control routine. The achieved sample rate is fixed to 500ns. The obtained motor phase currents samples during a voltage pulse generation are stored into the internal memory of the DSP and passed for post processing to the GUI.

The way how the motor currents are captured along the voltage pulse is demonstrated in Figure 4-11. The following important characteristics of the implemented oversampling

mechanism should be considered when analyzing the measured current curves from the experimental setups:

- Due to technical implementation issues related to the used microcontroller, the start and end of the current oversampling is oriented on the voltage pulse switching command, as shown in Figure 4-11, and not on the effective voltage pulse in the machine under consideration of delay times as explained in Figure 4-7. Owing to the interrupt handling of the DSP, the total delay time t_{td} between the switching command and the effective voltage pulse could not be considered so that it was not possible to implement flexible oversampling mechanism oriented on the effective voltage pulse.
- The first sample s_1 of the motor currents occurs 500ns after the beginning of the switching command, while the last sample s_N occurs concurrent with the end of the switching command.
- The pulse width of the switching command signal is restricted to be a multiple of 500ns, $t_{pw} = N * 500ns$, where N is the number of samples collected along the voltage pulse switching command.

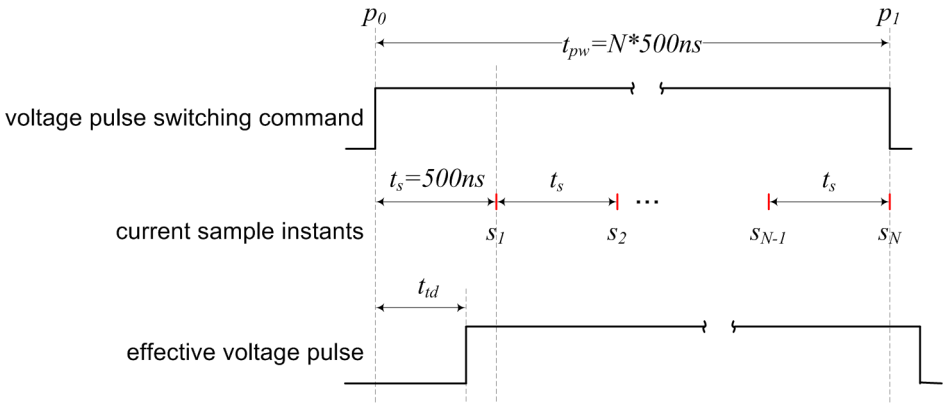

Figure 4-11: Sampling of the motor currents with respect to the voltage pulse switching command.

A detailed software and hardware description of the implemented motor control unit together with the VPG and the oversampling mechanism is given in chapter 5.

4.2 Basic Principles

The effect of the permanent magnet flux density on the saturation level of the steel stator core is the highest in direction of the magnets. This means that in the rotor

oriented reference frame (d, q), a variation of the permanent magnets magnetization will mostly affect the saturation of the stator in the d-axis of the motor. Together with the saturation level, the inductance in the d-axis of the motor will change as a result. Therefore, by applying a voltage pulse in the d-axis of the machine, the resulting current response should be mostly affected by a change of the permanent magnet magnetization in the d-axis of the machine, or in other words, the d-component of the current response will be mostly affected. In the following, a voltage pulse generation in the d-axis of the motor is discussed followed by introduction into the basic relationship between the d-current response and the temperature of the permanent magnets in the machine.

4.2.1 Generation of a Voltage Pulse in the D-axis of the Motor

The star-connected machine stator windings are fed by a conventional three-phase two-level bridge voltage source inverter as depicted in Figure 3-5. As already discussed, there are only six switching patterns that can generate non-zero dc voltage pulse in the machine corresponding to the six basic space vectors depicted in Figure 3-6. Therefore, a voltage pulse in the d-axis of the machine can be only generated by means of one of the six basic space vectors when the angle between the stator and rotor reference frame θ equals one of the basic space vectors angles, $\theta = 0°, 60°, 120°, 180°, 240°, 300°$. For the sake of clarity and a better understanding, the definition and implementation of the method is demonstrated here with pulse generation in the d-axis at $\theta = 0°$. This implies that the stator and rotor oriented reference frames are aligned $(d, q) \equiv (\alpha, \beta)$ which means that the corresponding components of the stator voltage and current space vector are equal:

$$u_d = u_\alpha \tag{4-1}$$

$$u_q = u_\beta \tag{4-2}$$

$$i_d = i_\alpha \tag{4-3}$$

$$i_q = i_\beta. \tag{4-4}$$

At standstill, when stator and rotor oriented reference frames are aligned ($\theta = 0°$), a positive and negative voltage pulse in the d-axis of machine can be achieved by applying the basic space vectors $\underline{V}_{1(100)}$ and $\underline{V}_{4(011)}$ respectively, see Figure 3-6. The corresponding switching patterns with time duration t_{pw} are demonstrated in Figure 4-12. Thus, formulated in the rotor oriented reference frame, the resulting voltage space

vector applied to the motor terminals has the following components for a positive voltage pulse:

$$u_{dP} = \frac{2}{3} V_{dc} \tag{4-5}$$

$$u_{qP} = 0, \tag{4-6}$$

and for a negative voltage pulse:

$$u_{dN} = -\frac{2}{3} V_{dc} \tag{4-7}$$

$$u_{qN} = 0. \tag{4-8}$$

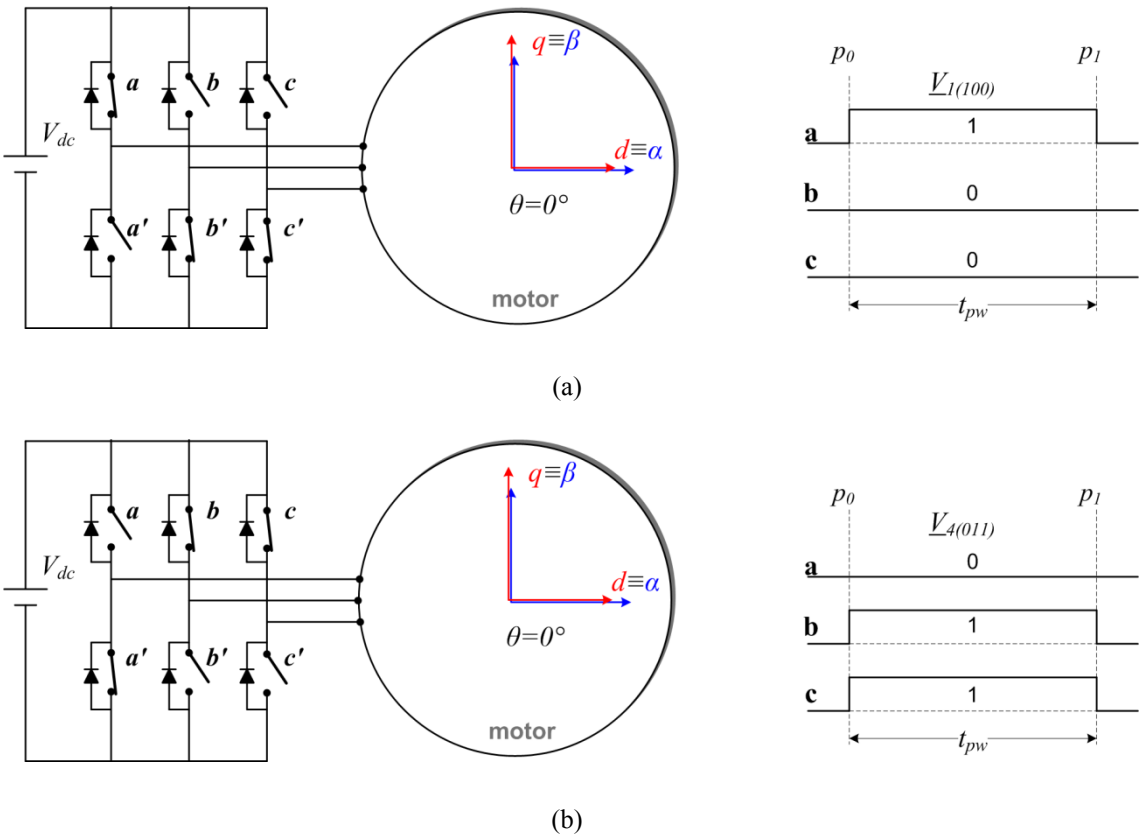

Figure 4-12: Generation of a dc voltage pulse in the d-axis of the machine at standstill upon $\theta = 0°$; (a) switching pattern of the positive voltage pulse; (b) switching pattern of the negative voltage pulse.

In a rotating machine, the voltage pulse is applied in phase $\boldsymbol{a}$ of the machine such that the electrical rotor position gets zero ($\theta = 0$) in the middle of the pulse, as depicted in Figure 4-13. The angles (θ_0, θ_1) between the rotor and stator reference frames at the time instant of the beginning p_0 and the end p_1 of the voltage pulse for a given machine with P pole pairs depend on the speed n [rps] and the voltage pulse width t_{pw} [s], as follows:

$$\theta_0 = \theta_1 = \frac{1}{2} 360° P n t_{pw}. \tag{4-9}$$

This means, that in a rotating machine the expressions given in (4-1)-(4-4) for the motor current and voltage space vector components and in (4-5)-(4-8) for the effective values of the voltage components at standstill can still be considered valid for the duration of the voltage pulse as long as the angles θ_0 and θ_1 are kept small enough. This implies a voltage pulse with a time duration t_{pw} which is short enough with respect to the motor speed and the number of pole pairs according to (4-9).

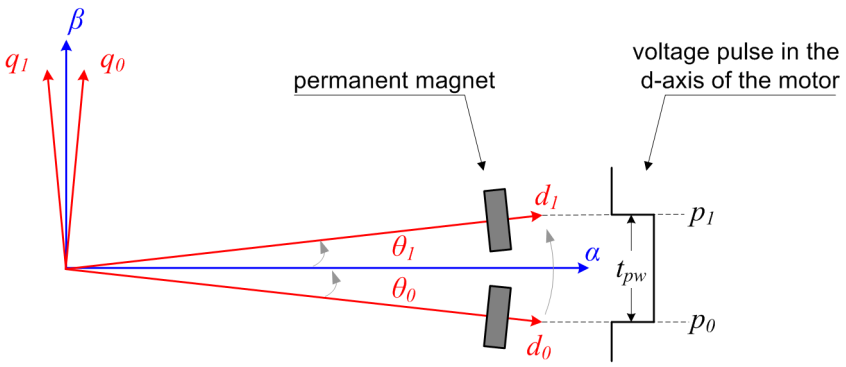

Figure 4-13: D-axis voltage pulse generation in a rotating machine neglecting the delay times between the switching command and the effective voltage pulse; relative displacement of the d-axis along the voltage pulse duration.

4.2.2 D-current Response upon Positive Voltage Pulse in the D-axis of the Motor

In the following, the slope of the d-current response di_d/dt upon a positive voltage pulse in the d-axis of the motor at standstill is examined. The alignment of the rotor and the stator reference frame, as illustrated in Figure 4-12, is achieved by applying a stationary, not rotating, reference voltage space vector $\underline{u}_{s,ref}$ with zero degree angle and amplitude to produce as much as enough a current space vector to align the magnets with the motor phase $\boldsymbol{a}$. While applying a positive voltage pulse in the d-axis of the

motor at three different reference magnet temperatures $T_m = 25°C, 70°C, 120°C$, the currents of the motor are simultaneously sampled with 2MHz synchronously with respect to the beginning of the voltage pulse switching command, as it has been explained in 4.1.4. The duration of the voltage pulse t_{pw} is set to 240µs so that a large current response is generated in the IPMSM under test that clearly visualizes saturation effects in the d-axis of the machine. The time trace of the resulting i_d and i_q are depicted in Figure 4-14a and Figure 4-14b respectively.

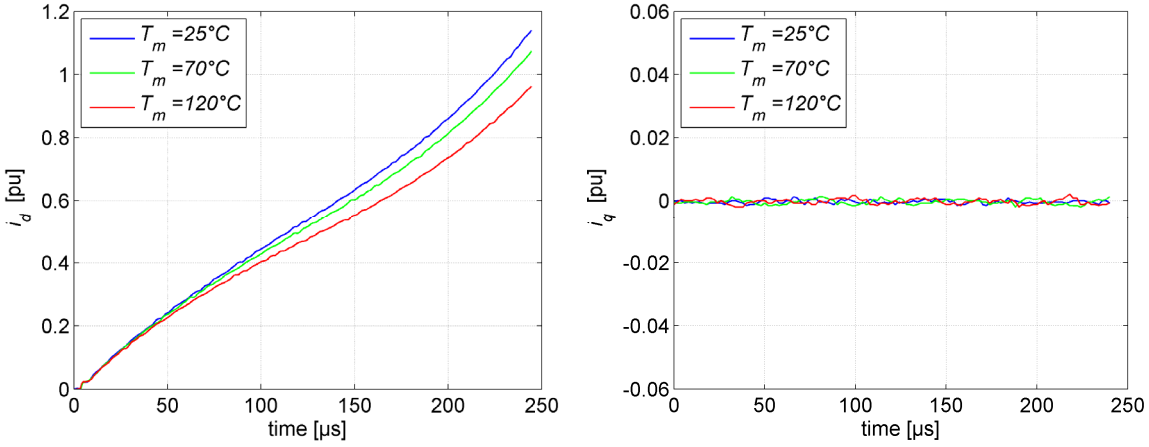

Figure 4-14: Current response upon voltage pulse in the d-axis of the motor at standstill ($t_{pw} = 240\mu s$; $V_{dc} = 650V$). The motor under test is an IPMSM with aligned stator and rotor reference frame; (a) d-current response; (b) q-current response.

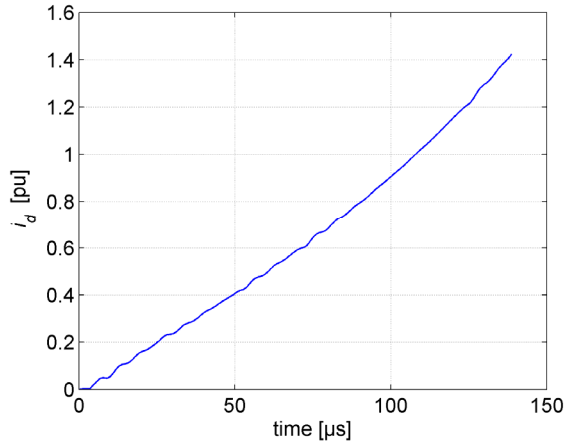

Figure 4-15: D-current response upon voltage pulse in the d-axis of the motor at standstill ($t_{pw} = 140\mu s$, $V_{dc} = 650V$) at $T_m = 25°C$. The motor under test is an SPMSM with aligned stator and rotor reference frame.

Under the same conditions but using a shorter voltage pulse of 140µs, the d-current response of a SPMSM is captured in Figure 4-15. Considering the obtained d-current response curves from Figure 4-14 and Figure 4-15 the gradient of a current curve is predominantly influence by two basic factors:

- The gradient of the d-current curve increases while the d-current i_d grows due to the applied voltage pulse in the positive d-axis of the machine, as it can be observed in Figure 4-15. The d-inductance of the machine gets smaller along the pulse because of the increased saturation level in the d-axis caused by the additional stator flux linkage produced by the d-current excitation, as visualized in Figure 4-16. In Figure 4-14a the gradient of a d-current response first decreases before starting to increase at about 100µs. This is a particular behaviour of the IPMSM under test that is not investigated further here as it not subject of the current thesis. All other tested machines demonstrated a behaviour as in Figure 4-15.
- The gradient of the current curve decreases while the temperature increases, as it can be observed in Figure 4-14a. This is because the portion of the stator flux linkage produced by the permanent magnet flux sinks due to temperature dependent demagnetization effects. Consequently the saturation level decreases and the motor inductance in the d-axis increases.

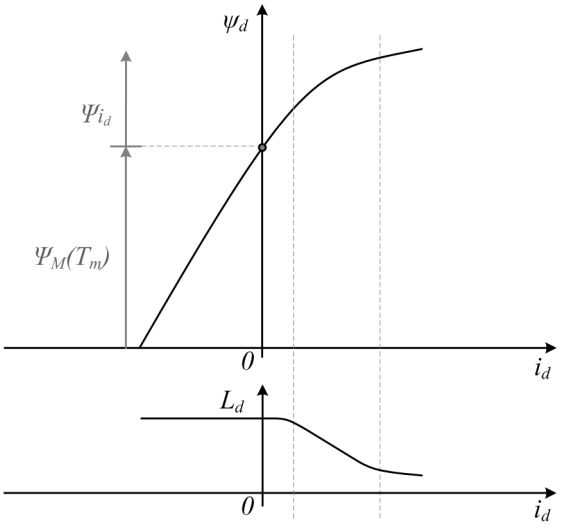

Figure 4-16: Flux saturation effects in the d-axis of the motor due to permanent magnet flux linkage and the d-current excitation ($i_q = 0$).

Thus, when the q-current is zero, it can be concluded that the d-current slope di_d/dt is a function of the d-current i_d itself and the temperature of the permanent magnets T_m:

$$\frac{di_d}{dt} = f_{i_q=0}(i_d, T_m). \tag{4-10}$$

By inverting (4-10), a relationship for the magnet temperature T_m can be obtained as follows:

$$T_m = f_{i_q=0}\left(i_d, \frac{di_d}{dt}\right). \tag{4-11}$$

The function expressed in (4-11) is characterized by a strong non-linearity since it reflects saturation effects produced by the permanent magnet excitation and the d-current excitation. However, the degree of non-linearity depends strongly on the design and construction type and especially on the size of the effective air gap of the machine. A bigger effective air-gap will reduce the stator reactance and consequently the effect of the d-current i_d in (4-11). Therefore, it is expected that for a SPMSM the degree of linearity of (4-11) will be higher than for an IPMSM, which will result in relative easier method commissioning. However, the demonstrated validation of the proposed magnet temperature estimation discussed next is carried out solely on IPMSM. This is intentional in order to prove method feasibility on strongly non-linear machine type.

In the following sections, three basic implementation approaches of the proposed magnet temperature estimation in IPMSM will be discussed. The first approach implies magnet temperature estimation based on a single voltage pulse in the positive d-axis of the motor. The second approach deals with the speed dependency that influences the accuracy of the temperature estimation especially in machines with high stator reactance and cross-coupling saturation effects. A speed compensation methodology applying a combination of a positive and negative d-axis voltage pulse will be demonstrated that overcomes the undesired dependency. A common requirement of these two approaches is zero q-current ($i_q = 0$) in the machine at the beginning of each voltage pulse upon magnet temperature estimation. The third approach demonstrates magnet temperature estimation with non-zero q-current ($i_q \neq 0$) in the machine. Analytical discussions of all three methodologies will be given followed by demonstration and discussion of experimental results conducted at low speed (n=0÷300rpm) and at high speed (n=3000÷4800rpm).

4.3 Sensorless Magnet Temperature Estimation with a Single Positive Voltage Pulse in the D-axis of the Motor at Zero Load

In this section, an estimation of the permanent magnets temperature in IPMSM will be demonstrated based on a single voltage pulse applied in the machine with q-current set to zero at the beginning of the pulse, ($i_q = 0$). An analytical approach is given first where the motor equations are discussed with respect to a voltage pulse in the positive d-axis of the motor and an initial q-current set to zero by the current controller, ($i_{q,ref} = 0$). Experimental results for the d-current response at various reference magnet temperatures will be presented for various speeds, followed by discussions on commissioning procedures and method sensitivity and robustness.

4.3.1 Motor Equations upon a Positive Voltage Pulse in the D-axis of the Motor

The presented method proposes a magnet temperature estimation procedure based on an application of a voltage pulse in the d-axis of the machine, whereby the resulting the d-current response is measured and the corresponding d-current slope di_d/dt is used as indicator for the magnet temperature. The approach leans on the following two main assumptions:

- As already mentioned before, the influence of the permanent magnet magnetization level on the saturation of the machine is the strongest its d-axis. This implies the highest dependency of the d-current slope di_d/dt from the permanent magnet magnetization level and consequently from the temperature of the magnets.
- The d-current response is not affected by the back electromotive force.

Since the influence of the q-current on the magnet temperature estimation is excluded from the analysis presented in the current section, for the sake of a better understanding the motor equations (3-21) and (3-22) that do not account for cross-coupling saturation effects are considered. For convenience, the motor equations are given here again:

$$u_d = R_s i_d + \underbrace{\left(\frac{dL_d}{di_d} i_d + L_d\right)}_{L_d^*} \frac{di_d}{dt} - \omega L_q i_q \tag{4-12}$$

$$u_q = R_s i_q + \underbrace{\left(\frac{dL_q}{di_q} i_q + L_q\right)}_{L_q^*} \frac{di_q}{dt} + \omega L_d i_d + \omega \psi_M. \tag{4-13}$$

If a voltage pulse is generated in the positive d-axis of the motor when the rotor and stator reference frames are aligned ($\theta = 0$), the applied voltage space vector on the motor terminals has the components $u_d = 2/3 V_{dc}$ and $u_q = 0$. Thus, the motor equations (4-12) and (4-13) become:

$$\frac{2}{3} V_{dc} = R_s i_d + L_d^* \frac{di_d}{dt} - \omega L_q i_q \tag{4-14}$$

$$0 = R_s i_q + L_q^* \frac{di_q}{dt} + \omega L_d i_d + \omega \psi_M. \tag{4-15}$$

At standstill, the equations (4-14) and (4-15) describe the momentary state of the machine upon a voltage pulse in the d-axis of the motor at $\theta = 0$. However they can be considered valid in a rotating machine as long as the voltage pulse time duration is small enough with respect to the speed and the number of pole pairs of the machine according to (4-9), so that the displacement between the rotor and stator reference frames at the beginning and the end of the voltage pulse can be neglected, see Figure 4-13.

Basically, the proposed method exploits the resulting relationship from (4-14). It is subject to the condition that at the beginning of the voltage pulse the q-current is zero ($i_q = 0$) in the machine. Thus, by neglecting the stator resistance voltage drop, equation (4-14) becomes:

$$L_d^* \frac{di_d}{dt} = \frac{2}{3} V_{dc}. \tag{4-16}$$

Since cross-coupling effects are neglected at this point, it can be assumed that the differential inductance L_d^* is predominantly affected by the saturation level in the d-axis of the machine, which is in turn influenced by the d-current i_d and the magnetization level of the permanent magnets. When the d-current slope di_d/dt is measured along the voltage pulse, variation of L_d^* can be detected. Thus, the d-current slope di_d/dt will change upon changes in the magnetization level of the magnets. Since the magnetization of the magnets is temperature dependent, a given d-current slope di_d/dt can be associated with a given magnet temperature T_m as long as no other factors influence the

magnet magnetization. If the permanent magnets are operated in the machine in a temperature range where only reversible change of the magnet magnetization occur, the d-current slope di_d/dt can be used as indicator for the magnet temperature T_m. A distinctive relationship between di_d/dt and T_m can be established for a given machine by a look-up-table (LUT). This is because the relationship expressed in (4-16) has generally a non-linear character. A LUT is identified during a commissioning phase either by direct measurements of T_m and di_d/dt or by setting constant reference temperature values in the rotor while measuring di_d/dt, as it will be explained later.

In the present investigation, the winding currents are controlled in a way that a constant reference temperature is established across the magnets. This is monitored by the rotor temperature monitoring device. Thus, at a given reference magnet temperature, the current control is interrupted for short period test pulse procedures to measure the d-current response di_d/dt with respect to T_m upon a positive voltage pulse in the d-axis of the machine.

4.3.2 Tuning Aspects of a Magnet Temperature Estimation with a Single Positive Voltage Pulse in the D-axis of the Motor

There are two controllable parameters that significantly influence the sensitivity and the robustness of a magnet temperature estimation based on the relationship from (4-16). On the one hand, this is the time duration t_{pw} of the voltage pulse applied in the d-axis. On the other hand, this is the initial d-current in the machine at the beginning of the voltage pulse. Both parameters can be meaningfully controlled in order to obtain a desired sensitivity of a magnet temperature estimation procedure for a given machine, as it is explained next.

Adjustment of Voltage Pulse Width - t_{pw}

For a particular machine and desired speed range, the voltage pulse width t_{pw} should be carefully selected according to the following discussions. Generally it is valid that the bigger the voltage pulse width t_{pw}, the more distinctive is the difference in the d-current response between two different reference magnet temperatures, which makes easier to associate a d-current slope di_d/dt to a given magnet temperature level T_m. In order to visualize this a voltage pulse with relatively long time duration, $t_{pw} = 200\mu s$, is applied in the machine at standstill and at magnet temperatures of 20°C and 60°C, see Figure 4-17. As expected, the deviation between the two current curves increased progressively along the voltage pulse.

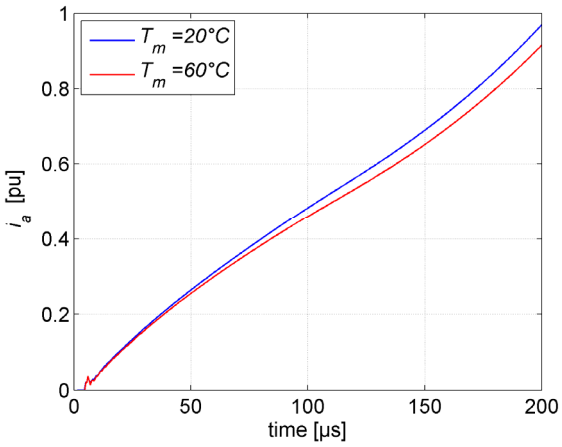

Figure 4-17: Current i_a response upon voltage pulse of 200µs in the motor d-axis at standstill and at no load; d- current initial value $i_{d,ref} = 0$; $V_{dc} = 750$V.

However, if the voltage pulse width t_{pw} is selected too big with respect to the maximum operating speed, in a rotating machine the displacement between the rotor and stator reference frames within the voltage pulse cannot be neglected, see Figure 4-13. It is assumed here that along the voltage pulse, the α-axis of the motor should see quasi the same permanent magnet flux linkage in the rotating machine as at standstill. Therefore, according to Figure 4-13, the angles θ_0 and θ_1 should be kept small enough which implies a short possible voltage pulse. It should be noted here that once the voltage pulse width t_{pw} is defined for a given machine it should be kept the same at all motor speeds.

Figure 4-18 demonstrates the influence of the speed on the current response, where at a constant magnet temperature, $T_m = 70°C$, a relative long voltage pulse of 100µs is applied in the d-axis of the motor at low and high speed (n=100rpm and n=4800rpm).

Apart from the considerations concerning the permanent magnet flux linkage, the speed influences the d-current response indirectly over the q-current that will develop in the machine along the voltage pulse. At higher speeds, according to (4-15) the voltage terms $\omega L_d i_d$ and $\omega \psi_M$ will produce a negative q-current along the voltage pulse duration. The q-current response is depicted in Figure 4-18b. The q-current i_q produces a speed dependent voltage term in the d-axis of the motor and an additional voltage term as a result of the change of the flux excitation in the d-axis produced by the change of i_q. Thus, the speed and the resulting q-current developed along the voltage pulse will indirectly influence the d-current response. The voltage pulse should be kept small in order to avoid significant q-current increase. The speed dependency resulting from the

q-current rise along the voltage pulse will be discussed in detail in section 4.4. Additional advantage of using relative short voltage pulse width is to keep the resulted d-current response as small as possible for less influence on the motor performance. In the experimental validation, both a setup with a small and a setup with a big voltage pulse width will be demonstrated and discussed.

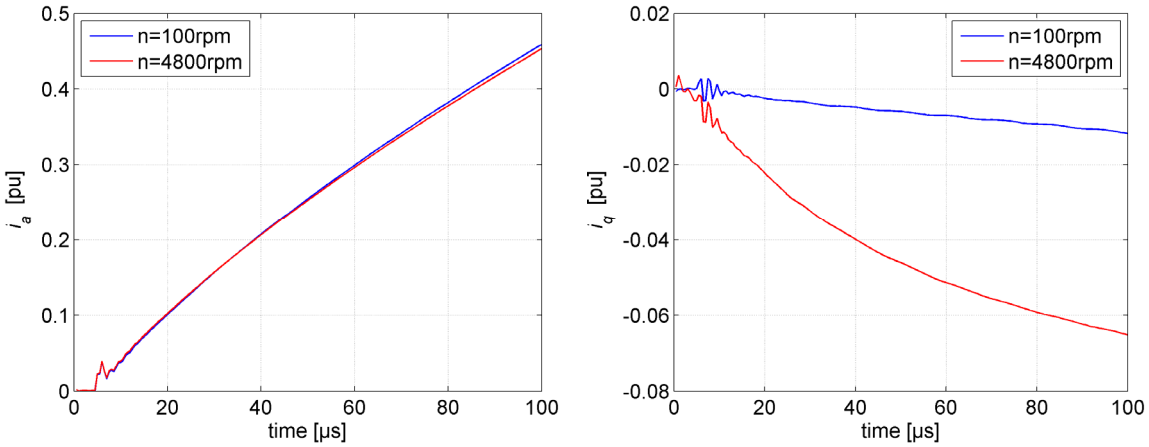

Figure 4-18: Current response upon voltage pulse of 100µs in the motor d-axis at no load, with d-current initial value $i_{d,ref} = 0$ and q-current initial value $i_{q,ref} = 0$; n=100rpm and n=4800rpm at $T_m = 70°C$; $V_{dc} = 750V$; (a) d-current response; (b) q-current response.

Selecting Initial d-current - $i_{d,ref}$

The initial d-current available in the machine at the beginning of a voltage pulse can be assumed equal to the reference d-current $i_{d,ref}$ set by d-current controller of the field oriented control scheme. The initial d-current $i_{d,ref}$ has a significant influence on the sensitivity of the d-current response with respect to the magnet temperature T_m, since by varying $i_{d,ref}$ different initial saturation levels in the d-axis of the motor can be set before a voltage pulse is generated.

Figure 4-19 demonstrates a simplified presentation of flux saturation effects that occur in the machine upon voltage pulse injection in the d-axis of the motor while the q-current is assumed zero, $i_{q,ref} = 0$. Once the pulse width is set for a given machine, $t_{pw} = const$, an initial d-current $i_{d,ref}$ provides the most sensitivity when the difference of the d-current slopes di_d/dt at two different temperatures is the highest. This is the case when the inductance in the d-axis of the motor starts to decline or in other words, when the stator core starts to saturate strongly in the d-axis, as exemplary visualized in Figure 4-19.

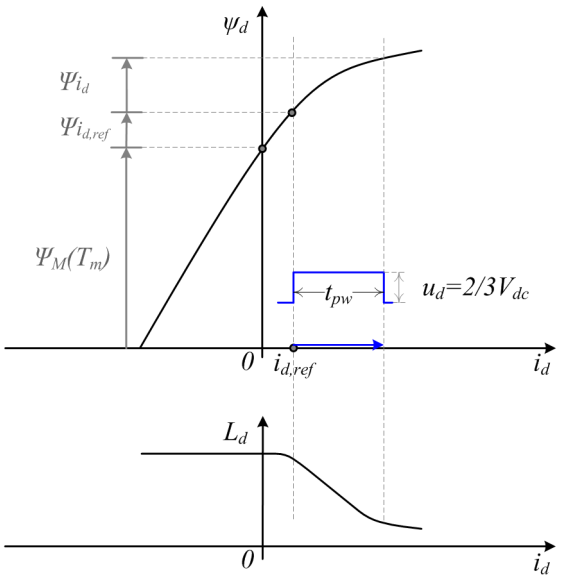

Figure 4-19: Simplified presentation of flux saturation effects in the d-axis of the motor caused by the permanent magnet flux linkage ψ_M, the initial d-current excitation $\psi_{i_{d,ref}}$ and the d-current excitation ψ_{i_d} along the voltage pulse; $i_{q,ref} = 0$.

The optimal $i_{d,ref}$ with respect to the magnet temperature estimation for a given pulse width t_{pw} depends strongly on the machine design, and more precisely on how strong the steel stator laminated core saturates in the d-axis.

4.3.3 Quantitative Estimation of the D-current Response

Since the d-current slope di_d/dt is used as indicator for the magnet temperature in the proposed method, the sensitivity of the magnet temperature estimation depends strongly on the precise evaluation of di_d/dt. In the present investigation standard current sensors are used, whereby a quantitative estimation of a current slope can be realized by linearisation of the current curve using polynomial interpolation or by approximation with difference quotient calculation.

Current Curve Linearisation by Polynomial Interpolation

The d-current slope di_d/dt can be approximated by linearising the exact time trace of the d-current response i_d. It should be reminded here that a d-axis voltage pulse is generated upon alignment of the rotor and stator reference frames ($\theta = 0$), see Figure 4-12 and Figure 4-13, which means $i_d \approx i_a$ as long as the voltage pulse is of relatively short duration. Thus, the d-current slope di_d/dt is obtained by oversampling the phase

current i_a along the voltage pulse and linearising the resulting curve using polynomial interpolation:

$$y(t) = S_a t + P, \tag{4-17}$$

where the weighting factor S_a represents the approximated slope of the i_a current curve and the offset P represents the value of i_a at the beginning of the voltage pulse, which is assumed to be almost equal the initial d-current, ($P \approx i_{d,ref}$).

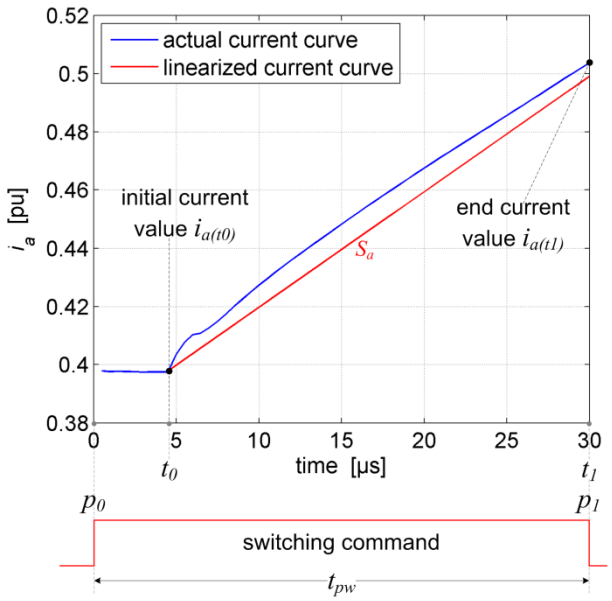

Figure 4-20: D-current response upon voltage pulse of 30µs in the motor d-axis at standstill; with d-current initial value $i_{d,ref} = 0.4$pu and q-current initial value $i_{q,ref} = 0$; $T_m = 20$°C; $V_{dc} = 750$V.

Figure 4-20 shows an actual current curve versus its linearised counterpart for the case of voltage pulse generation in the d-axis with $i_{d,ref} = 0.4$pu and $t_{pw} = 30\mu s$. The linearisation is conducted on the effective current curve. As already explained in 4.1.3, there is a total delay t_{td} between the beginning of the switching command and the effective voltage pulse applied on the motor terminals. Furthermore, the sampling of the motor currents starts and ends with the switching command, as described in 4.1.4. Therefore, as effective current curve is considered here the part of the measured current time trace along the switching command duration t_{pw} that is directly affected by the resulting effective voltage pulse on the machine terminals. According to Figure 4-20, this is part of the curve defined between the values $i_{a(t0)}$ and $i_{a(t1)}$. Thus, the approximated current slope S_a is obtained by using linear regression calculation using all current samples captured every 500ns between the time instant t_0 and t_1. The

calculation by linear regression is explained in detail in section 5.1.1. The calculated current slope S_a is then used as indicator for the magnet temperature T_m in the current investigation.

It should be noted here that the delay between the beginning of the switching command and the effective current curve in Figure 4-20 is a result of the total delay time t_{td} between the switching command and the effective voltage pulse, and the current sensor response time t_{resp}. For the setup demonstrated in Figure 4-20, which implies positive current and positive voltage pulse in the machine, according to the discussions made in section 4.1.3 the total delay time t_{td} between the beginning of the switching command and the effective voltage pulse is estimated to be $t_{td} = t_{d1} + t_{DT} + t_{d(on)} \approx 4{,}20\mu s$. In manufacturer's data sheets [75], the current sensor response time is only given to be $t_{resp} < 1\mu s$.

Slope Approximation by Difference Quotient Calculation

Apart from the linearisation approach, a slope approximation can be carried out by calculating solely the difference quotient (4-18)

$$\frac{\Delta i_a}{\Delta t} = \frac{i_{a(t_1)} - i_{a(t_0)}}{t_1 - t_0} \ , \tag{4-18}$$

where only two samples of the current response are required, one sample at the beginning $i_{a(t_0)}$ and one sample at the end $i_{a(t_1)}$ of the effective current curve according to Figure 4-20. Calculating the difference quotient is generally characterized by lower slope estimation precision, therefore in the present investigation a preference is given to the current curve linearisation approach using a slope approximation S_a. For the purpose of comparison, slope approximation based on both $\Delta i_a/\Delta t$ and S_a will be given later in this chapter where the distribution and repetitiveness of the current response measurements with respect to a reference magnet temperature are discussed in detail for different method's operating points.

4.3.4 Sensitivity and Robustness Issues

In the following, an investigation is conducted to define the optimal operating conditions for the machine under test with respect to the highest possible sensitivity for a magnet temperature estimation procedure based on a single positive voltage pulse in the d-axis of the motor. For the purpose, the difference of d-current responses for two different magnet temperatures, and various initial d-current values $i_{d,ref}$ and different

voltage pulse widths t_{pw} is measured. The goal is to recognize an optimal combination of $i_{d,ref}$ and t_{pw} that provides a d-current response characterized with highest sensitivity with respect to the magnet temperature T_m. Furthermore, three setups characterized with highest possible sensitivity but with different voltage pulse widths will be demonstrated in order to investigate the distribution of the obtained measurements and the influence of the motor speed on the d-current response.

The current slopes S_a for two reference magnet temperatures, $T_m = 20°\text{C}$ and $T_m = 60°\text{C}$, are captured at standstill using voltage pulse width t_{pw} varying from 30µs to 100µs and initial d-current $i_{d,ref}$ between 0.2pu and 0.5pu. These ranges have been preliminary recognized as meaningful for the IPMSM under tests. The machine needs additional d-current excitation prior to the voltage pulse generation, so that the saturation level of the machine in its d-axis can be elevated to the area of most sensitivity with respect to T_m. The differences between $S_{a(T_m=20°C)}$ and $S_{a(T_m=60°C)}$ for the resulting combinations of $i_{d,ref}$ and t_{pw} are depicted in Figure 4-21. The plot demonstrates an approach how to tune and optimize a magnet temperature estimation procedure based on a single positive voltage pulse in the d-axis of the machine.

According to Figure 4-21, for the combination $i_{d,ref} = 0.4\text{pu}$ and $t_{pw} = 30\mu s$, the difference between the current slopes $S_{a(T_m=20°C)}$ and $S_{a(T_m=60°C)}$ is the biggest, which would imply at first sight the highest sensitivity for a magnet temperature estimation procedure among all investigated combinations of $i_{d,ref}$ and t_{pw}. However, as already mentioned before, the pulse width should be long enough in order to produce a distinctive d-current response. Therefore, the method's sensitivity should be also validated and discussed with respect to t_{pw}. For the purpose, three combinations of $i_{d,ref}$ and t_{pw} are investigated in detail characterized by relatively short, medium and long voltage pulse duration with respect to the machine under test. Thus, the following three combinations are considered:

- setup 1: $t_{pw} = 30\mu s$ and $i_{d,ref} = 0.4\text{pu}$
- setup 2: $t_{pw} = 50\mu s$ and $i_{d,ref} = 0.35\text{pu}$
- setup 3: $t_{pw} = 90\mu s$ and $i_{d,ref} = 0.3\text{pu}$

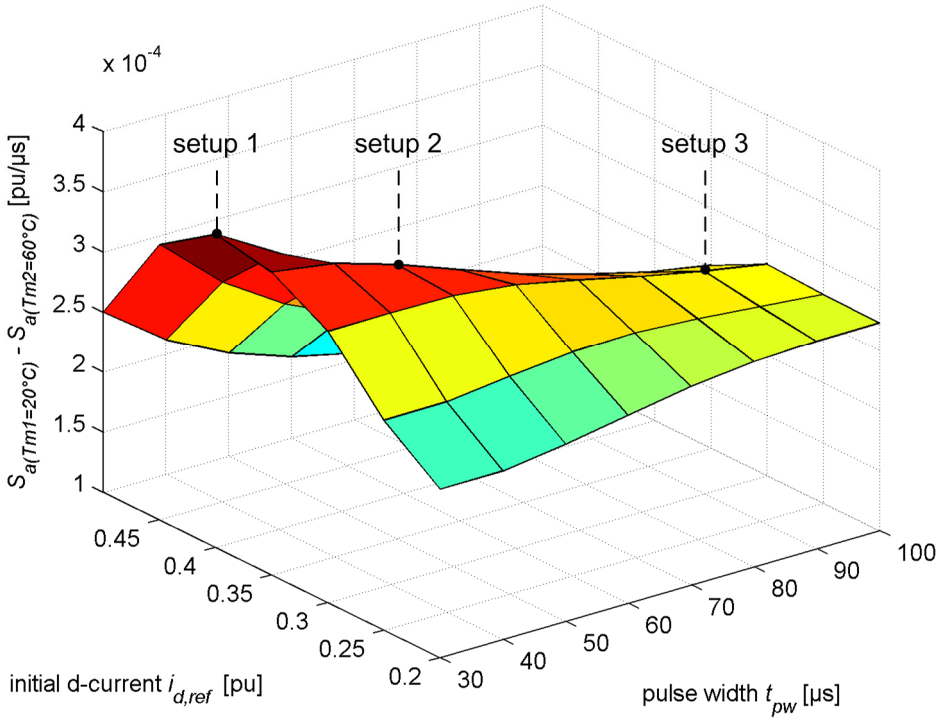

Figure 4-21: The difference of the approximated current slopes S_a between two reference magnet temperatures ($T_{m1} = 20°C$ and $T_{m2} = 60°C$) as a function of the initial d-current $i_{d,ref}$ and the pulse width t_{pw} of the applied d-axis voltage pulse; standstill; $V_{dc} = 750\text{V}$.

As Figure 4-21 shows, the selected combinations will characterize with the biggest difference between the current slopes $S_{a(T_{m1}=20°C)}$ and $S_{a(T_{m2}=60°C)}$ for the corresponding voltage pulse width t_{pw}. The experimental setups are carried out to investigate the relationship between t_{pw} and the influence of the speed on the magnet temperature estimation, and the effect of t_{pw} on the repetitiveness and distribution of the current slope measurements for a given reference magnet temperature.

Setup 1: $t_{pw} = 30\mu s$ and $i_{d,ref} = 0.4\text{pu}$

This setup is characterized by a relative short voltage pulse with respect to the nominal speed of the motor under test and highest method's sensitivity with respect to the selected reference d-current $i_{d,ref}$. The reference magnet temperatures at which the measurements are carried out are given in Table 4-6. A reference magnet temperature is set in the machine by controlling the motor winding currents in a manner that a constant temperature is established across the magnets. This is interrupted for short period test

measurements only. It should be noted that the reference temperature values, at which the measurements are carried out, are not necessarily equidistant since it resulted very cumbersome to keep a desired reference magnet temperature constant for a long time, especially at low and high magnet temperatures, see Table 4-6.

Table 4-6: Setup 1 ($t_{\mathrm{pw}} = 30\mu\mathrm{s}$, $i_{d,ref} = 0.4\mathrm{pu}$): Reference magnet temperatures.

motor speed [rpm]	T_{m1} [°C]	T_{m2} [°C]	T_{m3} [°C]	T_{m4} [°C]	T_{m5} [°C]	T_{m6} [°C]	T_{m7} [°C]	T_{m8} [°C]	T_{m9} [°C]	T_{m10} [°C]	T_{m11} [°C]
n=100	21	30	40	50	60	70	80	90	100	110	117
n=4800	22	30	40	50	60	70	80	90	100	110	119

The d-current responses at each investigated reference magnet temperature T_m are depicted in Figure 4-22a for motor speed n=100rpm, while their linearised counterparts are given in Figure 4-22b. In order to demonstrate the influence of the motor speed on the d-current slope di_d/dt, the d-current responses obtained at motor speed n=100rpm and n=4800rpm are depicted in Figure 4-23 for reference magnet temperature $T_m = 60°\mathrm{C}$.

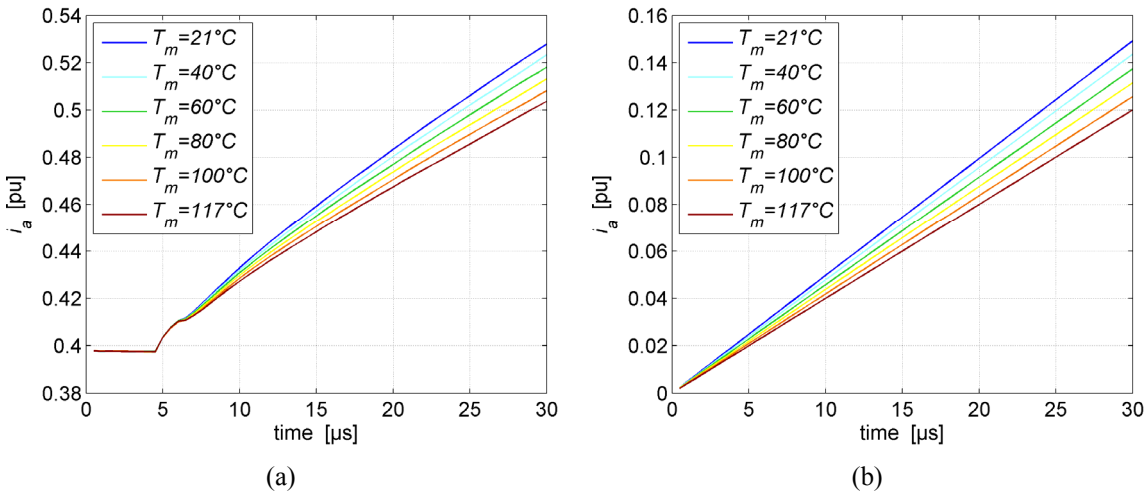

Figure 4-22: The d-current i_d response upon positive voltage pulse in the d-axis of the motor; $t_{\mathrm{pw}} = 30\mu\mathrm{s}$ and $i_{d,ref} = 0.4\mathrm{pu}$; $V_{\mathrm{dc}} = 750\mathrm{V}$; (a) measured current response at various magnet temperatures and motor speed n=100rpm; sample rate 500ns; (b) linearisation of the measured current response by polynomial interpolation with eliminated offset.

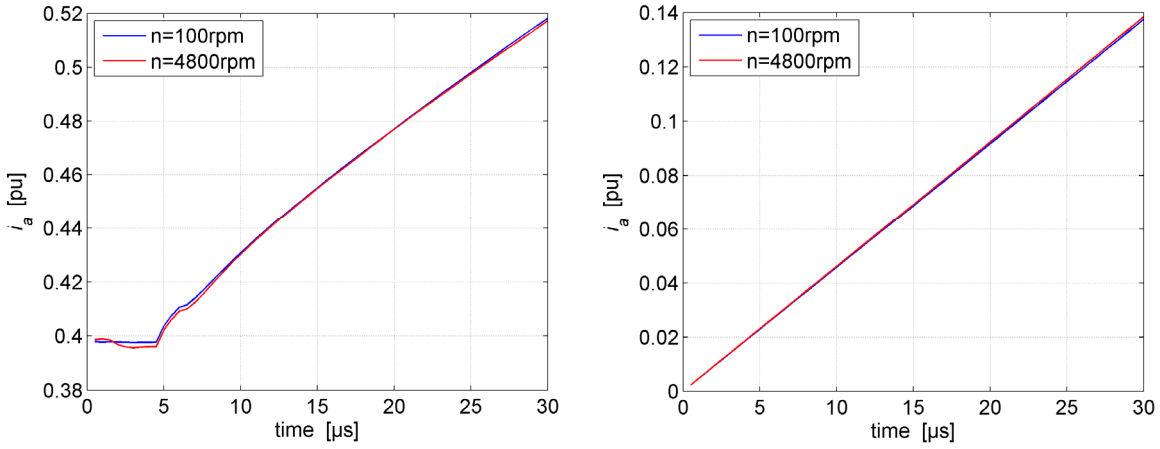

Figure 4-23: The d-current i_d response upon positive voltage pulse in the d-axis of the motor; $t_{\mathrm{pw}} = 30\mu s$ and $i_{d,ref} = 0.4\mathrm{pu}$; magnet temperature $T_m = 60°\mathrm{C}$; $V_{\mathrm{dc}} = 750\mathrm{V}$; (a) measured current response at motor speed n=100rpm and n=4800rpm; sample rate 500ns; (b) linearisation of the measured current response by polynomial interpolation with eliminated offset.

A set of 50 measurements are carried out at each reference magnet temperature, and motor speed n=100rpm and n=4800rpm. The time interval between two measurements is set to 50ms, whereby the completion of 50 measurements varies between 7 to 10 seconds. Within this time, the temperature of the magnets does not change significantly and can be assumed constant. Thus, the mean values of the approximated d-current slopes S_a are given in Figure 4-24 as a function of the magnet temperature for motor speed n=100rpm and n=4800rpm.

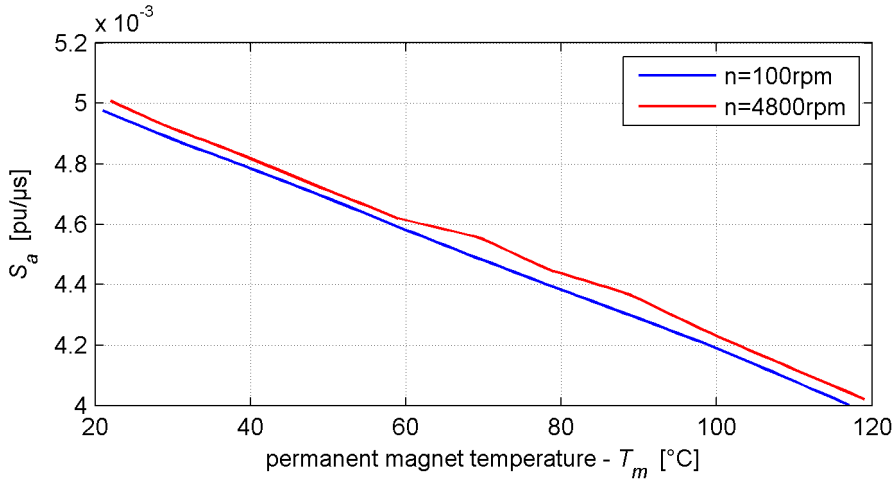

Figure 4-24: Approximated d-current slopes S_a as a function of the magnet temperature T_m for motor speed n=100rpm and n=4800rpm; setup 1: $t_{\mathrm{pw}} = 30\mu s$ and $i_{d,ref} = 0.4\mathrm{pu}$.

The distribution of the approximated d-current slopes S_a obtained from the 50 measurements conducted at each reference magnet temperature T_m and motor speed n=100rpm is given as histogram plot in Figure 4-25. The grey line drawn through a distribution indicates the mean value of S_a for each magnet temperature.

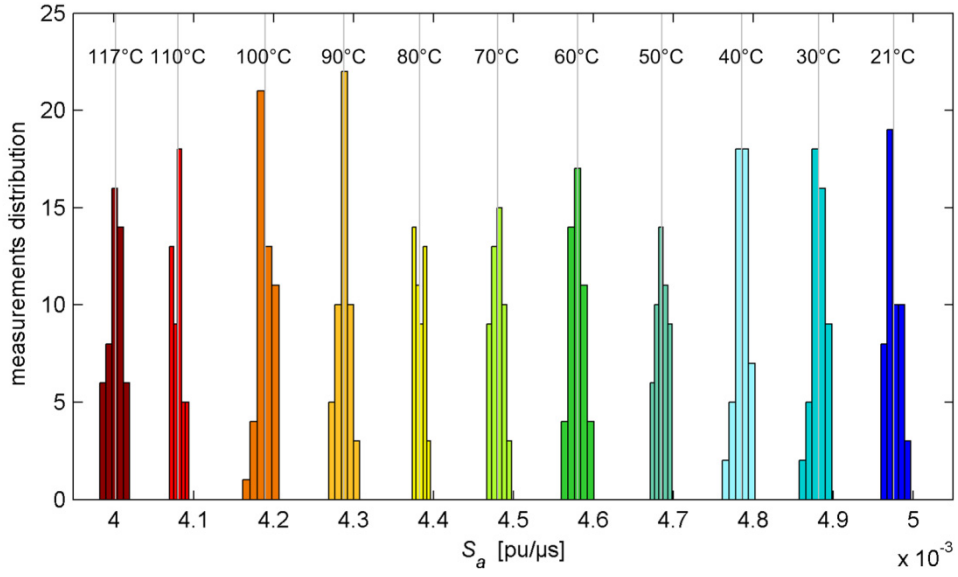

Figure 4-25: Distribution of the approximated d-current slopes S_a obtained from 50 measurements conducted at each reference magnet temperature T_m; setup 1: $t_{\mathrm{pw}} = 30\mu\mathrm{s}$ and $i_{d,ref} = 0.4\mathrm{pu}$; motor speed n=100rpm.

Setup 2: $t_{pw} = 50\mu s$ and $i_{d,ref} = 0.35\mathrm{pu}$

The setup is characterized by a voltage pulse duration that equals the PWM period in the applied control scheme. From a software point of view, this is the easiest way to generate a voltage pulse for the proposed magnet temperature estimation procedure and therefore it is of interest to be investigated. With respect to the selected reference d-current $i_{d,ref}$, again the setup is characterized by the highest method's sensitivity.

Table 4-7: Setup 2 ($t_{pw} = 50\mu\mathrm{s}$, $i_{d,ref} = 0.35\mathrm{pu}$): Reference magnet temperatures.

motor speed [rpm]	T_{m1} [°C]	T_{m2} [°C]	T_{m3} [°C]	T_{m4} [°C]	T_{m5} [°C]	T_{m6} [°C]	T_{m7} [°C]	T_{m8} [°C]	T_{m9} [°C]	T_{m10} [°C]	T_{m11} [°C]
n=100	21	30	40	50	60	70	80	90	100	108	-
n=4800	-	30	40	50	60	70	80	90	100	110	118

The reference magnet temperatures at which the measurements are carried out for this setup are given in Table 4-7. For motor speed n=100rpm, the d-current responses at each investigated reference magnet temperature T_m are plotted in Figure 4-26a and their linearised counterparts are given in Figure 4-26b. The d-current response at reference magnet temperature $T_m = 60°C$ is depicted in Figure 4-27 for motor speed n=100rpm and n=4800rpm.

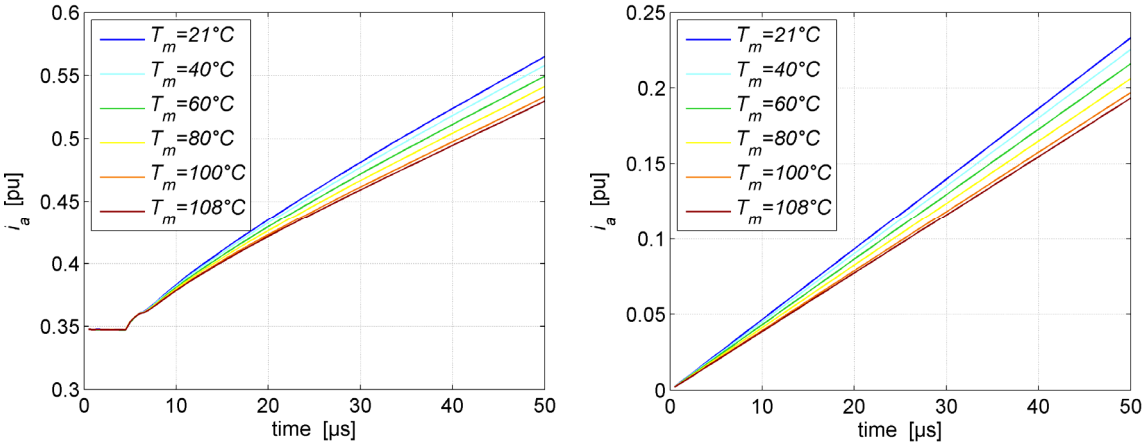

Figure 4-26: The d-current i_d response upon positive voltage pulse in the d-axis of the motor; $t_{pw} = 50\mu s$ and $i_{d,ref} = 0.35pu$; $V_{dc} = 750V$; (a) measured current response at various magnet temperatures and motor speed n=100rpm; sample rate 500ns; (b) linearisation of the measured current response by polynomial interpolation with eliminated offset.

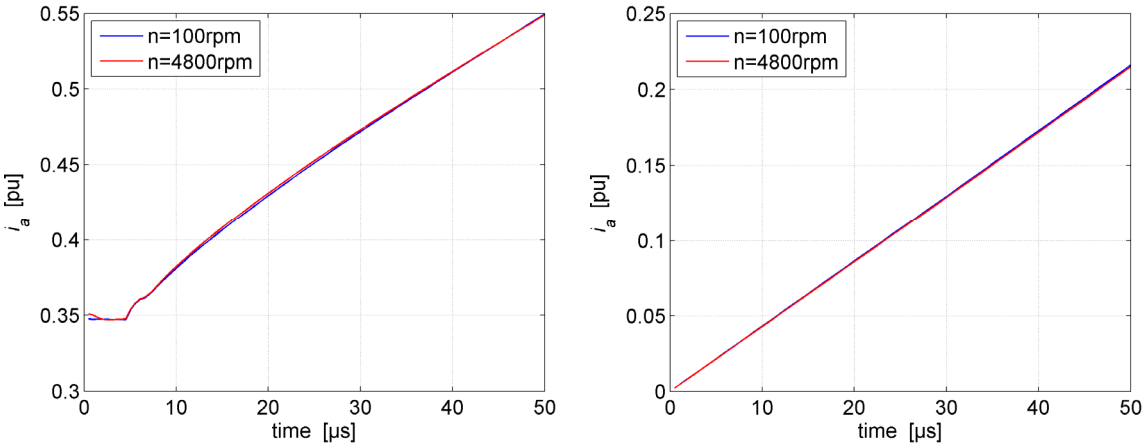

Figure 4-27: The d-current i_d response upon positive voltage pulse in the d-axis of the motor; $t_{pw} = 50\mu s$ and $i_{d,ref} = 0.35pu$; magnet temperature $T_m = 60°C$; $V_{dc} = 750V$; (a) measured current response at motor speed n=100rpm and n=4800rpm; sample rate 500ns; (b) linearisation of the measured current response by polynomial interpolation with eliminated offset.

Analogically to setup 1, a set of 50 measurements are carried out at each reference magnet temperature listed in Table 4-7, and motor speed n=100rpm and n=4800rpm. Thus, the dependency of the approximated d-current slopes S_a from the magnet temperature is visualized in Figure 4-28, where the mean values of S_a obtained from each set of 50 measurements for a given reference T_m are plotted as a function of the magnet temperature for motor speed n=100rpm and n=4800rpm.

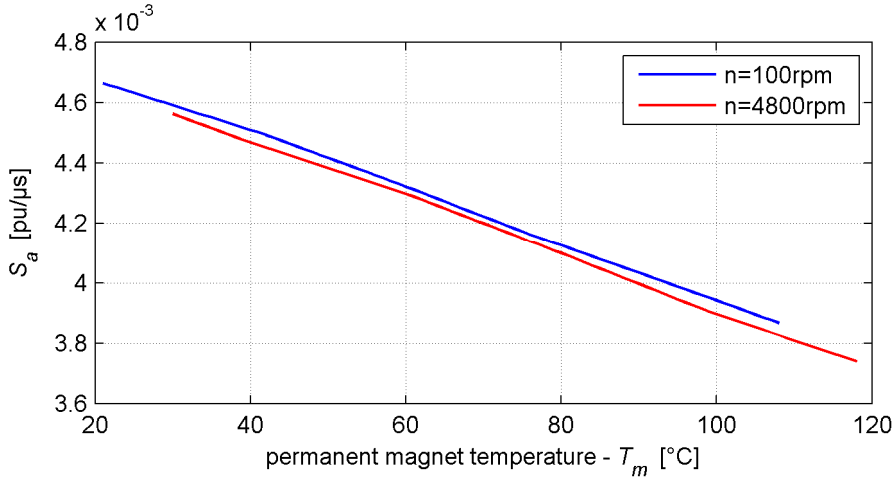

Figure 4-28: Approximated d-current slopes S_a as a function of magnet temperature for motor speed n=100rpm and n=4800rpm; setup 2: $t_{pw} = 50\mu s$ and $i_{d,ref} = 0.35pu$.

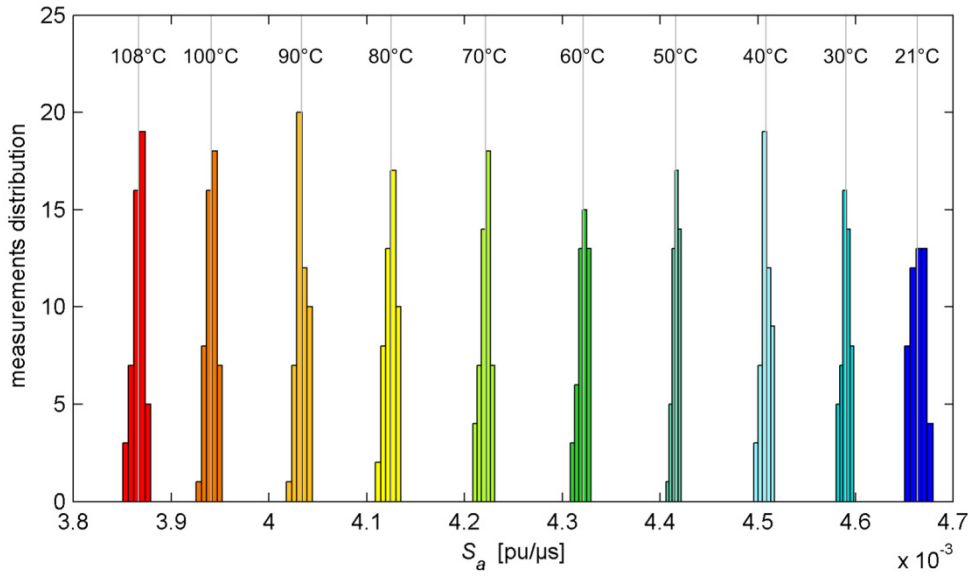

Figure 4-29: Distribution of the approximated d-current slopes S_a obtained from 50 measurements conducted at each reference magnet temperature T_m; setup 2: $t_{pw} = 50\mu s$ and $i_{d,ref} = 0.35pu$; motor speed n=100rpm.

The distribution of the approximated d-current slopes S_a obtained from the 50 measurements conducted at each reference magnet temperature T_m and motor speed n=100rpm are given as histogram plot in Figure 4-29. The grey line drawn through a distribution indicates the mean value of S_a for a given reference magnet temperature.

Setup 3: $t_{pw} = 90\mu s$ and $i_{d,ref} = 0.30pu$

The setup is characterized by a relative large voltage pulse and highest method's sensitivity with respect to the selected reference d-current $i_{d,ref}$. The reference magnet temperatures at which the measurements are carried out for this setup are given in Table 4-8. For motor speed n=100rpm, the d-current responses at each investigated reference magnet temperature T_m are plotted in Figure 4-30a, while their linearised counterparts are given in Figure 4-30b.

Table 4-8: Setup 3 ($t_{pw} = 90\mu s$, $i_{d,ref} = 0.3pu$): Reference magnet temperatures.

motor speed [rpm]	T_{m1} [°C]	T_{m2} [°C]	T_{m3} [°C]	T_{m4} [°C]	T_{m5} [°C]	T_{m6} [°C]	T_{m7} [°C]	T_{m8} [°C]	T_{m9} [°C]	T_{m10} [°C]	T_{m11} [°C]
n=100	-	32	40	50	60	70	80	90	100	110	119
n=4800	21	30	40	50	60	70	80	90	100	110	118

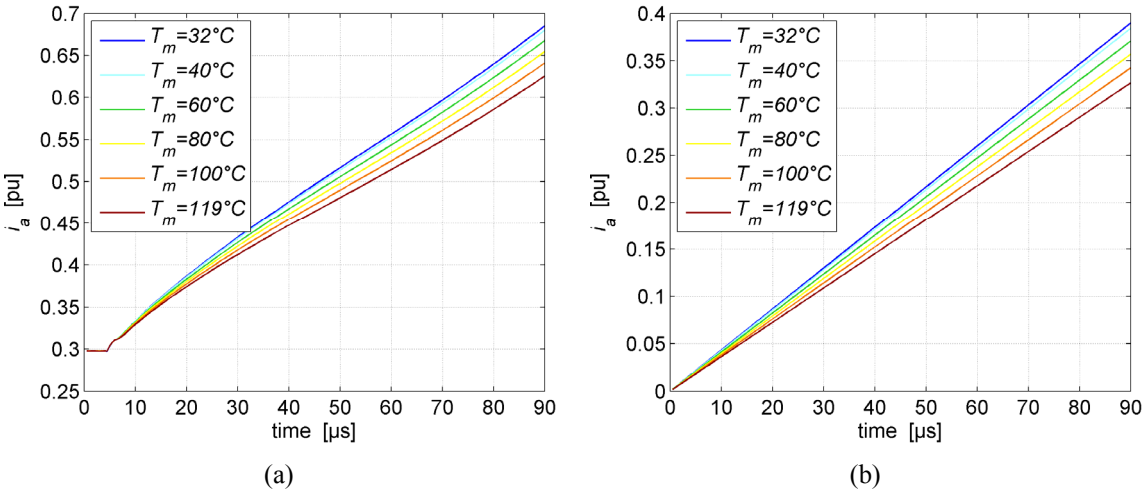

Figure 4-30: The d-current i_d response upon positive voltage pulse in the d-axis of the motor; $t_{pw} = 90\mu s$ and $i_{d,ref} = 0.3pu$; $V_{dc} = 750V$; (a) measured current response at various magnet temperatures and motor speed n=100rpm; sample rate 500ns; (b) linearisation of the measured current response by polynomial interpolation with eliminated offset.

The d-current response at reference magnet temperature $T_m = 60°C$ is depicted as measured in Figure 4-31a and in linearised form in Figure 4-31b for motor speed n=100rpm and n=4800rpm. Analogically to setup 1 and setup 2, a set of 50 measurements are carried out at each reference magnet temperature, and motor speed n=100rpm and n=4800rpm. The approximated d-current slopes S_a as a function of the magnet temperature for motor speed n=100rpm and n=4800rpm are given in Figure 4-32.

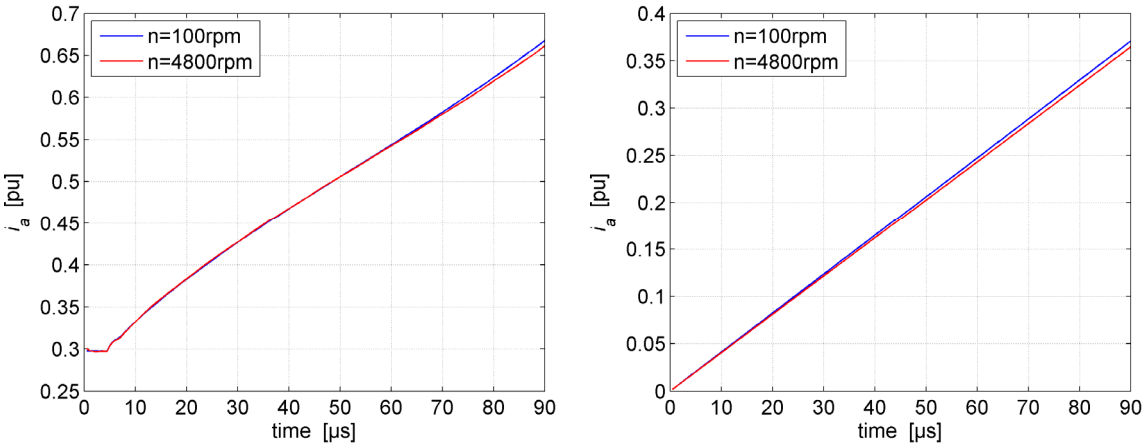

Figure 4-31: The d-current i_d response upon positive voltage pulse in the d-axis of the motor; $t_{pw} = 90\mu s$ and $i_{d,ref} = 0.3pu$; magnet temperature $T_m = 60°C$; $V_{dc} = 750V$; (a) measured current response at motor speed n=100rpm and n=4800rpm; sample rate 500ns; (b) linearisation of the measured current response by polynomial interpolation with eliminated offset.

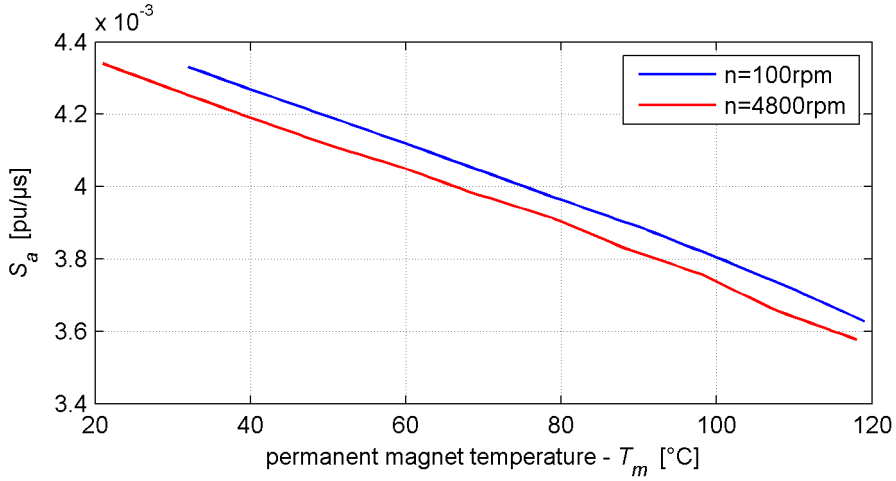

Figure 4-32: Approximated d-current slopes S_a as a function of magnet temperature for motor speed n=100rpm and n=4800rpm; setup 3: $t_{pw} = 90\mu s$ and $i_{d,ref} = 0.3pu$.

The distribution of the approximated d-current slopes S_a obtained from the 50 measurements conducted at each reference magnet temperature T_m and motor speed n=100rpm is depicted as histogram plot in Figure 4-33. The grey line drawn through a distribution indicates the mean value of S_a for a given reference magnet temperature.

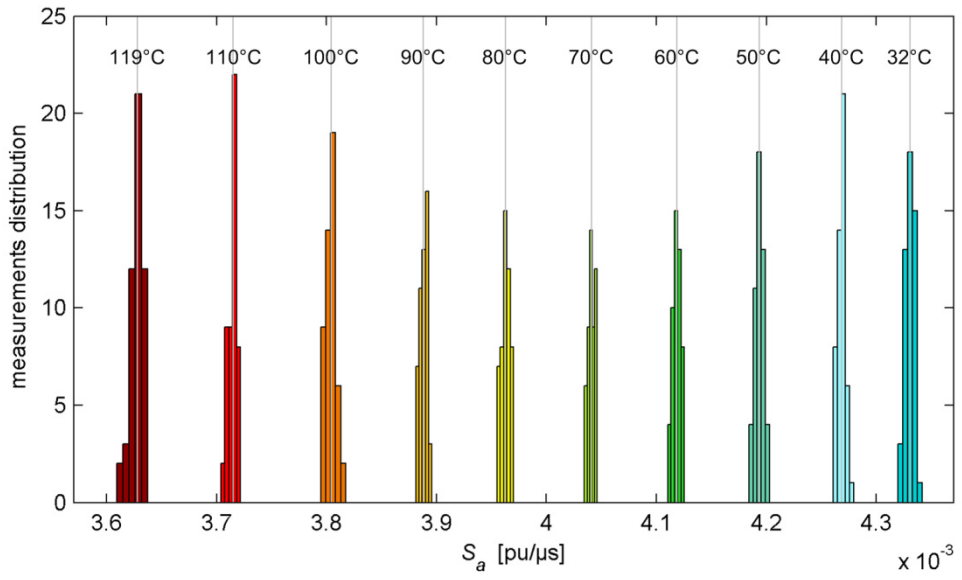

Figure 4-33: Distribution of the approximated d-current slopes S_a obtained from 50 measurements conducted at each reference magnet temperature T_m; setup 3: $t_{pw} = 90$µs and $i_{d,ref} = 0.3$pu; motor speed n=100rpm.

4.3.5 Discussions

With respect to the discussions made in section 4.3.3, the mean standard deviations of S_a and $\Delta i_a/\Delta t$ for a normal distribution calculated for each investigated setup with respect to the voltage pulse width t_{pw} are given in Table 4-9. By comparing the values of $\sigma(S_a)$ and $\sigma(\Delta i_a/\Delta t)$ within a setup, it is evident that a magnet temperature estimation procedure considering S_a as a temperature indicator is characterized by higher sensitivity than $\Delta i_a/\Delta t$. However, from software point of view, calculating the difference quotient $\Delta i_a/\Delta t$ is much easier to implement, whereby a low-cost microcontroller can be used. In contrast, an accurate online current slope linearisation S_a requires a motor control unit with current oversampling capability and higher computing power.

Comparing the three investigated setups the standard deviation of the linearised current slopes $\sigma(S_a)$ decreases when the voltage pulse becomes longer, see Table 4-9. Graphically this can be observed by comparing Figure 4-25, Figure 4-29 and Figure 4-33, where the distribution of the measurements for a reference temperature becomes narrower while t_{pw} increases. This is because the effect of varying saturation level in the d-axis of the motor due to varying magnet temperature is more distinctively reflected in a larger d-current response which requires an application of a longer voltage pulse. Therefore, considering a single measurement the probability to capture the correct magnet temperature is higher with a longer voltage pulse than with a shorter one. This means that with a longer voltage pulse the accuracy of the method will increase whereby the mean value over a few measurements will be sufficient to capture relatively precise the magnet temperature of the machine.

Table 4-9: Mean standard deviation σ for the approximated current slopes S_a versus pulse width t_{pw}.

standard deviation	$t_{pw} = 30\mu s$ setup 1	$t_{pw} = 50\mu s$ setup 2	$t_{pw} = 90\mu s$ setup 3
$\sigma(S_a)$	$1.028e-05$	$7.687e-06$	$4.129e-06$
$\sigma(\Delta i_a/\Delta t)$	$3.217e-05$	$1.023e-05$	$1.047e-05$

However, this is will be only valid for low speed or a narrow speed range. In a wider speed range, there is an offset between the linearised d-current slopes S_a. This can be

observed in Figure 4-24, Figure 4-28 and Figure 4-32, where S_a is plotted at low and high speed, n=100rpm and n=4800rpm, as a function of the magnet temperature. Therefore, if a LUT, that establishes a relationship between S_a and T_m, is obtained at low speed, the offset will lead to an error in the estimation of the magnet temperature at higher speeds. For setup 1, 2 and 3 this error is depicted in Figure 4-34.

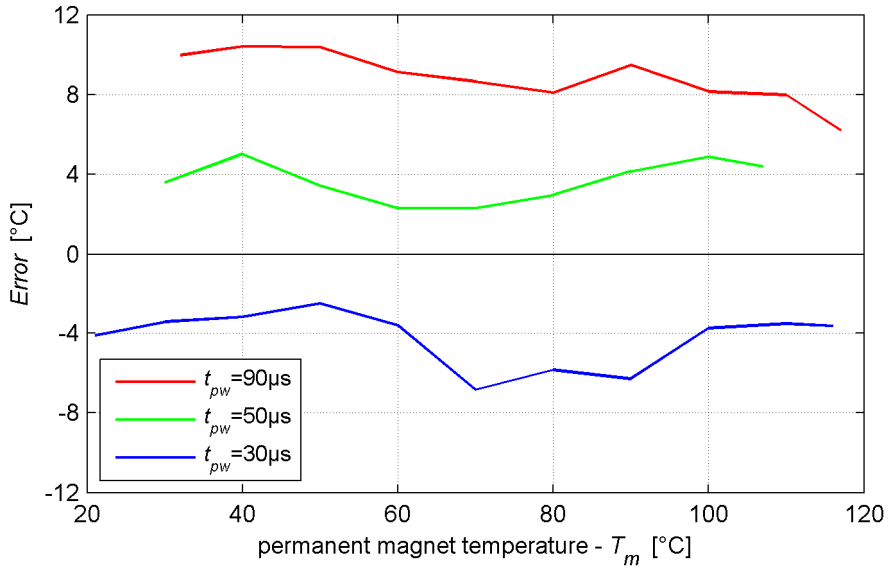

Figure 4-34: Magnet temperature estimation error between n=100rpm and n=4800rpm for setup 1 ($t_{pw} = 30\mu s$ and $i_{d,ref} = 0.4$pu), for setup 2 ($t_{pw} = 50\mu s$ and $i_{d,ref} = 0.35$pu) and setup 3 ($t_{pw} = 90\mu s$ and $i_{d,ref} = 0.3$pu);

There are three major effects that are responsible for the speed dependency in the d-current slope di_d/dt:

- The d-current i_d produces a flux in the q-axis of the machine (cross-coupling effects) that induces itself a speed dependent voltage in the d-axis of the machine.

- The q-current i_q that develops along the voltage pulse at higher speed induces additional voltages in the d-axis of the machine.

- At the beginning of the voltage pulse, the deviation between the d-axis and the α-axis of the machine increases while the speed increases.

It is very difficult indeed to separate these effects. In setup 3 with $t_{pw} = 90\mu s$, at motor speed n=4800rpm the angles θ_0 and θ_1 between the d-axis and the α-axis at the time

instant of the beginning and the end of the voltage pulse equal 5.2° according to (4-9). For the time duration of the voltage pulse, this deviation is responsible for an inherently lower average saturation level in the stator α-axis at higher speed, which leads to a smaller d-current slope di_d/dt than one obtained at lower speed. The effect due to the deviation between the d-axis and the α-axis can be considered negligible when θ_0 and θ_1 are also relatively small at higher speeds. Thus, along a voltage pulse in the d-axis of the motor, the contribution of the magnet flux density to the overall saturation level of the steel stator core in the α-axis of the machine can be assumed at high speed the same as at low speed. Therefore, in the experimental setups presented further in section 4.4 and 4.5 a preference is given to setups implying a short voltage pulse, $t_{pw} = 30\mu s$, whereby θ_0 and θ_1 equal 1.7° at speed n=4800rpm (the maximum investigated motor speed). This is because with a short voltage pulse, the source of offset in the d-current slope di_d/dt at higher speeds is predominantly caused by speed dependent voltage terms induced in the d-axis of the motor. These voltage terms can be analytically compensated, as will be discussed in the next section. In contrast, lower average saturation level due to large deviation between the d-axis and the α-axis of the motor at higher speed can be compensated only by identification of a LUT for various reference speeds.

For a given application, it depends on the machine operating speed range and the motor inductance in the d-axis how big the voltage pulse width t_{pw} should be selected. This should be carefully set for a given machine considering all discussions made so far. Once a voltage pulse width t_{pw} is defined, the initial d-current $i_{d,ref}$ can be estimated for best possible sensitivity with respect to the magnet temperature T_m by plotting the difference $\Delta S_a = S_{a(T_{m1})} - S_{a(T_{m2})}$ as a function of $i_{d,ref}$, whereby S_a is measured at two different magnet temperatures (T_{m1} and T_{m2}). For best results, the magnet temperature T_{m1} and T_{m2} should be selected symmetrical with respect to the middle of the entire expected operating magnet temperature range. Assuming an operating magnet temperature range between 20°C and 120°C, an estimation of an initial d-current $i_{d,ref}$ characterized with best possible sensitivity with respect to T_m should be carried out between reference magnet temperature $T_{m1} = 60°C$ and $T_{m2} = 80°C$ for example. As alternative, for convenience T_{m1} can be chose to be the room temperature as in Figure 4-21 while $T_{m2} = 60$°C.

4.4 Sensorless Magnet Temperature Estimation with a Positive and a Negative Voltage pulse in the D-axis of the Motor at Zero Load – Speed Compensation

As demonstrated in the experimental results in section 4.3, an estimation of the magnet temperature of the IPMSM under test based on a single positive voltage pulse reveals a clear speed dependency. There is an inherent offset in the d-current slopes between low and high speeds which will lead to erroneous magnet temperature estimation. Although the error can be considered to a great extent proportional to the speed, it can be compensated by establishing two LUTs between reference magnet temperatures and the corresponding d-current slope: one at standstill and another one at nominal speed or at maximum operating speed. In many cases identifying the LUT for a given motor at high speeds is cumbersome or in the worst case it cannot be realized at all. For example, if an identification of a LUT is carried out in an environmental chamber, operating the machine at high speeds can be undesirable.

In the current section an approach, first reported in [80] and [81], is proposed where the identification of a LUT at nominal speed is made obsolete by compensating the speed dependency analytically. For the purpose, the motor equations are analyzed first to identify speed dependent terms that influence the d-current response upon a voltage pulse in the d-axis of the motor. A compensation technique by applying an additional pulse in the negative d-axis is proposed, which increases the robustness of the magnet temperature estimation by reducing the speed influence in the d-current response. For better explanation of the presented compensation approach a notation as listed in Table 4-10 is adopted here.

Table 4-10: Adopted notation.

i_{dP}	d-current response upon a voltage pulse in the positive d-axis
i_{dN}	d-current response upon a voltage pulse in the negative d-axis
L^*_{ddP}	d-axis differential inductance along a voltage pulse in the positive d-axis
L^*_{ddN}	d-axis differential inductance along a voltage pulse in the negative d-axis
p_0	beginning of a pulse switching command (the beginning of an idle voltage pulse)
p_1	end of a pulse switching command (the end of an idle voltage pulse)
t_0	beginning of a measured effective current curve
t_1	end of a measured effective current curve

4.4.1 Motor Equations upon a Positive Voltage Pulse in the D-axis of the Motor

In the following, the motor voltage equations are analyzed in order to identify the voltage terms of the machine that disturb the d-current response upon a positive voltage pulse in the d-axis. For the purpose, the motor equations (3-27) and (3-28) derived in section 3.3.4 that consider saliencies, saturation and cross-coupling saturation effects are used in the current analysis. For convenience, the motor equations (3-27) and (3-28) are given here again:

$$u_d = R_s i_d + L^*_{dd}\frac{di_d}{dt} + L^*_{dq}\frac{di_q}{dt} - \omega L_{qq} i_q - \omega L_{qd} i_d \tag{4-19}$$

$$u_q = R_s i_q + L^*_{qq}\frac{di_q}{dt} + L^*_{qd}\frac{di_d}{dt} + \omega L_{dd} i_d + \omega L_{dq} i_q + \omega \psi_M. \tag{4-20}$$

When a voltage pulse is applied in the positive d-axis of the motor and the rotor and stator reference frames are aligned ($\theta = 0$), the effective voltage space vector applied to the motor terminals has the components $u_d = 2/3 V_{dc}$ and $u_q = 0$. Thus, the motor equations (4-19) and (4-20) become:

$$\frac{2}{3}V_{dc} = R_s i_d + L^*_{dd}\frac{di_d}{dt} + L^*_{dq}\frac{di_q}{dt} - \omega L_{qq} i_q - \omega L_{qd} i_d \tag{4-21}$$

$$0 = R_s i_q + L^*_{qq}\frac{di_q}{dt} + L^*_{qd}\frac{di_d}{dt} + \omega L_{dd} i_d + \omega L_{dq} i_q + \omega \psi_M. \tag{4-22}$$

According to (4-21) and (4-22) in a rotating machine the sum of the voltage terms that produce the d-current and q-current response upon a positive d-axis voltage pulse with negligible short time duration can be summarized as follows:

$$L^*_{dd}\frac{di_d}{dt} = \frac{2}{3}V_{dc} - R_s i_d \overbrace{-L^*_{dq}\frac{di_q}{dt}}^{Term\ 1} + \overbrace{\omega L_{qq} i_q}^{Term\ 2} + \overbrace{\omega L_{qd} i_d}^{Term\ 3} \tag{4-23}$$

$$L^*_{qq}\frac{di_q}{dt} = -R_s i_q - L^*_{qd}\frac{di_d}{dt} - \omega L_{dd} i_d - \omega L_{dq} i_q - \omega \psi_M. \tag{4-24}$$

As it was demonstrated already, the slope of the d-current response di_d/dt upon a voltage pulse in the d-axis of the motor is strongly dependent of the magnet temperature T_m over the saturation level of the d-axis of the steel stator core. However, according to (4-23) di_d/dt is also influenced directly by the voltage term $Term\ 1$ and the speed

dependent voltage terms $Term\ 2$ and $Term\ 3$. The voltage drop of the stator winding resistance is neglected here again. Although, it is subject to the condition that at the beginning of the voltage pulse the q-current is zero, $i_q = 0$, which means that at the beginning of the voltage pulse $Term\ 1$ and $Term\ 2$ will be zero too, at higher speeds according to (4-24) the q-current will change along the voltage pulse. This change is produced predominantly due to the induced inner voltage of the permanent magnet flux linkage ($-\omega\psi_M$). Consequently $Term\ 1$ and $Term\ 2$ will also change along the voltage pulse affecting the effective voltage $L_{dd}^{*} di_d/dt$, which in turn will affect the slope of the d-current response di_d/dt upon magnet temperature estimation procedure.

According to (4-24), along a voltage pulse in the d-axis of the motor the change of the q-current will occur in the negative direction, $i_q < 0$. Consequently $Term\ 1$ in (4-23) will increase the effective voltage $L_{dd}^{*} di_d/dt$ along the voltage pulse. Analogically, $Term\ 2$ in (4-23) will become negative, decreasing the effective voltage $L_{dd}^{*} di_d/dt$ along the voltage pulse. Finally, considering setup 1/2/3, discussed in section 4.3.4, where the initial d-current $i_{d,ref} \geq 0.3pu$, $Term\ 3$ will also lead to an increase of $L_{dd}^{*} di_d/dt$.

4.4.2 Speed Compensation Approach

In a magnet temperature estimation procedure based on a single positive voltage pulse in the d-axis, $Term\ 1$, $Term\ 2$ and $Term\ 3$ in (4-23) are seen as disturbing factors, since they introduce a speed dependent error in the estimation of the magnet temperature. By considering a combination of a positive and a negative voltage pulse in the d-axis of the motor, symmetry in (4-23) can be achieved which eliminates to a great extent the undesired terms. Thus, the difference of the effective voltages resulting from a pulse generation in the positive and negative motor d-axis $L_{ddP}^{*} di_{dP}/dt - L_{ddN}^{*} di_{dN}/dt$ will be less affected by the motor speed, whereby the difference of the resulting slopes of the d-current responses $di_{dP}/dt - di_{dN}/dt$ becomes an indicator for the magnet temperature T_m.

The main symmetry investigated here is based on the q-current. Thus, it is set here as a condition that the q-current should have the same values along the positive and the negative voltage pulse.

$$i_{qP} = i_{qN} \tag{4-25}$$

$$
\begin{aligned}
L^*_{ddP}\frac{di_{dP}}{dt} - L^*_{ddN}\frac{di_{dN}}{dt} \\
&= \frac{4}{3}V_{dc} - R_s(i_{dP} - i_{dN}) \\
&\quad \overbrace{- L^*_{dq}\left(\frac{di_{qP}}{dt} - \frac{di_{qN}}{dt}\right)}^{=0} + \overbrace{\omega L_{qq}(i_{qP} - i_{qN})}^{=0} \\
&\quad + \omega L_{qdP} i_{dP} - \omega L_{qdN} i_{dN}
\end{aligned}
\tag{4-26}
$$

The advantage of a symmetry according to (4-25) can be seen straightforward in the equation difference (4-26). It eliminates $Term\ 1$ and $Term\ 2$ in (4-23) whereby (4-26) is reduced to:

$$
\begin{aligned}
L^*_{ddP}\frac{di_{dP}}{dt} - L^*_{ddN}\frac{di_{dN}}{dt} \\
&= \frac{4}{3}V_{dc} - R_s(i_{dP} - i_{dN}) + \omega L_{qdP} i_{dP} - \omega L_{qdN} i_{dN}.
\end{aligned}
\tag{4-27}
$$

The preference here to eliminate $Term\ 1$ and $Term\ 2$ in (4-23) is motivated by the fact that these two terms influence $L^*_{dd} di_d/dt$ in two different directions. While $Term\ 1$ increases $L^*_{dd} di_d/dt$, $Term\ 2$ decreases $L^*_{dd} di_d/dt$ along the voltage pulse.

Furthermore, a symmetry with respect to the d-current responses i_{dP} and i_{dN} upon the positive and negative voltage pulse can eliminate or at least reduce significantly the influence of terms $R_s(i_{dP} - i_{dN})$ and $\omega L_{qdP} i_{dP} - \omega L_{qdN} i_{dN}$ in (4-27). Obviously, a full elimination will occur when

$$
i_{dP} = i_{dN}. \tag{4-28}
$$

However a current response symmetry that satisfies both (4-25) and (4-28) is in many cases very hard or almost impossible to obtain without controlling both the q-current and d-current reference values, $i_{q,ref}$ and $i_{d,ref}$. Such symmetry that satisfies (4-25) and (4-28) at the same time is demonstrated and discussed in section 4.5.

The proposed speed compensation is predominantly based on elimination of the q-current influence on the d-current response in (4-27) by controlling solely the d-current initial value upon the negative voltage pulse $i_{dN,ref}$ in a way that the q-current

developed along the negative voltage pulse i_{qN} equals the q-current developed along the positive voltage pulse i_{qP}, ($i_{qP} = i_{qN}$).

4.4.3 Experimental Validation

The analytical analysis made in 4.4.1 and 4.4.2 are valid under the assumption that the d-axis angular displacement within the voltage pulse duration according to (4-9) can be neglected. In other words, the saturation level reflected in the d-current response will be the same at low and high speed for the same magnet temperature. Therefore, for the validation of the speed compensation a short voltage pulse of $30\mu s$ is considered. It should be noted here that with respect to the switching command the duration of the positive and negative voltage pulse is the same, $t_{pwP} = t_{pwN} = 30\mu s$.

The initial d-current of the positive voltage pulse is kept constant $i_{dP,ref} = 0.4pu$, which implies maximum possible sensitivity of the d-current response with respect to the magnet temperature T_m, as in setup 1 investigated in section 4.3.4. In contrast, the d-current initial value upon negative voltage pulse $i_{dN,ref}$ can be arbitrarily set. Thus, $i_{dN,ref}$ is controlled in a manner that the current space vector response upon a positive voltage pulse $\underline{i}_P$ has the same value at the end of the pulse as the current space vector response upon a negative voltage pulse $\underline{i}_N$:

$$\underline{i}_{P(p_1)} = \underline{i}_{N(p_1)}. \tag{4-29}$$

This is the criteria according to which $i_{dN,ref}$ is controlled here for any speed. As a consequence of this criteria, the symmetry of the q-current can be achieved, ($i_{qP} = i_{qN}$) and the d-current responses of the positive and negative voltage pulse are also equal at the end of the pulse duration, $i_{dP(p_1)} = i_{dN(p_1)}$. Figure 4-35a demonstrates the completion of the criteria (4-29) in a real measurement carried out at motor speed n=100rpm and n=4800rpm for the same magnet temperature ($T_m = 60°C$), where the end values of the effective space vector current response are almost equal, $\underline{i}_{P(t_1)} \approx \underline{i}_{N(t_1)}$. The plots of the corresponding q-current responses are separately depicted in Figure 4-35b, showing more clearly the compensating approach, where the q-current curves upon positive and negative voltage pulse are almost equal, $i_{qP} \approx i_{qN}$. The corresponding d-current responses are plotted in Figure 4-35c. As it can be observed the end values of the effective d-current response curves are almost equal $i_{dP(t_1)} \approx i_{dN(t_1)}$. Therefore the absolute difference of the d-current responses $i_{dP} - i_{dN}$

decreases towards zero along the voltage pulse reducing additionally terms $R_s(i_{dP} - i_{dN})$ and $\omega L_{qdP} i_{dP} - \omega L_{qdN} i_{dN}$ in (4-27). Thus, the difference of the d-current responses $i_{dP} - i_{dN}$ becomes predominantly dependent of the actual magnet temperature. Under elimination of the inverter dead time, Figure 4-35d shows the current curves plotted from the difference between the current samples that construct the corresponding effective d-current curves i_{dP} and i_{dN}, for n=100rpm and n=4800rpm.

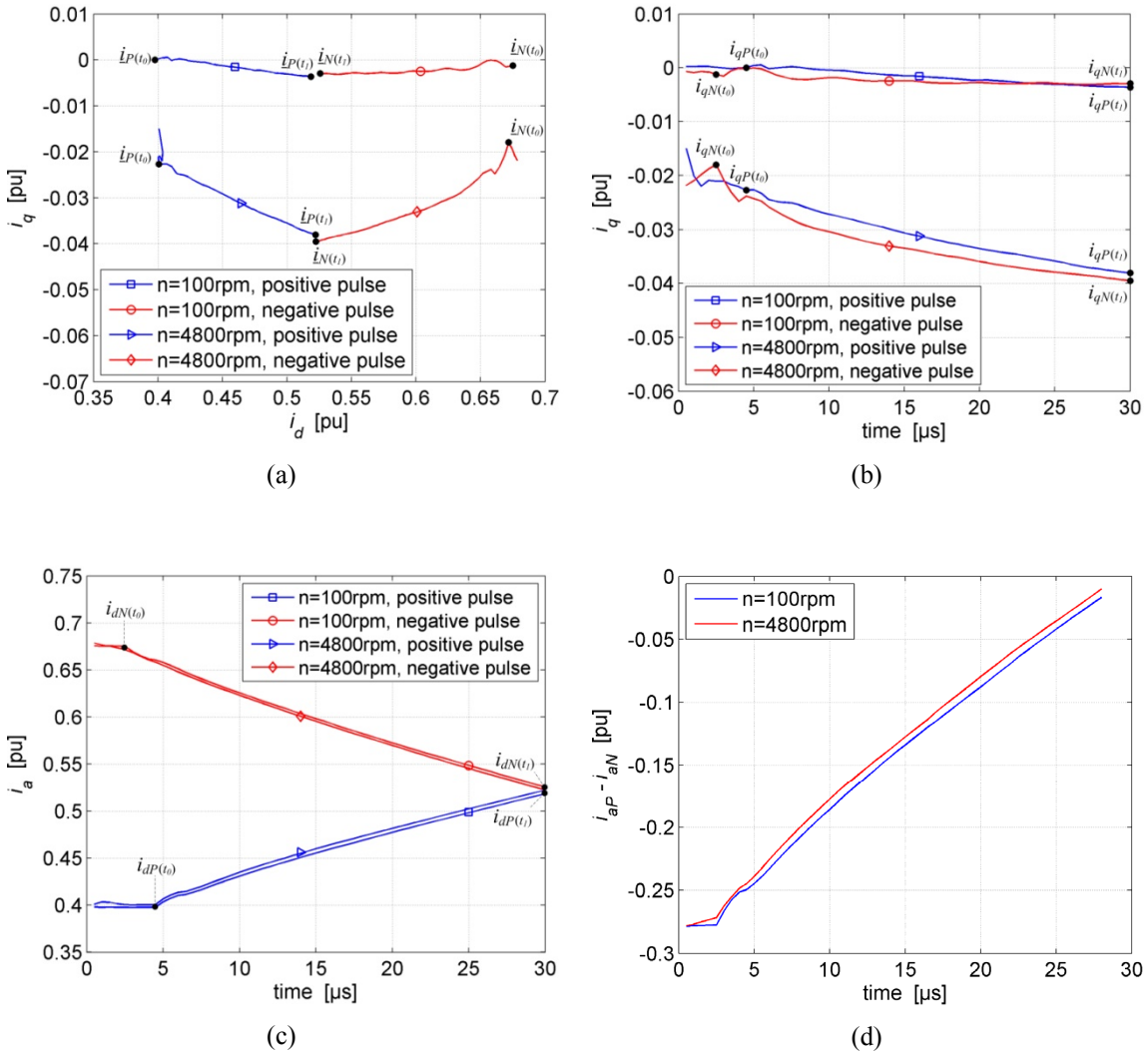

Figure 4-35: Current response upon a positive and negative voltage pulse in the d-axis of the motor at motor speed n=100rpm and n=4800rpm; constant magnet temperature $T_m = 60°C$; $t_{pw} = 30\mu s$ and $i_{d,refP} = 0.4pu$; sample rate 500ns; $V_{dc} = 750V$; (a) current space vector response; (b) q-current response; (c) d-current response; (d) the difference $i_{dP} - i_{dN}$ between the effective d-current response curves.

In contrast to the d-current response upon positive voltage pulse i_{dP}, the d-current response upon negative voltage pulse i_{dN} is not affected by the inverter dead time t_{TD}, see Figure 4-35c. Owing to the direction of the machine currents and the pulse polarity, the beginning of the positive effective voltage pulse in the machine is delayed by t_{TD} compared to the beginning of the negative effective voltage pulse. This has been explained already in section 4.1.3. For this reason, the evaluation of the difference of the d-current responses is carried out here upon the difference between the linearised d-current slope S_{aP} of the positive voltage pulse and the linearised d-current slope S_{aN} of the negative voltage pulse:

$$S_{aPN} = S_{aP} - S_{aN}. \tag{4-30}$$

In order to validate the proposed speed compensation procedure for a wider temperature range, measurements are conducted at equidistant reference magnet temperatures from 20°C to 120°C with step of 10°C. The difference of the positive and the negative voltage current response $i_{dP} - i_{dN}$ for various reference magnet temperatures at speed n=100rpm is depicted in linearised form in Figure 4-36.

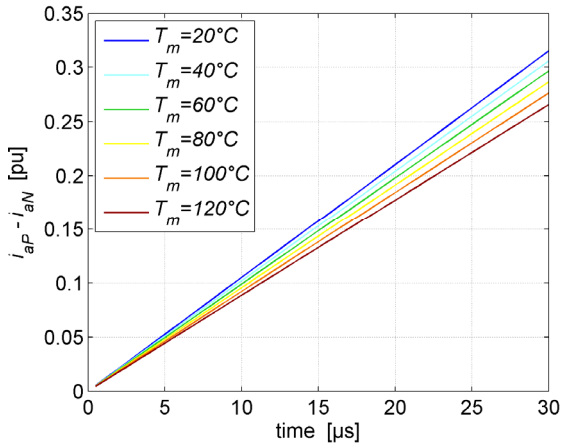

Figure 4-36: Linearised difference of the d-current response $i_{dP} - i_{dN}$ upon a positive and negative voltage pulse with eliminated offset at various reference magnet temperatures and constant motor speed n=100rpm; $t_{\mathrm{pw}} = 30\mu s$ and $i_{dP,ref} = 0.4\mathrm{pu}$; sample rate 500ns; $V_{\mathrm{dc}} = 750\mathrm{V}$.

For each reference magnet temperature 25 measurements are carried out. A single measurement consists of a generation of a positive voltage pulse followed by a generation of a negative voltage pulse in order to obtain S_{aP} and S_{aN} respectively. The time interval between a positive and negative voltage pulse generation is set to 100ms. The completion of all 25 test measurements of S_{aPN} at a given reference magnet temperature takes between 5 and 10 seconds. Within this time, the temperature of the

magnets does not change significantly and can be assumed constant. The obtained calculated linearised current slope differences S_{aPN} are depicted in Figure 4-37 as a function of the magnet temperature for n=100rpm and n=4800rpm. A value of S_{aPN} for a given reference temperature is the mean value over 25 measurements. The distribution of the 25 measurements of S_{aPN} at each reference temperature is given in Figure 4-38 for n=100rpm. The grey line through each distribution represents the corresponding mean value of S_{aPN}.

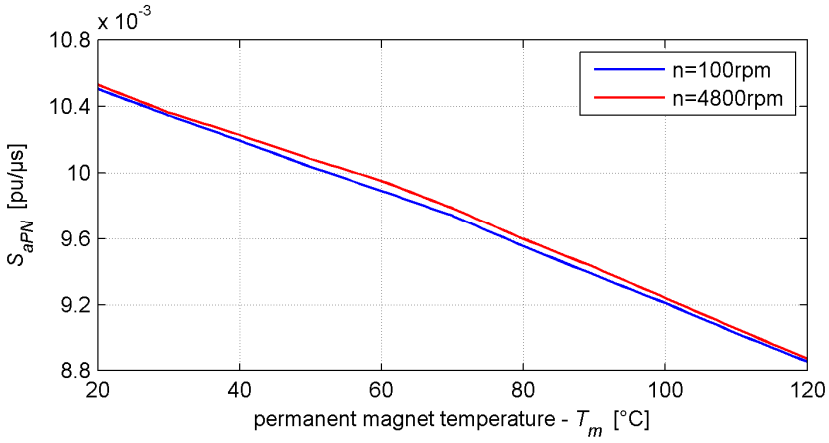

Figure 4-37: Linearised current slope differences S_{aPN} as a function of the magnet temperature T_m; compensated setup implying a positive and a negative voltage pulse in the d-axis of the motor for motor speed n=100rpm and n=4800rpm; $t_{pw} = 30\mu s$ and $i_{dP,ref} = 0.4$pu; sample rate 500ns; $V_{dc} = 750$V.

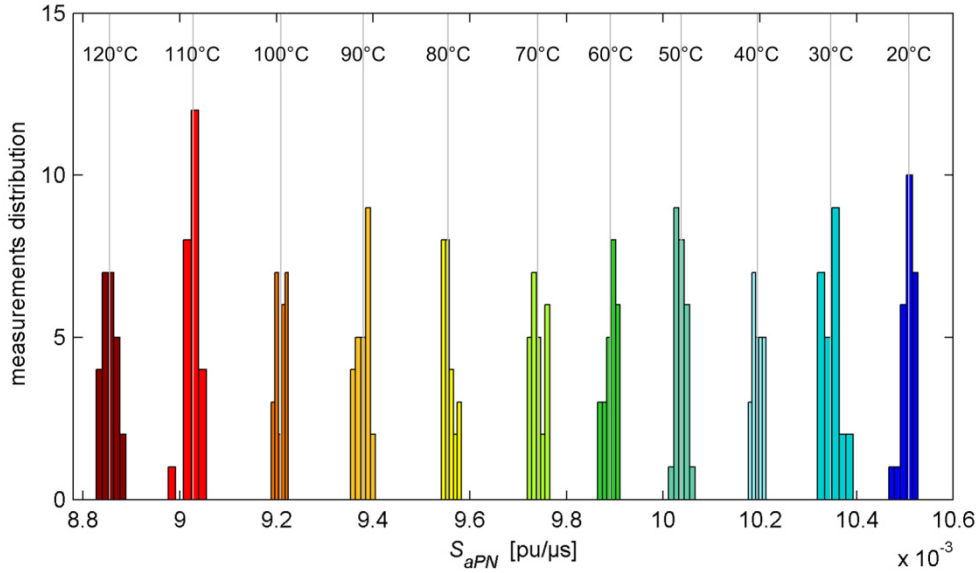

Figure 4-38: Distribution of the 25 measurements for each reference magnet temperature for S_{aPN} at motor speed n=100rpm; compensated setup with $t_{pw} = 30\mu s$ and positive voltage pulse initial d-current $i_{dP,ref} = 0.4$pu; $V_{dc} = 750$V.

As it can be observed in Figure 4-37, there is still an offset between the slopes S_{aPN} measured at n=100rpm and n=4800rpm, however the results are much more robust compared to a setup 1 from section 4.3.4., which is the reference setup in this investigation. The error between the current slope differences S_{aPN} obtained for n=100 and n=4800 expressed in degree Celsius is given in Figure 4-39. This is comparatively plotted together with the error curve obtained from setup 1 in section 4.3.4 depicted in Figure 4-34.

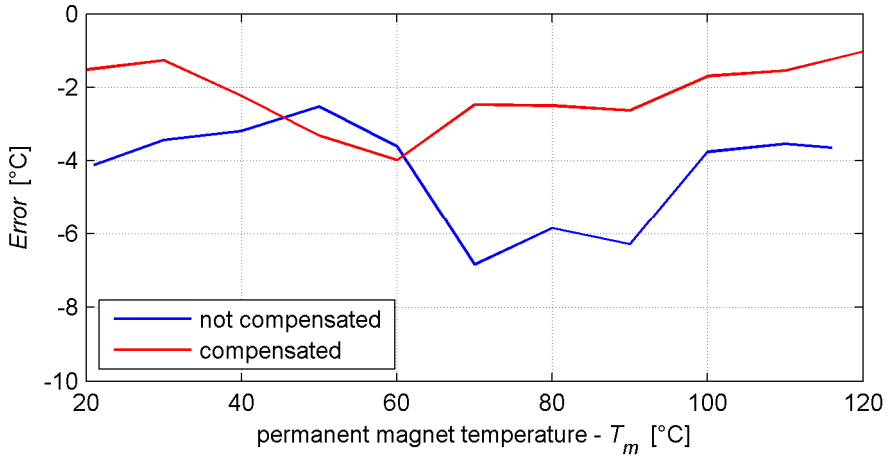

Figure 4-39: Magnet temperature estimation error between n=100rpm and n=4800rpm; comparative plots; an error curve for not compensated setup implying a single positive voltage pulse (setup 1: $t_{pw} = 30\mu s$ and $i_{d,ref} = 0.4pu$); an error curve for compensated setup with $t_{pw} = 30\mu s$ and positive voltage pulse initial d-current $i_{dP,ref} = 0.4pu$, and variable negative voltage pulse initial d-current, $i_{dN,ref}$.

Table 4-11: Error between low and high speed for not compensated and compensated setup.

Error [°C]	Not compensated setup (setup 1, implying a single positive voltage pulse)	Compensated setup (a setup implying a positive and negative voltage pulse)
Mean	-4°C	-2°C
Minimum	-2.5°C	-1°C
Maximum	-6.8°C	-3.8°C

Table 4-11 summarizes quantitatively the minimum and maximum error, and the resulting mean error for both, compensated and not compensated setup. Regarding the d-current response sensitivity with respect to the magnet temperature T_m, the demonstrated setup is not optimal as it implies only maximum sensitivity for S_{aP} but

not maximum sensitivity for S_{aN}. This is because, for comparison, the same initial d-current for the positive voltage pulse has been used, as estimated for setup 1 ($t_{pw} = 30\mu s$ and $i_{d,ref} = 0.4pu$) from section 4.3.4. However, the overall maximum sensitivity can be estimated by estimating the maximum deviation of S_{aPN} at two different reference temperatures as a function of $i_{dP,ref}$, analogically to the sensitivity investigation demonstrated in Figure 4-21 for the IPMSM under test.

4.4.4 Discussions

Magnet temperature estimation procedure based on negative and positive voltage pulse is clearly characterized by a better robustness and accuracy compared to a single positive voltage pulse approach, see Table 4-11. However, it is opinion of the author that the presented compensation approach can be further improved if the following aspects are considered:

- The time duration of the negative voltage pulse t_{pwN} can be made variable so that the positive and negative voltage pulse widths are not obligatory equal, $t_{pwP} \neq t_{pwN}$.Thus, t_{pwN} can be controlled together with the negative voltage pulse initial d-current $i_{dN,ref}$ in a manner that a better symmetry for the d- and q-current responses upon positive and negative voltage pulse can be obtained.
- An optimum symmetry implies a setup where in addition to the q-current symmetry, $i_{qP} = i_{qN}$, the d-current traces cross in the middle of the corresponding voltage pulse, (4-31). Such symmetry is discussed in detail in the next section where a magnet temperature estimation based on a positive and negative voltage pulse is used for magnet temperature estimation under load conditions.

$$i_{dP}\left(\frac{t_{1P}-t_{0P}}{2}\right) = i_{dN}\left(\frac{t_{1N}-t_{0N}}{2}\right) \tag{4-31}$$

4.5 Sensorless Magnet Temperature Estimation under Load Conditions

In the analyses presented in section 4.3 and 4.4 it was assumed that the q-current is zero in the machine at the beginning of a voltage pulse when estimating the temperature of the permanent magnets. This is because due to cross-coupling effects in the machine, the slope of the d-current response di_d/dt will get indirectly affected by the q-current i_q. A non-zero q-current, $i_q \neq 0$, will produce a flux in the d-axis changing the saturation level of the machine in the d-axis.

In the section, magnet temperature estimation under load conditions is presented. This implies that upon voltage pulse generation the q-current in the machine is not zero $i_q \neq 0$. Thus, neglecting saturation effects due to eddy currents, the resulting d-current response di_d/dt will predominantly reflect saturation effects caused by the stator flux linkage in the d-axis produced by the q-current, d-current and the permanent magnet excitation. Naturally this will lead to more complicated relationship between the d-current slope di_d/dt and the magnet temperature T_m. Thus, when $i_q \neq 0$, the relationship given in (4-10) can be rewritten as follows:

$$\frac{di_d}{dt} = f\left(i_q, i_d, T_m\right). \tag{4-32}$$

The degree of non-linearity of the relationship (4-32) strongly depends on the construction type and the design of the machine. In machines with bigger effective air gap, as it is the case in SPMSM, the cross-coupling inductances are lower than in IPMSM, which naturally reduces the influence of the q-current in (4-32). In the following, a methodology will be proposed how to compensate the influence of the q-current in the estimation of the magnet temperature T_m when the machine is operated under load conditions. The compensation approach given here was first reported in [82]. For better explanation, a notation as already listed in Table 4-10 is adopted here.

4.5.1 Q-current Influence Compensation

Upon a voltage pulse in the d-axis of the motor, the actual q-current in the machine at time instant of the beginning of the voltage pulse influences the resulting d-current response di_d/dt in two different ways:

- The effective voltage in the d-axis of the machine that produces the d-current response di_d/dt is strongly dependent of the q-current i_q and the motor speed. The flux produced by the q-current in the q-axis generates speed dependent voltage in the d-axis of the machine. On the other hand, due to cross coupling effects, a change in the q-current additionally produces a voltage in the d-axis of the machine.
- D-current response di_d/dt is inherently influenced by the saturation level of the machine in its d-axis. Due to cross-saturation phenomena, the q-current i_q contributes to the overall saturation level in the d-axis of the motor and thus affecting indirectly di_d/dt .

The proposed q-current compensation here handles these two effects separately.

Effective Voltage in the D-axis of the Motor upon Pulse Generation

Compared to the analyses and assumptions made in section 4.4.1 and 4.4.2, the q-current is not zero at the time instant of the begging of the voltage pulse, $i_{q,ref} \neq 0$, however the compensation approach with respect to the effective d-axis voltage is the same. For convenience, the equations (4-23) and (4-24) from section 4.4.2 are given again. Upon a positive voltage pulse in the d-axis of the machine, the effective voltage space vector applied to the motor terminals has the components $u_d = 2/3V_{dc}$ and $u_q = 0$. Thus, under the assumption of negligible short voltage pulse with respect to the maximum operating speed, the motor voltage equations are:

$$L_{dd}^{*}\frac{di_d}{dt} = \frac{2}{3}V_{dc} - R_s i_d \overbrace{-L_{dq}^{*}\frac{di_q}{dt}}^{Term\ 1} + \overbrace{\omega L_{qq} i_q}^{Term\ 2} + \overbrace{\omega L_{qd} i_d}^{Term\ 3} \tag{4-33}$$

$$L_{qq}^{*}\frac{di_q}{dt} = -R_s i_q - L_{qd}^{*}\frac{di_d}{dt} - \omega L_{dd} i_d - \omega L_{dq} i_q - \omega \psi_M. \tag{4-34}$$

Assuming a machine operating point where the q-current is positive and the d-current is zero at the time instant of the beginning of the voltage pulse, ($i_{q,ref} > 0$ and $i_{d,ref} = 0$), the amplitude of the effective voltage $L_{dd}^{*} di_d/dt$ working on the d-axis of the motor

along a positive voltage pulse will be significantly influenced by $Term\ 2$ over the speed, according to (4-33). Furthermore, at higher speed according to (4-34), the q-current will change along the voltage pulse which will cause additional change of the amplitude of the effective voltage $L_{dd}^{*} di_d/dt$ due to $Term\ 1$ in (4-33). Similar to the approach presented in section 4.4.2, a solution is provided by considering not only a positive but also a negative voltage pulse in the d-axis of the motor, whereby for a given motor speed the q-current developed along the positive and negative voltage pulse is the same:

$$i_{qP} = i_{qN}. \tag{4-35}$$

Under the condition (4-35), a symmetry can be created, where in contrast to (4-33) by building the voltage equation difference (4-36) the influence of $Term\ 1$ and $Term\ 2$ on the effective voltage $L_{ddP}^{*} di_{dP}/dt\ - L_{ddN}^{*} di_{dN}/dt$ is eliminated.

$$\begin{aligned} L_{ddP}^{*}\frac{di_{dP}}{dt} - L_{ddN}^{*}\frac{di_{dN}}{dt} &= \frac{4}{3}V_{dc} - R_s(i_{dP} - i_{dN}) \\ &\quad - \overbrace{L_{dq}^{*}\left(\frac{di_{qP}}{dt} - \frac{di_{qN}}{dt}\right)}^{=0} + \overbrace{\omega L_{qq}(i_{qP} - i_{qN})}^{=0} \\ &\quad + \omega L_{qdP} i_{dP} - \omega L_{qdN} i_{dN} \end{aligned} \tag{4-36}$$

Cross-saturation Effects and Operating Point Considerations

Figure 4-40 demonstrates a simplified presentation of the flux saturation effects that occur in the machine upon voltage pulse generation and visualizes at the same time the positive and negative voltage pulses as applied with respect to the machine operating point. When a positive voltage pulse is applied in the d-axis of the motor, the d-current i_{dP} increases and consequently the d-current excitation ψ_{i_d} increases too. Analogically, upon a negative voltage pulse, the d-current i_{dN} decreases whereby the d-current excitation ψ_{i_d} declines. To make sure that the d-current responses of a positive and negative voltage pulse are affected alike by the permanent magnet excitation, d-current excitation ψ_{i_d} should vary symmetrical with respect to the positive and negative voltage pulse, as shown in Figure 4-40. In practice, such symmetry is very difficult to

establish. Therefore, in this investigation the problem is confined only to achieve symmetry of the d-currents in a manner that $i_{dP} = i_{dN}$ in the middle of the positive and negative voltage pulse respectively:

$$i_{dP\left(\frac{p_1-p_0}{2}\right)} = i_{dN\left(\frac{p_1-p_0}{2}\right)}. \tag{4-37}$$

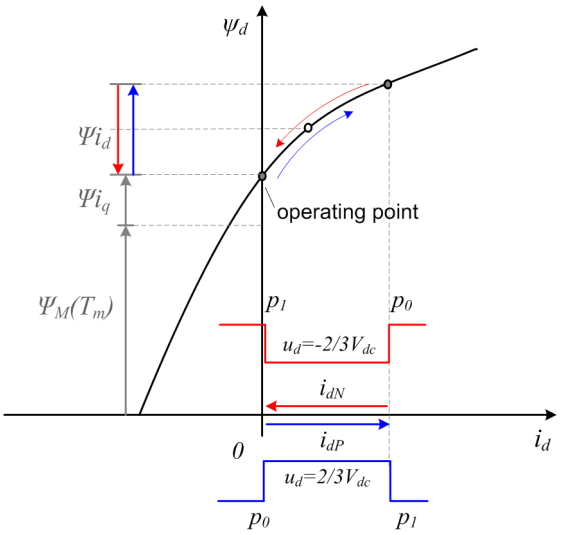

Figure 4-40: Simplified presentation of main flux saturation effects in the d-axis of the motor due to permanent magnet flux linkage ψ_M, q-current excitation ψ_{i_q} and d-current excitation ψ_{i_d} upon voltage pulse generation.

As a consequence of the d-current symmetry expressed in (4-37), the resulting d-axis inductances seen by the d-current upon positive and negative voltage pulse can be assumed to a great extent equal, since the d-current responses i_{dP} and i_{dN} operate in the same area.

$$L^*_{ddP} \approx L^*_{ddN} = L^*_{dd} \tag{4-38}$$

Analogically, the cross-coupling inductances can be assumed equal too:

$$L^*_{qdP} \approx L^*_{qdN} = L^*_{qd}. \tag{4-39}$$

Thus, equation (4-36) can be given in the following form

$$L^*_{dd}\frac{d(i_{dP} - i_{dN})}{dt} = \frac{4}{3}V_{dc} - R_s(i_{dP} - i_{dN}) + \omega L_{qd}(i_{dP} - i_{dN}). \tag{4-40}$$

This means that if the same effective pulse width is used for the positive and negative voltage pulse, the corresponding d-current response curves can be subtracted straight forward as follows:

$$i_{dPN} = i_{dP} - i_{dN}. \tag{4-41}$$

Further consequence of the d-current symmetry expressed in (4-37) is the reduction of the influence of the terms $R_s(i_{dP} - i_{dN})$ and $\omega L_{qd}(i_{dP} - i_{dN})$ in (4-40), since theoretically these will decline to zero, $R_s(i_{dP} - i_{dN}) = 0$ and $\omega L_{qd}(i_{dP} - i_{dN}) = 0$, in the middle of the voltage pulse, as $i_{dPN\left(\frac{p_1 - p_0}{2}\right)} = 0$ according to (4-37) and (4-41).

Because of cross-saturation effects, the q-current i_q creates a flux ψ_{i_q} in the d-axis of the motor contributing to the overall saturation level in this axis, see Figure 4-40. Thus, the difference of the d-current responses $d(i_{dP} - i_{dN})/dt$ is still strongly dependent of i_q, although this dependency is not obvious in (4-40). The relationship between $d(i_{dP} - i_{dN})/dt$ and i_q due to cross-saturation effects in the d-axis of the machine can be only identified by measurements. Measuring $d(i_{dP} - i_{dN})/dt$ as function of i_q should be carried out at constant magnet temperature ($T_m = const$) since the permanent magnet excitation should be kept constant. This is discussed in detail in section 4.5.3. In the next, a procedure will be defined that considers the current response symmetry with respect to the q-current i_q according to (4-35) and with respect to the d-current i_d according to (4-37).

4.5.2 Procedure Definition and Experimental Validation

For the sake of simplification, it is assumed here that the operating point of the machine under load conditions is defined solely by the reference q-current $i_{q,ref}$ in the field oriented current control while the reference d-current $i_{d,ref}$ is kept constant, $i_{d,ref} = const$. In this particular investigation the reference d-current is set to zero, $i_{d,ref} = 0$. Although, this is a well adopted approach in the field oriented current control of SPMSM, this is not obligatory especially when considering MTPA control of IPMSM. The objective here is confined to the problem to define magnet temperature estimation procedure which respects to a great extent the actual motor operating point defined by the q-current in the machine. A maximum sensitivity approach of $d(i_{dP} - i_{dN})/dt$ with respect to the magnet temperature T_m is not pursuit in the current investigation. Thus, based on the theoretical approach defined here with respect to the q- and d-current

response symmetry according to (4-35) and (4-37), the following procedure can be derived:

- At lower speeds, for a constant q-current in the machine $i_{q,ref} = const$, the initial d-current at the beginning of the positive voltage pulse is zero, $i_{dP(p_0)} = i_{d,ref} = 0$, and the initial q-current is kept unchanged, $i_{qP(p_0)} = i_{q,ref}$. In contrast, the initial d-current of the negative voltage pulse $i_{dN(p_0)}$ is controlled according to the condition that i_{dP} and i_{dN} become equal in the middle of the positive and negative voltage pulses respectively. Such control is visualized in Figure 4-41a where the d-current responses of the positive and negative voltage pulse cross in the middle of the pulse.

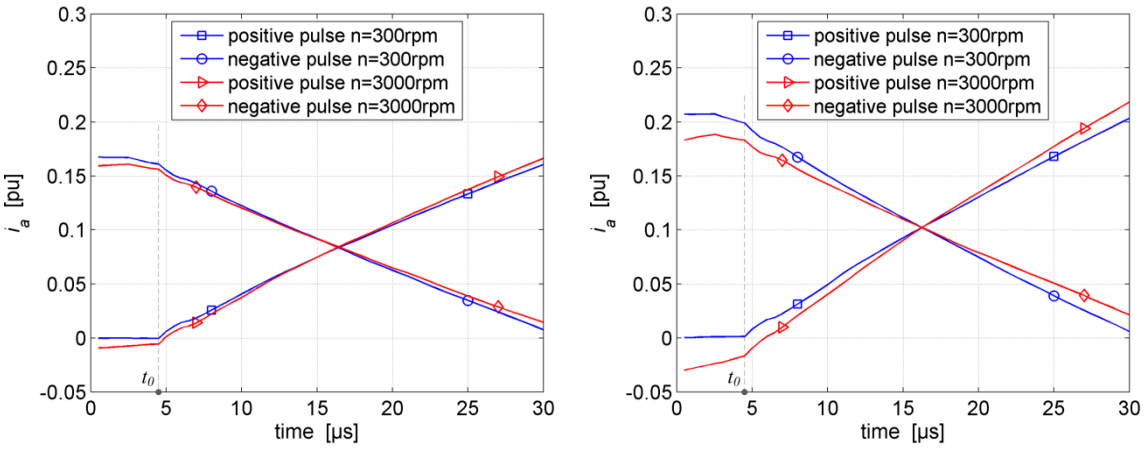

Figure 4-41: Q-current influence compensation approach: The d-current i_d response upon positive and negative voltage pulse in the d-axis of the motor for n=300rpm and n=3000rpm; $V_{\mathrm{dc}} = 750\mathrm{V}$; (a) $i_{q,ref} = 0.2\mathrm{pu}$; (b) $i_{q,ref} = 1.0\mathrm{pu}$.

- At higher speeds, the d-current responses are affected by additional induced voltage terms, as discussed in (4-33). Therefore, at higher speeds $i_{dP(t_0)}$ and $i_{dN(t_0)}$ should be adjusted so that (4-37) is still respected. In other words, for the investigated speed range here n=300rpm and n=3000rpm, the d-current curves at n=3000rpm have to cross in the middle of the voltage pulse as the d-current curves at n=300rpm, Figure 4-41. The degree of adjustment depends on the initial q-current in the machine upon voltage pulse generation. This can be comparatively observed in Figure 4-41a and Figure 4-41b, for $i_{q,ref} = 0.2pu$ and $i_{q,ref} = 1.0pu$ respectively. The purpose of the demonstrated control is to obtain symmetrical d-current excitation ψ_{i_d} upon positive and negative voltage

pulse along the entire investigated speed range. With respect to the operating point of the machine, this means that the operating point moves upward from its origin upon a positive voltage pulse and downward to its origin upon a negative voltage pulse, as demonstrated in Figure 4-40.

- Similar considerations are valid for the q-current control upon voltage pulse generation. While at lower speed $i_{qP(t_0)} = i_{q,ref}$, at higher speed $i_{qP(t_0)}$ and $i_{qN(t_0)}$ should be adjusted accordingly so that the q-current response curves, if not equal, at least cross in the middle of voltage pulse. This is visualized in Figure 4-42 where the q-current response is plotted for n=300rpm and n=3000rpm, and for $i_{q,ref} = 0.2pu$ and $i_{q,ref} = 1.0pu$ respectively. The initial values of the curves indicate the required adjustment. The purpose of the q-current control is to obtain, if not constant, at least symmetrical excitation ψ_{i_q} upon positive and negative voltage pulse along the entire investigated speed range.

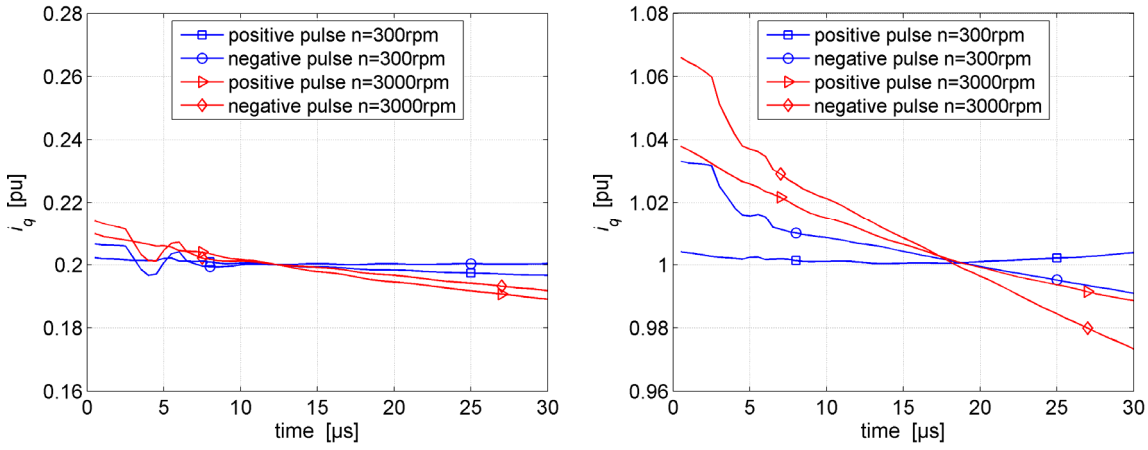

Figure 4-42: Q-current influence compensation approach: The q-current i_q response upon positive and negative voltage pulse in the d-axis of the motor for n=300rpm and n=3000rpm; $V_{\mathrm{dc}} = 750\mathrm{V}$; (a) $i_{q,ref} = 0.2\mathrm{pu}$; (b) $i_{q,ref} = 1.0\mathrm{pu}$.

Experimental results obtained under the procedure described above are carried out at various machine operating points and speed n=300rpm and n=3000rpm. Owing to the direction of the machine currents and the pulse polarity, the beginning of the positive effective voltage pulse in the machine is delayed by t_{TD} compared to the beginning of the negative effective voltage pulse. This has been explained already in section 4.1.3. In

order to keep the effective pulse width same for the positive and negative voltage pulse, in the current experimental setup the switching command of the negative voltage pulse is artificially delayed by the inverter dead time t_{TD}. Thus, the measured effective d-current response upon positive and negative voltage pulse would start at the same time instant t_0, see Figure 4-41. This makes it possible to subtract straightforward the corresponding d-current response curves $i_{dP} - i_{dN}$ and obtain a resulting i_{dPN} current curve. Under load conditions, both, the slope of the d-current response of the positive and negative voltage pulse, di_{dP}/dt and di_{dN}/dt, are strongly affected by the speed and therefore neither of them can be used as indicator for the magnet temperature T_m However, under the presented procedure, the difference of the d-current responses $i_{dP} - i_{dN}$ are speed independent for a given machine operating point, $i_{q,ref} = const.$ This is demonstrated in Figure 4-43a for $i_{q,ref} = 0.2pu$ and in Figure 4-43b for $i_{q,ref} = 1.0pu$, where at a constant magnet temperature ($T_m = 60°C$) the resulting $i_{dP} - i_{dN}$ curves are depicted for n=300rpm and n=3000rpm.

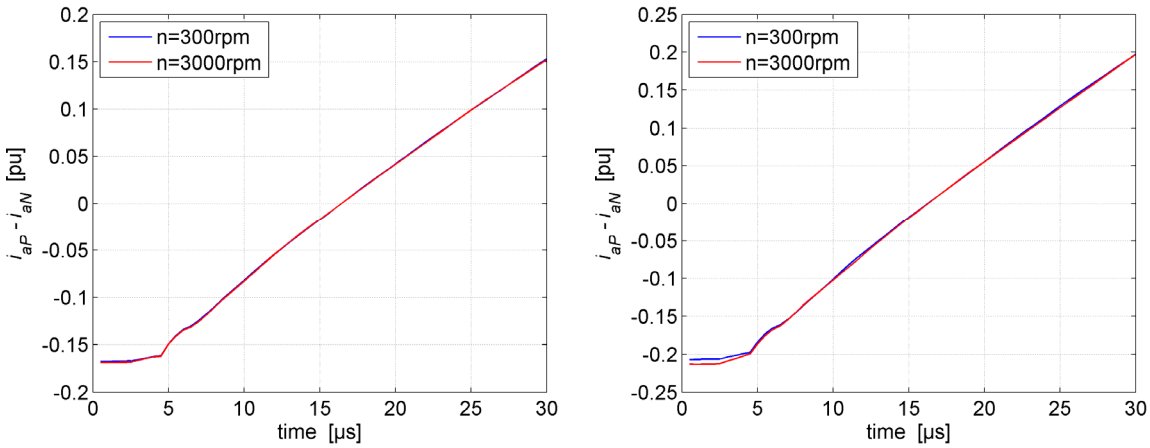

Figure 4-43: Q-current influence compensation approach: The difference $i_{dP} - i_{dN}$ between the d-current response curves upon a positive and negative voltage pulse in the d-axis of the motor at motor speed n=300rpm and n=3000rpm; constant magnet temperature $T_m = 60°C$; $t_{pw} = 30\mu s$; $V_{dc} = 750V$; (a) $i_{q,ref} = 0.2pu$; (b) $i_{q,ref} = 1.0pu$.

The difference of the d-current curves upon a positive and negative voltage pulse $i_{dP} - i_{dN}$ for various reference magnet temperatures T_m are demonstrated for motor speed n=300rpm in Figure 4-44a for $i_{q,ref} = 0.2pu$ and in Figure 4-44b for $i_{q,ref} = 1.0pu$.

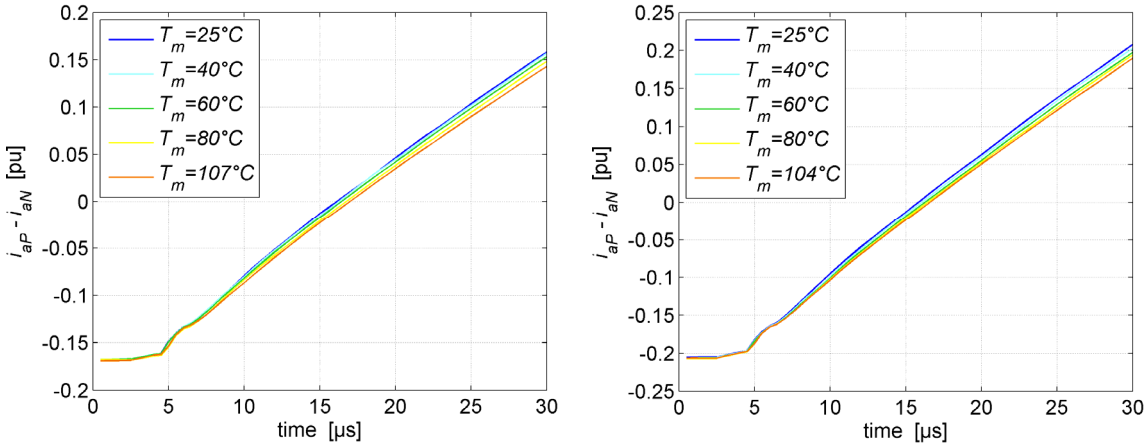

Figure 4-44: Q-current influence compensation approach: The difference $i_{dP} - i_{dN}$ between the d-current response curves upon a positive and negative voltage pulse in the d-axis of the motor at motor speed n=300rpm and n=3000rpm; at various magnet temperatures T_m; $t_{pw} = 30\mu s$; $V_{\mathrm{dc}} = 750\mathrm{V}$; (a) $i_{q,ref} = 0.2\mathrm{pu}$; (b) $i_{q,ref} = 1.0\mathrm{pu}$.

In contrast to (4-30), the slope evaluation is carried out here on the d-current response difference, whereby S_{aPN} is the linearised slope of the effective resulting curve difference $i_{dP} - i_{dN}$, as plotted in Figure 4-43 and Figure 4-44. The obtained linearised current slopes S_{aPN} for $i_{q,ref} = 0.2;\ 0.3;\ 0.4;\ 0.6;\ 0.8;\ 1.0pu$ are depicted in Figure 4-45 as a function of the magnet temperature T_m for speed n=300rpm and n=3000rpm. The corresponding S_{aPN} values are the mean values obtained over 25 measurements conducted at the same reference temperature, reference q-current $i_{q,ref}$ and motor speed. Comparing the plots of Figure 4-45 for the various q-currents, there is a clear dependency of di_{dPN}/dt from the q-current in the machine under the applied procedure. However, this dependency is no longer due to speed or q-current dependent voltage terms but due to cross-saturation effects produced by the q-current excitation in the d-axis of the motor. For a given machine, this dependency can only be identified by measurements. For this purpose, measurements of S_{aPN} are carried out at constant reference magnet temperatures $T_m = 25;\ 40;\ 60;\ 80°C$ and various q-currents $i_{q,ref} = 0.2;\ 0.3;\ 04.;\ 0.6;\ 0.8;\ 1.0pu$. The obtained results are depicted in Figure 4-46. The best scenario with respect to a magnet temperature estimation procedure would be if the relationship between S_{aPN} and i_q is linear and not influenced by the magnet temperature. As the obtained curves in Figure 4-46 show, for the IPMSM under test, linearity is observed for $i_q > 0.4pu$. Furthermore, it can be observed that for this particular machine the relationship between S_{aPN} and i_q is practically independent from the magnet temperature T_m, since the shape of the curve does not significantly change

for various magnet temperatures. This is an important aspect as it substantially simplifies the identification of a magnet temperature estimation procedure under load conditions.

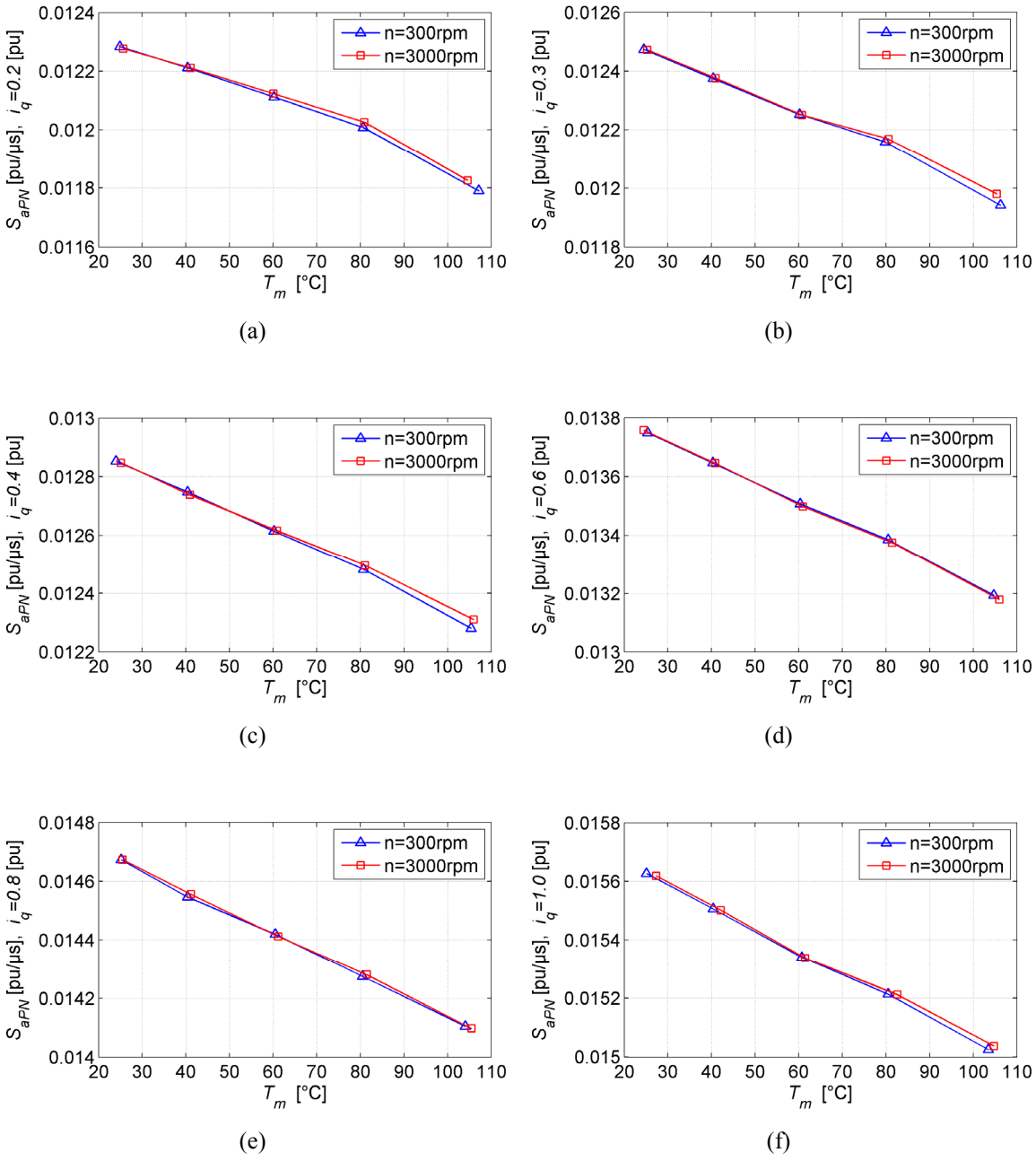

Figure 4-45: Q-current influence compensation approach: The slopes S_{aPN} of $i_{dP} - i_{dN}$ as a function of the magnet temperature T_m for motor speed n=300rpm and n=3000rpm; $t_{pw} = 30\mu s$; sample rate 500ns; $V_{\mathrm{dc}} = 750\mathrm{V}$;
(a) $i_q = 0.2pu$; (b) $i_q = 0.3pu$; (c) $i_q = 0.4pu$; (d) $i_q = 0.6pu$; (e) $i_q = 0.8pu$; (f) $i_q = 1.0pu$.

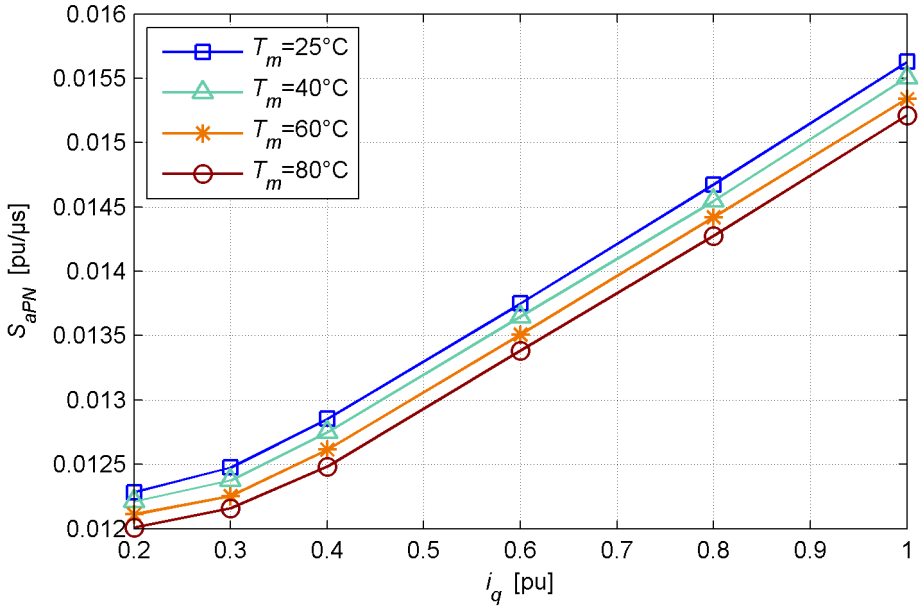

Figure 4-46: Q-current influence compensation approach: The slopes S_{aPN} of $i_{dP} - i_{dN}$ as a function of the q-current i_q captured at various magnet temperatures and motor speed n=300rpm; $V_{\mathrm{dc}} = 750\mathrm{V}$.

4.5.3 Identification of Magnet Temperature Estimation Procedure under Load Conditions

Identification of a magnet temperature estimation procedure under load conditions for a given motor requires the relationship between S_{aPN} and T_m at various q-currents i_q. This will give a two-dimensional identification LUT, which is normally cumbersome to establish. If the relationship between S_{aPN} and i_q can be assumed independent of the magnet temperature T_m, for a given motor it is sufficient to identify the relationship at a single magnet temperature ($T_m = const$) and assume it constant along the entire motor operating temperature range. Thus, the identification of the required two-dimensional LUT is confined to the task to identify two separate one-dimensional LUTs as follows:

- LUT_1 contains the measured values of S_{aPN} at various magnet temperatures. The measurements should be carried out at a constant q-current. A preferable value for the q-current is the middle value with respect to the q-current range the machine will be operated within, $i_{q(mid)}$.

$$S_{aPN[i_{q(mid)}]} = \mathrm{LUT}_1\{T_m\} \tag{4-42}$$

- LUT_2 contains the measured values of S_{aPN} at various q-currents. The measurements should be carried out at a constant reference magnet temperature. Analogically, a preferable reference magnet temperature is the middle value with respect to the temperature range $T_{m(mid)}$, at which the machine will be operated.

$$S_{aPN[T_{m(mid)}]} = \text{LUT}_2\{i_q\} \tag{4-43}$$

Table 4-12 demonstrates the assembling of the required two-dimensional LUT from LUT_1 and LUT_2. The rest of the elements $S_{aPN[i_{qx},T_{my}]}$ that are not directly estimated by measurements can be calculated as follows:

$$S_{aPN[i_{qx},T_{my}]} = S_{aPN[i_{qx},T_{m(mid)}]} + S_{aPN[i_{q(mid)},T_{my}]} - S_{aPN[i_{q(mid)},T_{m(mid)}]}. \tag{4-44}$$

Table 4-12: An example of assembling two-dimensional LUT from the corresponding one-dimensional tables $S_{aPN[i_{q(mid)}]} = \text{LUT}_1\{T_m\}$ and $S_{aPN[T_{m(mid)}]} = \text{LUT}_2\{i_q\}$ for commissioning magnet temperature estimation procedure under load conditions.

				LUT_1		
		i_{q1}	i_{q2}	$i_{q3(mid)}$	i_{q4}	i_{q5}
	T_{m1}			$S_{aPN}[i_{q3},T_{m1}]$		
	T_{m2}			$S_{aPN}[i_{q3},T_{m2}]$		
LUT_2	$T_{m3(mid)}$	$S_{aPN}[i_{q1},T_{m3}]$	$S_{aPN}[i_{q2},T_{m3}]$	$S_{aPN}[i_{q3},T_{m3}]$	$S_{aPN}[i_{q4},T_{m3}]$	$S_{aPN}[i_{q5},T_{m3}]$
	T_{m4}			$S_{aPN}[i_{q3},T_{m4}]$		
	T_{m5}			$S_{aPN}[i_{q3},T_{m5}]$		

It should be noted here that equation (4-44) is valid only if there is a common overlapping point $S_{aPN[i_{q(mid)},T_{m(mid)}]}$ in LUT_1 and LUT_2 which is represented in Table 4-12 by the point $S_{aPN}[i_{q3},T_{m3}]$. Preferably, the common point should be in the middle

of the established matrix. This will evenly distribute potential errors in the calculated slopes $S_{aPN[i_{qx},T_{my}]}$ generated by some lack of accuracy in measuring LUT_1 and LUT_2.

For better understanding of the Table 4-12 assembling, Figure 4-47 demonstrates graphically how an arbitrary point $S_{aPN[i_{qx},T_{my}]}$ can be interpolated from the measured curves (LUT_1 and LUT_2). The depicted curves are the actual measured curves for the machine under test with a common overlapping slope S_{aPN} set at $i_{q(mid)} = 0.6pu$ and $T_{m(mid)} = 60°C$. The curve $S_{aPN[T_{m(mid)}=60°C]}(i_q)$ from Figure 4-47 corresponds to LUT_2 in Table 4-12, while $S_{aPN[i_{q(mid)}=0.6pu]}(T_m)$ corresponds to LUT_1. This graphical presentation also demonstrates the reconstruction of the curves plotted in Figure 4-46, which were obtained by measurements.

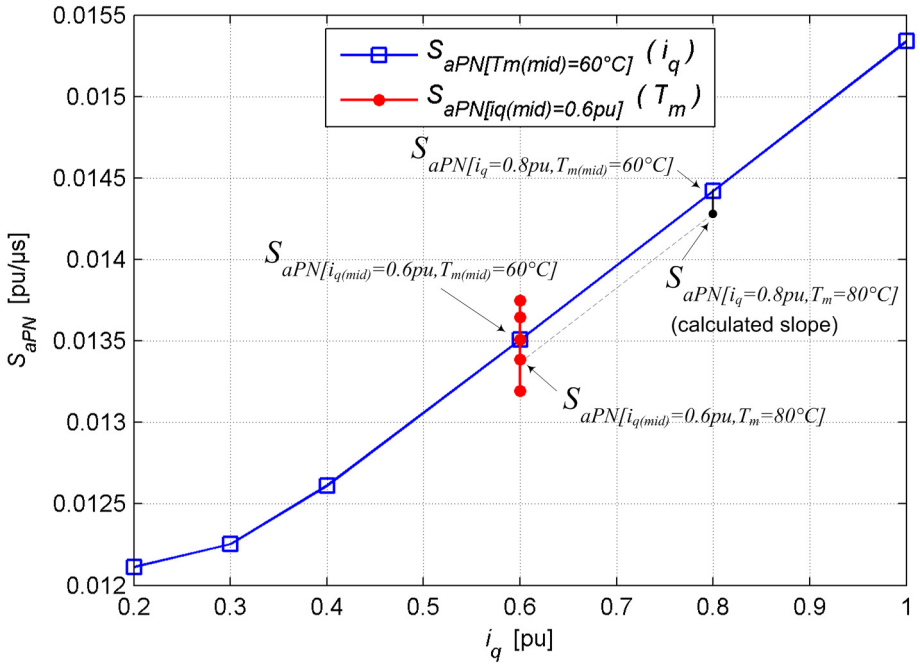

Figure 4-47: An example of graphical estimation of a slope S_{aPN} for a $i_q = 0.8pu$ and $T_m = 80°C$ using measured curves with middle values $i_{q(mid)} = 0.6pu$ and $T_{m(mid)} = 60°C$; motor speed n=300rpm.

4.5.4 Discussions

The proposed procedure does not perfectly respect the original operating point of the machine, since the current components at the beginning of the voltage pulse ($i_{dP(p_0)}$, $i_{dN(p_0)}$, $i_{qP(p_0)}$, $i_{qN(p_0)}$) should be controlled in a small range around the machine operating point in order to guarantee symmetrical excitation ψ_{i_d} and ψ_{i_q} along the voltage pulse. As shown in Figure 4-42 for $i_{q,ref} = 0.2pu$ and $i_{q,ref} = 1.0pu$, the deviation from the original operating point increases while the q-current and the motor speed increases. For the machine under test the maximum deviation is less than 8% for $i_{q,ref} = 1.0pu$ and motor speed n=3000rpm, Figure 4-42b.

As already pointed out in [82], the consideration how the voltage pulses are applied with respect to the machine operating point should be met with regard to the machine design and control application requirements. Theoretically, a voltage pulse generation can be realized also around the machine operating point, which will mean $i_{d(ref)} < 0$ for the positive voltage pulse and $i_{d(ref)} > 0$ for the negative voltage pulse, according to Figure 4-40.

For a machine with originally weak saturation level in the d-axis, magnet temperature estimation under load conditions will be difficult or in the worst case impossible to implement. The proposed method gives best results around operating points at which the d-axis of the machine starts to saturate along the test pulses. If a machine originally reveals week saturation level, prior to a test pulse generation an additional positive d-current in the machine will be necessary to increase the method sensitivity. This will consequently lead to a further deviation from a desired motor operating point. Therefore, the proposed temperature estimation under load condition would have inherently low application range. The applicability will be further hindered especially in the case of low saturated IPMSM, where a negative d-current is often required in order to obtain MTPA control of the machine or in the field weakening control.

4.6 Outlook

A commissioning of a magnet temperature estimation procedure requires a knowledge of the magnet temperature in order to establish a LUT that associates a given d-current response di_d/dt with an absolute magnet temperature T_m. The direct temperature measuring device used in the current investigation would not be normally the first choice since its usage requires significant construction and assembly efforts. A solution can provide an infrared camera mounted in a hole through the stator enclosure as it has been used in [23], [25], [26]. A more simple approach is to establish a constant reference temperature level inside the machine for sufficiently long time in order to ensure thermal balance where the stator and rotor temperature can be considered equal. This can be realized by heating-up the motor in an environmental chamber or by controlling the winding currents in a manner that a constant stator temperature can be maintained in the machine for a time long enough. This would require a temperature sensor in the stator core but this is meanwhile standard in most modern machines.

In general, the accuracy of the proposed method strongly depends on the current sensors. In this particular investigation, the used current sensors are factory integrated in the inverter. According to the data sheets the sensors have a temperature coefficient of 0.003%/C and accuracy of ±0.65%. The current sensors are dimensioned for maximum current exceeding almost 4 times the nominal current of the machine. It is opinion of the author that with better selected and dimensioned current sensors a higher accuracy in measuring the d-current response can be achieved and thus improving the accuracy of the estimated magnet temperature.

In the current investigation, the stator winding resistance and its temperature dependency has been completely neglected. The method accuracy can be further improved if this is considered. In this case a winding temperature sensor would be required.

As it has been shown in the distribution of the measurements given in Figure 4-25, Figure 4-29, Figure 4-33 and Figure 4-38, a correct estimation of a magnet temperature level is strongly related to the number of measurements that can be conducted for calculating a mean value. Naturally, more measurements will lead to better accuracy. However, a trade-off should be found in each application since every measurement is related with short interruption of the motor normal operation. For example, in the setups described in section 4.3 and 4.4, it should be considered that the load current is set to zero for a time duration bigger or equal 3 to 5 times the motor electrical time constant before a voltage pulse can be generated.

5 Practical Realization Issues

The chapter discusses the practical realization of the proposed method and its validation setup. An accent is put on the hardware implementation and software integration of magnet temperature estimation routines into a field oriented control. Furthermore, the design and implementation of the temperature monitoring system used in the current investigation is presented in detail.

5.1 Hardware and Software Implementation

In the present section, a software and hardware implementation of the motor control unit (MCU) used in the current investigation is given. Although the MCU is specially designed for the validation process of the proposed magnet temperature estimation technique, it reveals many characteristics for potential hardware and software end-implementation. The main advantage of the MCU is that, it consists of a single floating point DSP that runs the motor control routines, the magnet temperature estimation procedure and the user interface protocol functions. The current oversampling mechanism, which is required for capturing the motor currents upon voltage pulse generation, is implemented solely by optimized programming of the DSP peripherals and does not involve the use of FPGA.

First the main aspects of the software implementation will be discussed, whereby an integration of a magnet temperature estimation procedure in a FOC will be demonstrated. Secondly, the hardware with main accent on the implementation of the currents oversampling mechanism will be presented.

5.1.1 Software Implementation

As it has been shown in section 4.3, section 4.4 and section 4.5, depending on the applied magnet temperature estimation approach, different machine operating points should be established in the machine prior to generation of a voltage pulse in the d-axis of the motor. Therefore, a software implementation of a magnet temperature estimation procedure would vary accordingly. However, there are two major software routines that reveal general character, independent of the selected magnet temperature estimation procedure and the applied motor control: a Voltage Pulse Generator (VPG) routine and a Current Slope Estimation (CSE) routine.

Voltage Pulse Generator (VPG) Routine

The VPG is responsible for the generation of a voltage pulse in the positive or negative d-axis of the motor. A voltage pulse generation in the d-axis of the machine is realized here by applying the basic space vectors $\underline{V}_{1(100)}$ for positive and $\underline{V}_{4(011)}$ for negative voltage pulse. Thus, detecting the d-axis in a rotating machine is confined to predicting the moment when the angle between the stator and rotor oriented reference frames equals zero, $\theta = 0$. The angle θ is derived from the mechanical rotor position θ_r. Thus, in the beginning of every PWM period, $PWM_{prd(n)}$, a software subroutine within VPG, denominated here as d-axis tracer, takes the mechanical rotor position θ_r as an input and estimates the value of θ with respect to the middle of an eventual voltage pulse that can be generated immediately after completion of the actual PWM period. A voltage pulse in the d-axis of the motor can be then generated when θ is expected to become zero at the middle of the pulse, as shown in Figure 5-1.

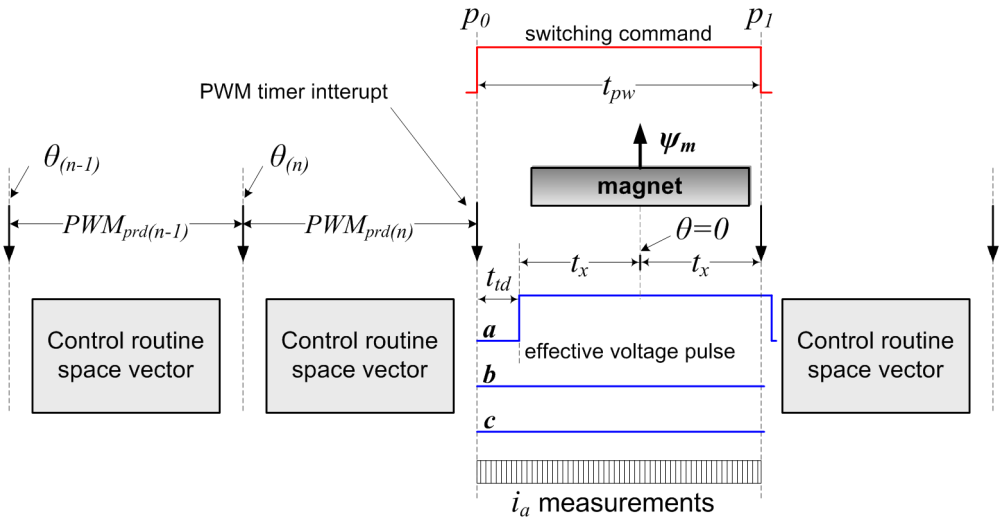

Figure 5-1: Time scheduling of the control algorithm and the generation of a positive voltage pulse in the d-axis of the machine upon magnet temperature estimation.

The angle θ is estimated with respect to the middle of an eventual voltage pulse with time duration t_{pw} according to the following calculation:

$$\theta = \theta_{(n)} + \frac{\Delta\theta_{(n)}}{PWM_{prd}}\left(PWM_{prd} + \frac{t_{pw} + t_{td}}{2}\right), \tag{5-1}$$

where

$$\Delta\theta_{(n)} = \theta_{(n)} - \theta_{(n-1)}. \tag{5-2}$$

According to (5-1), the generation of a voltage pulse considers the total delay time t_{td} between the beginning of the pulse switching command p_0 and the effective voltage pulse in the machine, as depicted in Figure 5-1. In contrast, the end of the effective voltage pulse is not of importance since the oversampling of the motor currents terminates with the end of the pulse switching command p_1, as already described in section 4.1.4. Therefore, the prediction of $\theta = 0$ is calculated with respect to the middle of the time instant $p_0 + t_{td}$ and p_1, as demonstrated in Figure 5-1. The delay time t_{td} varies depending on the direction of the machine currents and the voltage pulse polarity, as already discussed in section 4.1.3. The prediction of θ, as given in (5-1), is only valid in this form under the following conditions: the change in the machine speed from one PWM period to the next is negligible, $\Delta\theta_{(n+1)} \approx \Delta\theta_{(n)}$, and the mechanical rotor position θ_r is captured synchronously to the beginning of the PWM period.

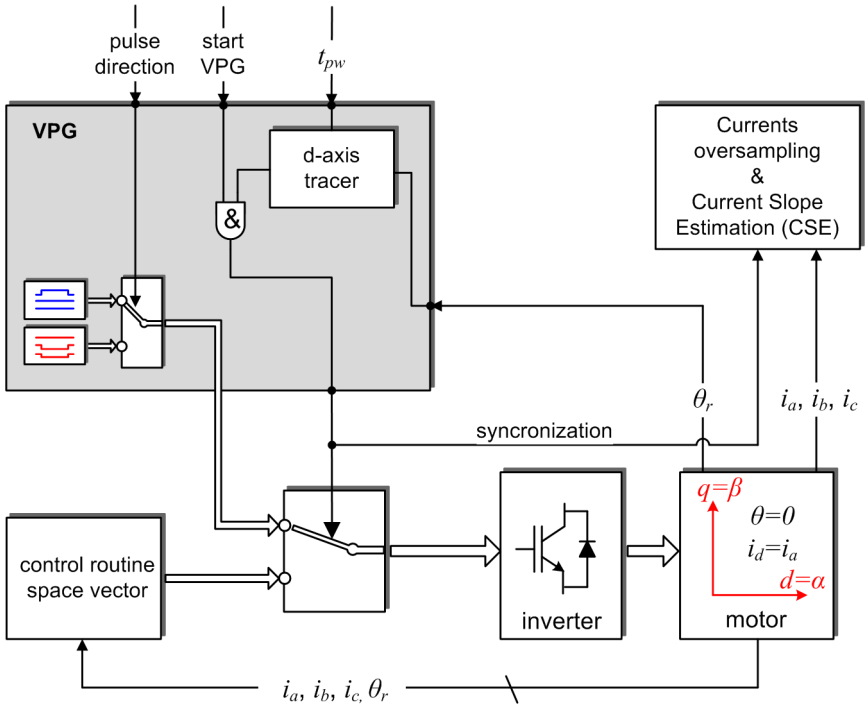

Figure 5-2: Integration of the voltage pulse generator (VPG) into the motor control scheme.

The integration of a VPG routine into a conventional field oriented control scheme (FOC) is demonstrated in the Figure 5-2. Every time the d–axis is detected according to the principle depicted in Figure 5-1, a software flag is set by the d-axis tracer which in a

combination with a start command forces interruption of the running control scheme and activates the VPG. The start command is usually generated by a control routine that establishes a required operating point in the machine prior to a voltage pulse generation. Once the VPG is activated, the control of the inverter switching signals is passed to the VPG. Thus, after completion of the actual PWM period, an inverter switching pattern corresponding to a positive or negative voltage pulse is applied to the motor terminals for the time duration of the desired pulse width t_{pw}. The switching patterns for a positive and negative voltage pulse have been already given in Figure 4-12. When a generation of a voltage pulse is completed, the control is given back to the original motor control routine by generating a PWM interrupt at the time instant p_1, as depicted in Figure 5-1.

Current Slope Estimation (CSE) Routine

The sensitivity of the proposed method depends strongly on the correct evaluation of the slope of the d-current response di_d/dt. As already discussed, the quantitative evaluation of di_d/dt is carried out on linearisation of the measured d-current curve, as given in (4-17) in section 4.3.3, whereby the slope of the linearised curve S_a is used as a figure of merit. The linearisation of the slope S_a is realized by applying linear regression calculation:

$$S_a = \frac{\sum_{i=0}^{n-1}\left(t_i - \overline{t}\right)\left(i_{a,i} - \overline{i}_a\right)}{\sum_{i=0}^{n-1}\left(t_i - \overline{t}\right)^2}\ , \tag{5-3}$$

where t_i is the relative sample time, $\overline{t}$ is the mean time, $i_{a,i}$ is the phase current i_a corresponding sample and $\overline{i}_a$ is the mean value over all samples. In the present investigation, with the proposed hardware implementation, the motor currents are sampled along the voltage pulse at a fixed rate of 500ns.

After a completion of a voltage pulse generation, the stored current samples are used by the CSE routine to calculate S_a according to (5-3). The computing time of the CSE routine depends strongly on the number of samples to be used in the linear regression. Thus, as the sample rate is fixed, CSE will have a variable executing time depending on the voltage pulse width t_{pw}. In contrast to the motor control software routines, CSE is not time critical task so that a CSE routine is programmed with the lowest priority as it should not interrupt the motor real time control. Such task scheduling is demonstrated in Figure 5-3, where a torque and speed field oriented control routines cannot be interrupted by the CSE routine. The CSE routine is triggered by a software interrupt

generated upon completion of the VPG. The depicted task scheduling is managed by the DSP operating system that defines the priority and the interruptability of each task.

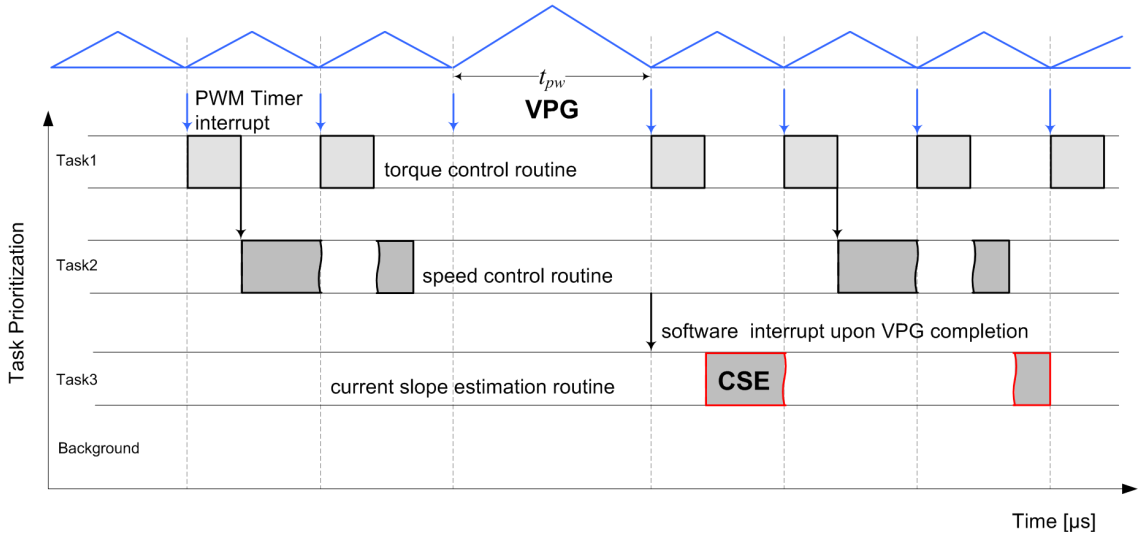

Figure 5-3: Task scheduling of the control routines and the current slope estimation (CSE) routine, source [83].

5.1.2 Hardware Implementation

The proposed temperature estimation technique together with the motor control embedded software is deployed on a single floating point DSP, TMS320C6747. The advantage of the C6747 is that it provides relatively high computing power, big internal memory, on-chip Pulse Width Modulation (PWM) peripheral for a space vector control of three-phase inverter and on-chip encoder logic peripheral for a rotor position sensor. In contrast to conventional microcontrollers used in motor control applications, TMS320C6747 does not have on-chip Analog Digital Converters (ADCs). However, this is not seen here as a disadvantage since most microcontrollers with on-chip ADC channels are anyway unsuitable for simultaneous sampling of all motor phase currents since their internal ADC channels are normally multiplexed. In order to obtain a noise free curve of the phase current i_a, which is essential for a correct magnet temperature estimation, it is strongly recommended to oversample simultaneously all motor currents (i_a, i_b, i_c) along a voltage pulse, and not only the phase current i_a. This is particularly important especially when current sensors are used which output is a voltage signal proportional to the measured current. If the current sensors output voltages are affected by noise, this noise is common for all three phases and can be successfully eliminated only if the motor currents samples are simultaneously captured. Therefore, for accurate

magnet temperature estimation, a clear recommendation is given here to the use of external high resolution ADC channels.

The proposed hardware setup here uses the external analog digital converter ADS8422. The converter has 16-bit resolution and maximum sample rate of 4MSPS. The ADS8422 time characteristics proved to fit very well with the time constraints of the Direct Memory Access (DMA) controller and the External Memory Interface (EMIF) of the TMS320C6747 so that a simultaneous triggering of up to three ADC channels at a sample rate of 500ns can be achieved. This is a value that can be normally reached only by the usage of a FPGA. Furthermore, the ADC triggering and read events are not governed by the CPU but from the DSP peripherals solely. The exact interaction between TMS320C6747 and ADS8422 has been separately handled in a Master Thesis [84] within the current project. In the following only major principles are given.

A block diagram of the proposed hardware setup is depicted in Figure 5-4. The output signal of an on-chip CAP (Capture Compare) unit of the TMS320C6747, programmed in this case as a PWM unit, triggers all ADCs channels simultaneously every 500ns during voltage pulse generation. The same signal is used to trigger the Direct Memory Access controller (DMA) which together with the External Memory Interface (EMIF) peripheral read the sample data and moves this to an array in the DSP internal memory without interrupting the CPU.

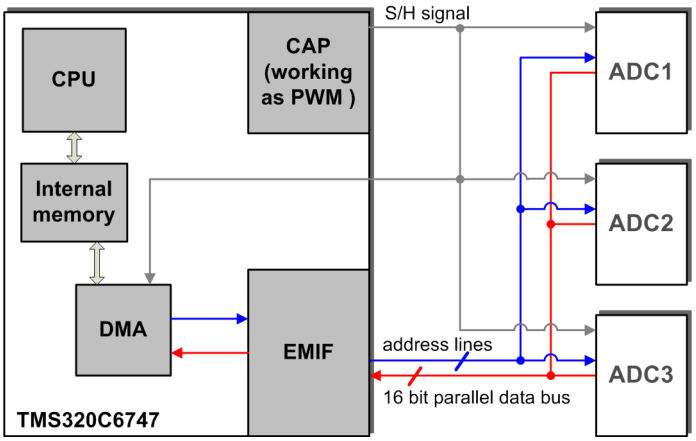

Figure 5-4: Block diagram of the implemented connectivity between the ADCs and the DSP, source [83].

The more detailed timing of the signals is shown in Figure 5-5. The ADC conversion time is 225ns, which is the time between the trigger event and the time instant when the data is ready to be read by the DSP. All ADC channels are triggered simultaneously on the falling edge of the Capture Compare Unit (CAP) output signal (ADC Sample and

Hold Signal). The rising edge of the same signal starts the DMA controller, which needs 230ns to initiate the first read event to the EMIF. Consequently, the EMIF needs 50ns to move the data to the DMA controller which in turn needs 90ns to store the data into the internal memory and initiate a new read event for the next ADC channel. Although the whole ADC trigger and read process takes 610ns for all three channels, due to the ADCs conversion time of 225ns, the data is not overwritten and it doesn't come into a conflict with the ADC triggering period of 500ns.

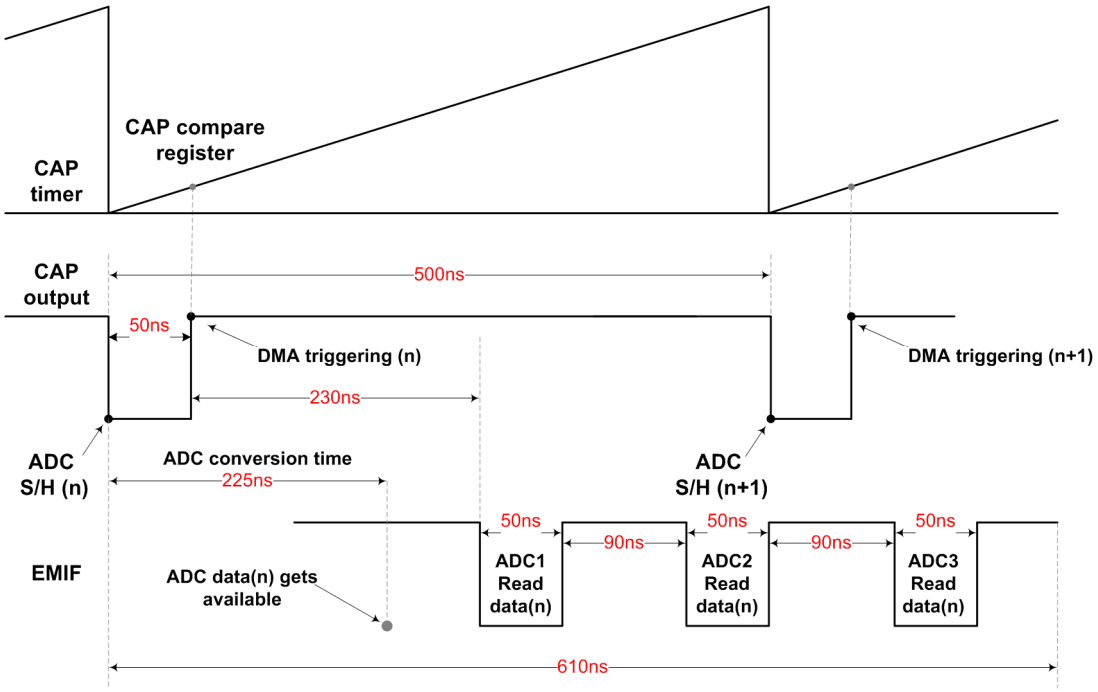

Figure 5-5: Time diagram of the ADCs sample and read events, source [83].

The presented hardware setup is not obligatory for a successful implementation of the proposed magnet temperature estimation technique. In order to measure the slope of the d-current response di_d/dt upon voltage pulse generation a dedicated current derivative sensor can be used as well. Such sensors gained recent popularity in motor control applications implying sensorless rotor position estimation, [85]–[88]. The use of a current derivative sensor in a magnet temperature estimation procedure will make an oversampling current mechanism and a current slope estimation routine obsolete. This will make possible hardware setups with cheaper microcontrollers, with significantly less computing power and peripheral capability as the one presented here (TMS320C6747).

From hardware point of view, a further simplification can be achieved by considering evaluation of the d-current response slope di_d/dt based on the difference of the initial and end current value, $\Delta i_a = i_{a(t_1)} - i_{a(t_0)}$, as depicted in Figure 4-20. In this case only two measurement points will be necessary to approximate di_d/dt. However, such implementation depends strongly on the quality of the measured current signals and can introduce some degradation in the accuracy of the magnet temperature estimation.

5.2 Rotor Temperature Monitoring Device

The rotor temperature monitoring device used in the experimental validation process of the proposed magnet temperature estimation method is described in the following. The measuring device is a tool that was specially built for the current investigation since monitoring of the instantaneous temperature of the permanent magnets was needed. The following guiding requirements were set prior to the device final design:

- Various locations on the surface and in the interior of the rotor are needed to be measured simultaneously so that an adequate axial and radial temperature distribution can be obtained.
- The rotating device must withstand spinning from standstill to up to 6000rpm.
- The electronic circuit should reveal high immunity to electromagnetic interferences in order to guarantee applicability in inverter fed motor applications.
- The data transmission must be 100% reliable against electromagnetic interferences.
- Autonomous compact power supply that guarantees at least 12 hours continuous operation.
- The instrumentation should be able to measure temperatures in the rotor of up to 180°C.
- Certain degree of flexibility in terms of data preprocessing. Such flexibility is seen as modifiable sample period, the possibility to apply digital filtering, time synchronization with other measuring systems, etc.
- Most suitable temperature sensors for less impact on the machine performance during operation.

Taking into considerations the majority of known techniques reported in the literature, that are used for measuring the rotor temperature in a rotating machine, a monitoring system design was derived that fulfils best these requirements. The implemented device is battery powered and based on contact measurements using thermocouples. It consists of a microcontroller for the data processing and infrared optical link for a noise free data transmission to a stationary receiver.

Circuit Design

Figure 5-6 shows a block diagram of the whole rotor temperature monitoring system. It consists of a rotating rotor temperature monitoring device and stationary receiver connected to a host PC. The selected thermocouples are of type K, which implies sensitivity of approximately 41µV/°C. Thermocouples as temperature sensors have been successfully used in various rotor temperature monitoring systems [16]–[18], [27], [89], [90]. Compared to resistance temperature detectors (RTDs) [19], [20], [91], thermocouples do not need a current or voltage source. This makes them more favoured when the circuit is battery powered. Furthermore, they are wide-spread, virtually available at any size and have relatively good linearity.

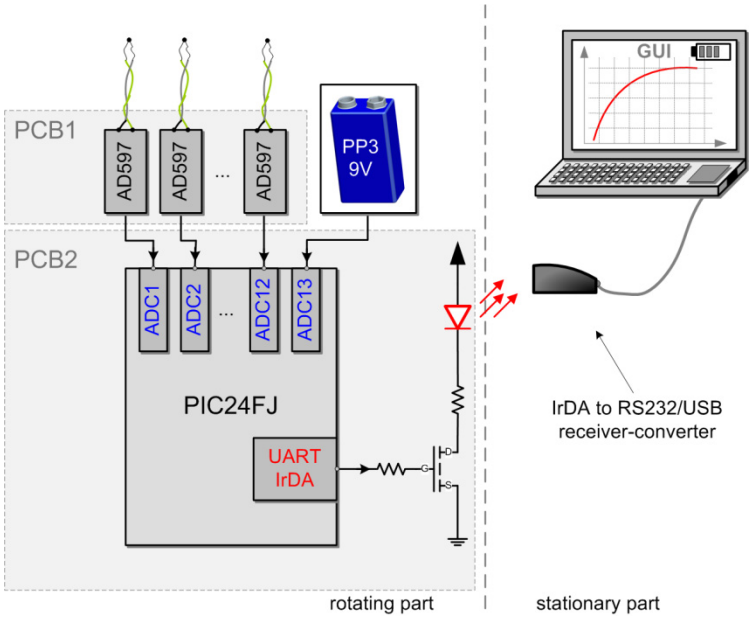

Figure 5-6: Block diagram of the rotor temperature monitoring system – signal data path; source [92].

According to the theory of thermocouples, the cold junction temperature should be known in order to measure the absolute temperature of the measuring point. Cold junction compensation and amplification of the thermocouple output voltage is realized here by a single integrated circuit (AD597 or AD595), referred to as thermocouple

conditioner. Thus, the thermocouple output voltage is converted to a voltage value that corresponds to an absolute temperature value with sensitivity of approximately 10mV/°C. This voltage is then directly sampled and converted by an analog digital converter (ADC) of a microcontroller. In this particular design a microcontroller of PIC24FJ family has been used. The 44 pin version of PIC24FJ has 13 ADCs on-chip, where 12 of them can be used for temperature measurements and one is permanently reserved for monitoring the battery voltage of the rotating instrumentation.

The circuitry of the rotating device is split on two printed circuit boards (PCBs), PCB1 and PCB2 as shown in Figure 5-6. PCB1 contains the thermocouple conditioner elements while PCB2 contains the microcontroller, the power electronic circuit, the infrared light-emitting diode (LED) and its driver circuit. This approach is chosen deliberately, since a PCB1 with different thermocouple conditioners topologies can be used, while the layout of PCB2 is considered constant. There are two thermocouple conditioner elements considered here, AD597 and AD595, both suitable for thermocouples of type K. The difference between the two is the size and the accuracy. While the AD597 is very small and has an accuracy of ±4°C, AD595 is almost 3 times bigger in size compared to AD597 but has an accuracy of ±1°C. Therefore, depending on the requirements with respect to the accuracy and the number of simultaneously measured temperature points in the rotor, different configuration can be used. Currently there are two versions of PCB1, one with eight AD597 and one with six AD595, as shown in Figure 5-7. The circuit layout of a PCB1 with eight AD597 is depicted in Figure 5-8. Figure 5-9 shows front and back view of the PCB2. Almost all electronic elements are of type SMD (surface-mounted device), since they are light and experience relative low centrifugal forces. The circuit layout of PCB2 is shown in Figure 5-10. The layout of PCB2 is independent of PCB1. Practically a PCB1 with up to 12 thermocouple conditioners can be implemented and connected to PCB2 straightforward.

It should be noted here that for the validation process of the magnet temperature estimation procedures, PCB1 with high precision thermocouple conditioners of type AD595 is used. Therefore, as already mentioned, only six rotor temperature measuring points are considered in the validation process. The locations of the measuring points have been already given in Figure 4-6.

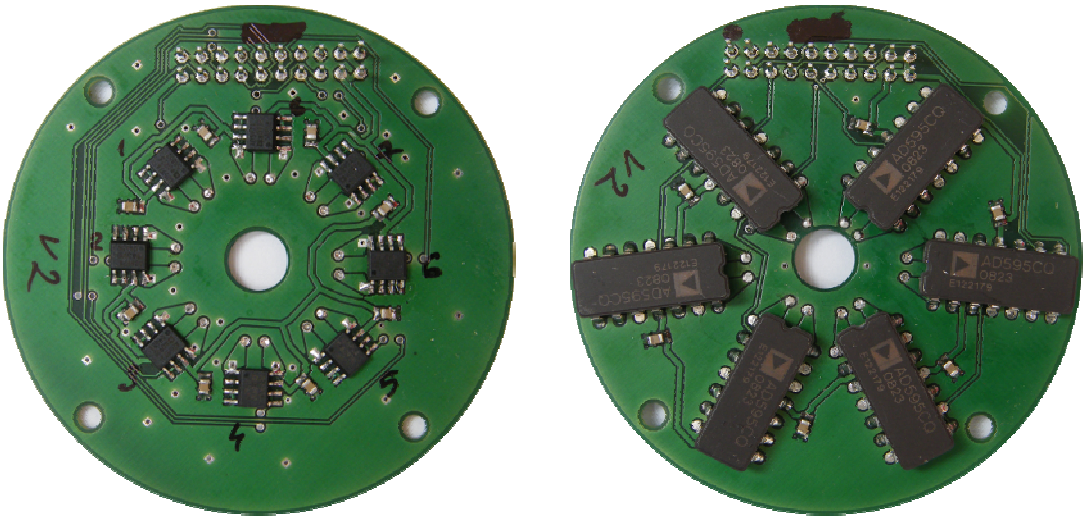

(a) (b)

Figure 5-7: PCB1 containing the thermocouple conditioner elements; front view: a) topology with eight thermocouple conditioners of type AD597; b) topology with six thermocouple conditioners of type AD595.

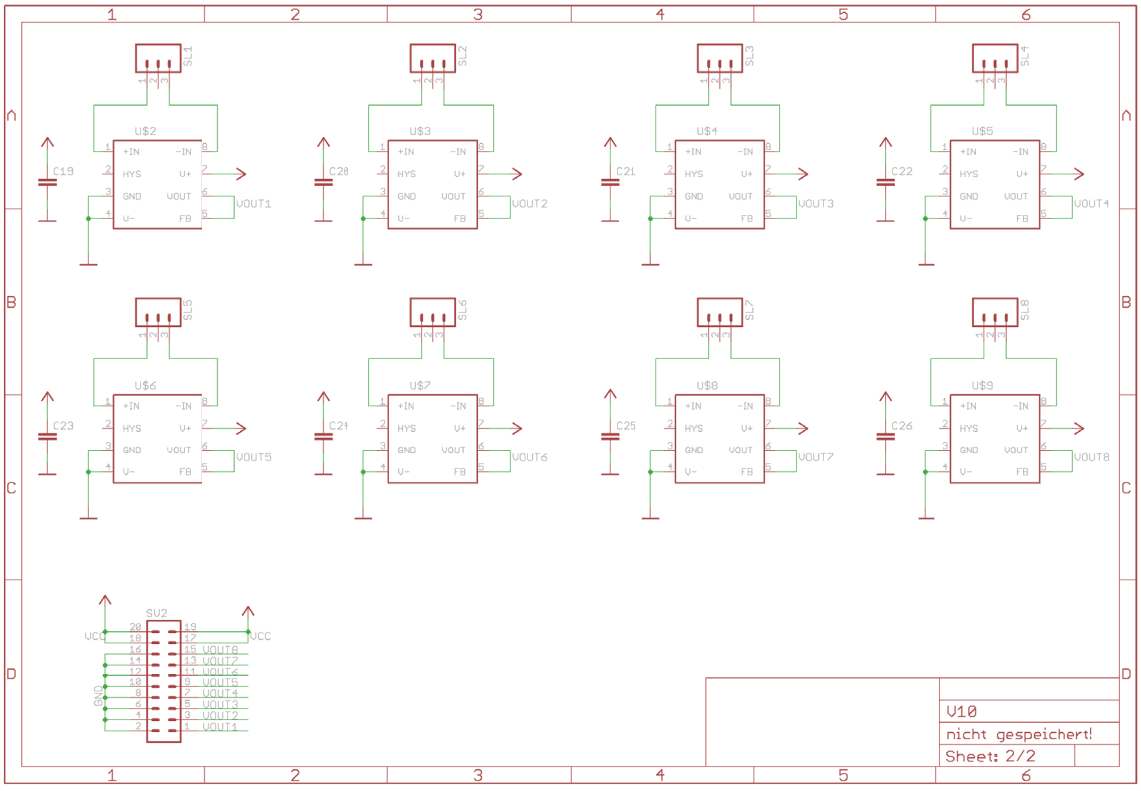

Figure 5-8: Circuit layout of PCB1 implying eight thermocouple conditioners of type AD597.

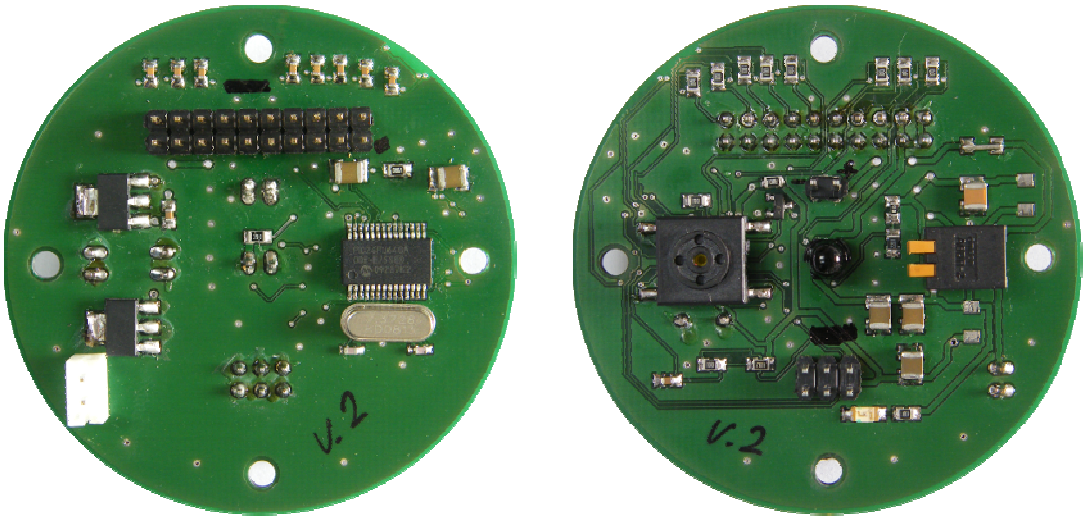

(a) (b)

Figure 5-9: PCB2 the microcontroller, the power electronic circuit, the infrared LED and its driver circuit: a) back view; b) front view with the infrared LED centred in the middle of the board.

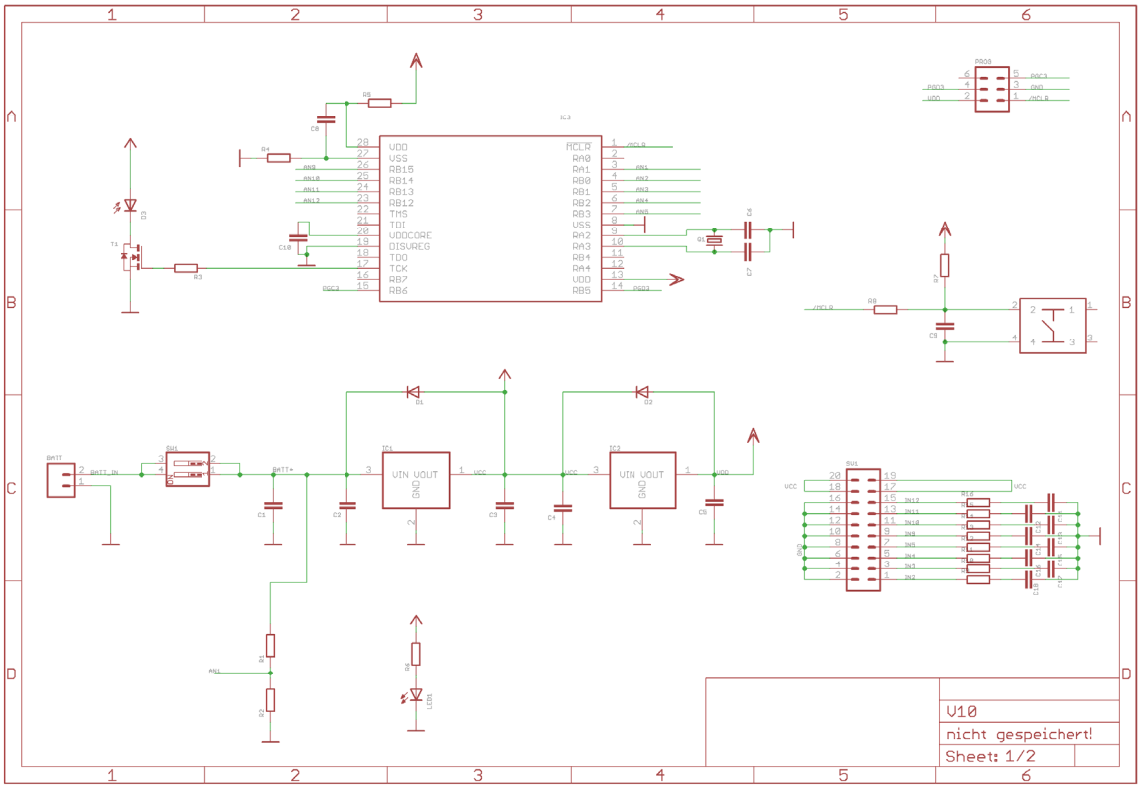

Figure 5-10: Circuit layout of PCB2.

The circuit of the rotating device is generally exposed to extreme electromagnetic hostile environment since the machine is driven by PWM controlled inverter with switching frequency of 20KHz. This is a general problem directly or indirectly reported in the majority of the works dealing with rotor temperature measuring issues. The signals are often so disturbed that only an average temperature value can be obtained. In the current design and implementation the following measures are taken that led to considerably stable and noise free temperature signals:

- The aluminium enclosure provides directly an electrostatic shield for the circuit.
- Thermocouple pairs of wire are twisted to ensure that both signals are equally affected by noise
- An electrical contact between the rotor and a thermocouple wire is avoided otherwise ground loops would introduce additional noise in the measured signal. The wires of the thermocouples are normally isolated but not the hot junction. Therefore, the hot junctions of the sensors are isolated here by applying a thin high temperature resistive silicon film.
- Analog filtering is applied to every signal. An analog low pass resistor capacitor (RC) filter is provided to the each ADC channel input pin of the microcontroller. It is demonstrated in Figure 5-11 that a sufficient dimensioning of the RC filters is required in order to obtain a stable temperature signal.

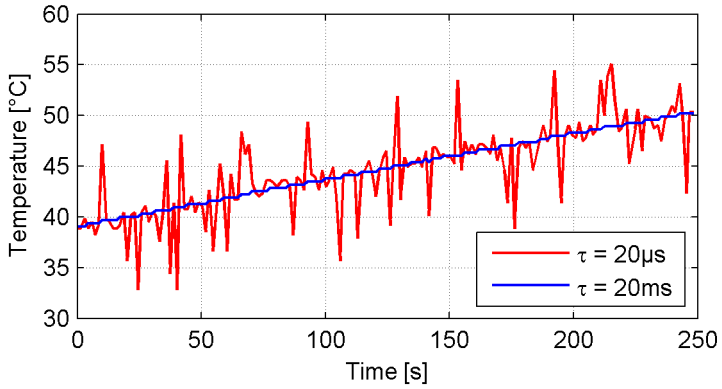

Figure 5-11: Rotor temperature signal measured with analog low pass RC filter with a time constant of 20µs and 20ms; inverter operation with PWM switching frequency of 20KHz.

The overall circuit of the rotating device is powered by a single PP3 9V battery. Since the nominal circuit current load is less than 33mA, an effective continuous operation of more than 30 hours can be guaranteed with a lithium power cell of 1200mA. The low power circuitry consumption is achieved by the use of thermocouples as temperature

sensors and the choice of a low power microcontroller with IrDA (Infrared Data Association) protocol support. The power saving effect resulting from the application of IrDA protocol in the optical data link and the applied data processing are explained next.

Data Processing and Optical Data Link

With respect to the transmission of the temperature values from the rotor to a stationary data processor (e.g. a host PC), there are three mostly applied approaches: slip rings, radio telemetry and light transmission. Measurements of rotor temperature through a slip ring assembly have been demonstrated in [27] and [28]. This strategy reveals several problems including limited number of rings, speed range for operation, electric noise and material compatibility, but positively needs minimum disassembly of the machine [91]. Radio telemetry has been proposed in [17] and [20], where wireless module operating at 433MHz carrier frequency has been used. Applications of data transmission by light are very successfully demonstrated in [16], [19], [21], [89]. Among all techniques, data transmission by light is characterized by highest reliability and noise immunity, and therefore, a strong preference to this strategy is given here as well.

In the current setup, the rotor temperature sensors are sampled every 100ms. The CPU processes the sample signals and makes a single data packet of 30bytes, as shown in Figure 5-12. The data packet is then moved to the UART (Universal Asynchronous Receiver Transmitter) module of the microcontroller. By means of an optical data link, the date packet is transmitted to a stationary receiver. It is only one way communication where the start and the stop codes provide synchronization with the stationary receiver system. Similar strategy has been reported in [89].

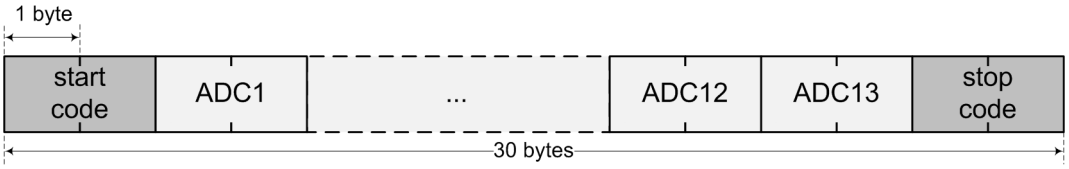

Figure 5-12: Data packet format.

The optical data link is realized by using an infrared LED which is connected the microcontroller UART output transmitter pin via a simple driver circuitry as shown in Figure 5-6. The infrared LED is centred on the PCB2, see Figure 5-9b. Apart from the 13 ADC internal channels, low power consumption, and very small size, the PIC24FJ microcontroller is considered here most suitable for this application as its UART

module supports IrDA data transmission protocol. The IrDA standard and protocols are described in detail in [93]. IrDA a packet of standards for various communication protocols highly optimized for infrared optical data links. In this particular application, IrDA SIR (Serial Infrared) is used, since it is already hardware implemented in the microcontroller UART module and satisfies fully the application requirements for low power infrared data link. Figure 5-13 demonstrates the principle of encoding a normal UART signal by the microcontroller UART module according to the IrDA SIR (Serial Infrared) scheme. Bit data of `1´ gets encoded as `0´. Bit data of `0´ gets encoded with `0´ for 7/16 bit width, followed by `1´ for 3/16 bit width and then again `0´ for 6/16 bit width. The use of IrDA SIR encoding scheme forces a significant shorter switch-on state for the LED per bit data transmission compared to a normal UART operating mode. In idle mode, i.e. no effective data transmission, the LED is in a continuous switched-off state. The result is a significant power saving effect since the infrared LED is one of the most power consuming electronic components of the device circuitry. This is an important aspect of the design as the rotating device is battery powered.

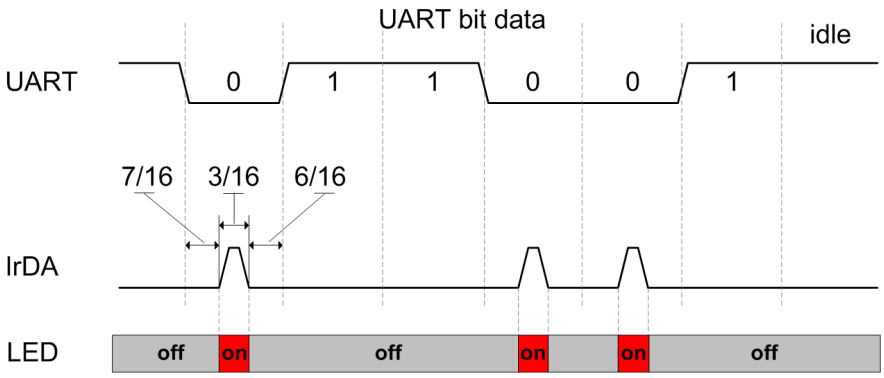

Figure 5-13: IrDA Serial Infrared (SIR) encoding scheme.

For successful infrared data communication between the rotating device and a host PC, the use of an IrDA compatible receiver/converter is mandatory. An IrDA receiver for a personal computer is easy to find as it is a market product offered by many computer peripherals vendors at relatively low price (usually about 20€). Normally an IrDA receiver has RS232 (or USB) interface that can be connected directly to the serial port of a host PC. The standardized wave length ranges between 850nm and 900nm and the radiation angle is maximum 30° at a distance of 3m. In this particular application, an infrared serial to RS232 converter from DeLock is used as receiver, see Figure 5-14. The UART module of the microcontroller should be set to the same baud rate as the receiver (9.6Kbit/s).

Figure 5-14: DeLock infrared serial to RS232 converter; source (www.delock.com).

In an experimental setup, the temperature signals transmitted from the rotating device to a host PC are real-time monitored on a Graphical User Interface (GUI), see Figure 5-6, and additionally stored with a time stamp for offline post-processing. Furthermore, the momentary battery state of charge of the rotating device is displayed continuously on the GUI. The GUI is programmed here using LabVIEW.

Mechanical Assembly

The PCB1 and PCB2 are fixated into two aluminium bodies separated by a plastic battery container. The assembly setup is demonstrated in Figure 5-15a. In case of monitoring machines with different diameter of the shaft, only the back aluminium body should be newly manufactured. This is the aluminium body enclosing the PCB1 with the thermocouple conditioners, as shown on the left picture of Figure 5-15b. This particular method of mounting requires a hole of around 5mm in the shaft. This leads the thermocouples from the rotor through to the instrumentation. From thermal point of view, the overall presented design foresees that the enclosure is completely mounted outside the motor so that the motor heat does not influence significantly the device circuitry.

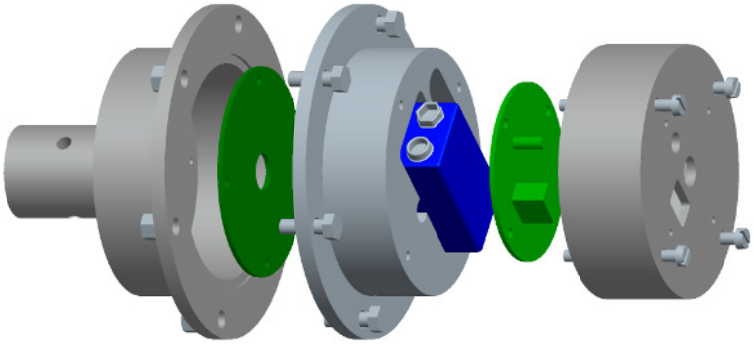

(a)

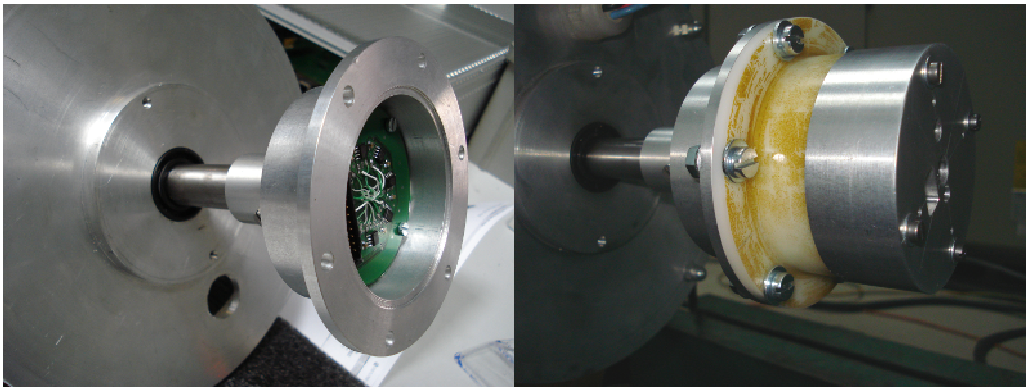

(b)

Figure 5-15: Mechanical assembly of the rotor temperature monitoring device: (a) 3D CAD view of the assembly parts; (b) photos of the device enclosure.

Accuracy

The device circuitry together with the thermocouples is calibrated using a high precision environmental chamber. As already mentioned, the used thermocouples are of tolerance class 1, which implies relative tolerance of ±0.36°C. Extensive test results of device functionality and accuracy are given in [13], [14]. An overall device accuracy of ±1°C could be estimated. Under uniform rotor temperature conditions, a maximum deviation between adjacent thermocouples of less than 1°C could be measured. Rotor temperature measurements, obtained upon heat-up tests of an induction motor and IPMSM, characterize with very high repetitiveness, [13], [14].

6 Conclusion

In the growing effort to look for better efficiency, increased reliability and cost optimization, the online temperature monitoring of the permanent magnets becomes an important diagnostic technique that should be strongly considered in modern PM electric drives. This is because the most widely used magnets in PM machines are Neodymium magnets and they are characterized with relatively low thermal stability expressed in two major magnetic properties. On the one hand, the remanence flux density of the magnet varies with the temperature, whereby reversible demagnetization effects occur while the magnet temperature increases. Thus, depending on the ambient temperature and the exact composite of the magnetic material, the rotor flux linkage in the motor can fluctuate up to 20% or even more under normal operating conditions and temperature range. This is particularly unfavourable fact which negatively influences constant torque control of PM machines. On the other hand the magnet intrinsic coercivity is a function of the temperature, whereby the absolute value decreases while the temperature increases. This means that, irreversible demagnetization of the magnet occurs at lower opposing external fields. Since theses two properties of the magnet are strongly related with its temperature, the magnet temperature is an inherent safety and control issue in electric drives based on PM machines. Therefore, in modern high performance PM electric drives it becomes essential in the control software to have an online feedback on the actual temperature of the magnets. The benefits are straightforward. In a motor torque control the degree of change of the rotor flux linkage due to temperature demagnetization effects can be online estimated and extra current can be applied on the machine terminals to compensate the fluctuation keeping a desired constant torque. In terms of safety operation, a magnet temperature monitoring increases the reliability and prolongs the life of the machine since it makes possible to avoid irreversible rotor demagnetization by hindering overloading of the machine while the magnet temperature is currently high.

Due to rotation, measuring directly the temperature of the magnets is inherently cumbersome task. There are many techniques applying different kind of sensors (infrared sensors and cameras, thermocouples, RTD, etc.). However, such techniques are characterized by significant additional costs, manufacturing and assembling efforts, which explains their low acceptance in industrial and end-user applications. Furthermore every additional sensor increases the risk of sensor failure resulting in reduced reliability of the electric drive.

With the clear objective to avoid direct temperature measurements in the rotor of a rotating machine, the presented work was set out to establish and validate the concept of a novel technique for online estimation of the magnet temperature in a PM machine without using any temperature sensors. The method exploits the actual problem faced in neodymium magnets, namely, the strong dependency of the magnetization level of the magnets from the temperature. The permanent magnets in a PM machine are normally cycled for the expected operating temperature range, which means that, within this temperature range the magnet flux density is a constant function of the magnet temperature (not necessarily linear). This implies that the rotor flux linkage is also a function of the magnet temperature. However, the rotor flux linkage influences the saturation level of the stator steel core of the machine, which in turn influences the stator inductances. Inherently, this influence is the strongest in the d-axis of the motor. Therefore the proposed method requires an application of a voltage pulse in the d-axis of the motor whereby the d-current response is measured and d-current slope is evaluated. In the analytical and experimental validation of the method it was demonstrated that, a change of the magnet temperature is reflected in the slope of the d-current response. Thus, it was found that, the degree of change of the d-current slope can be used as indicator for the degree of change of the magnet temperature. However, before a d-current slope can be unambiguously associated with a given temperature level of the permanent magnets, all other factors, that affect the d-current response of the machine upon a voltage pulse in the d-axis of the motor, should be considered and best possible eliminated or compensated. The current work demonstrated two successful compensation approaches that eliminate or reduce major factors influencing the d-current response and making variation in the d-current slope predominantly dependent of the magnet magnetization level and consequently its temperature. Thus, a speed compensation approach with zero load current was introduced whereby a combination of a positive and negative voltage pulse in the d-axis of the machine is used to eliminate undesired voltage terms in the d-axis of the machine as a result of the motor speed and the q-current developed along the pulse. By following analogical approach, magnet temperature estimation procedure under load conditions could be developed that compensate the influence of the q-current on the d-current response by eliminating undesired speed dependent voltage terms and reducing the effect of cross-coupling saturation effects. The obtained results proved that with the applied compensation approaches, the d-current slope can be successfully used as an indicator for the magnet temperature. It resulted to be indeed the most sensitive indicator reported so far in the literature. The experimental validation demonstrated that with the proposed method, an online estimation of the magnet temperature with accuracy down to only a few degrees

Celsius is possible for a wide motor speed range. Although predominantly tested on an interior permanent magnet synchronous machine, the proposed tuning and commissioning procedures of the method are valid and applicable for most types of PM machines.

From implementation point of view, a major advantage of the proposed magnet temperature monitoring is seen in the fact, that in an online mode the designated software routines only need the motor currents and the rotor position as feedback signals. Since these signals are typically available in a PM electric drive control scheme, there is no need for extra hardware. Thus, the range of the method applicability is very wide. The monitoring technique will bring the greatest benefits in PM electric drive systems operated under varying ambient temperature and harsh environmental conditions, such as wind turbines, hydro-generators, traction drives, pumps in the mining and oil industry, etc. It will increase the reliability and improve the exploitation capability of the machine by permitting secured overloading while machine operating points at risk of irreversible demagnetization can be identified and avoided by the control scheme. PM electric drives are widely used in electric and hybrid electric vehicles. Integration of a magnet temperature monitoring in such control applications will help to achieve constant torque control since the degree of change in the rotor magnetization can be detected in online mode and compensated by the current controller. This will give the car driver a better feeling for a constant vehicle driving performance at all conditions.

The method relies on detection of saturation drop in the steel stator core as a consequence of demagnetization effects in the magnets due to the temperature. Thus, occurrence of permanent partial demagnetization due to mechanical factors (chopped magnets, corrosion, etc) will lead to erroneous temperature estimation, whereby a new calibration of the temperature estimation procedure will be necessary. In order to detect such cases, the author recommends the use of a combination of techniques. For example, the proposed method can be combined with a parallel running magnet temperature monitoring either based on flux observer or on a thermal model of the machine.

In this work, several factors were neglected which can be investigated in future research activities. For example, the method validation was carried out assuming uniform temperature distribution of the magnets. Depending on the size of the magnets, segmentation and the motor operating point, the temperature along a permanent magnet is not always constant. Eddy currents in the magnet can cause uneven momentary temperature values along its surface and volume. However, such investigation would

require much more sophisticated experimental setups where the temperature differences along the magnet surface must be directly measured. Furthermore, saturation effects due to eddy currents in the steel stator core were neglected too. Investigation considering the eddy currents as a function of the stator temperature can be made a subject for ongoing research in order to improve the method performance. Further performance boost can be achieved by considering the influence of the stator winding resistance voltage drop on the d-current response, as this was also neglected in this work. The stator winding resistance varies with the temperature. A compensation of this voltage will require online temperature measurements of the stator windings. However, this should not be an obstacle since modern machines are normally equipped with temperature sensors in the stator.

Appendix A - List of Symbols

B	flux density
B_r	remanent flux density; remanence
B_i	intrinsic flux density
H	magnetizing force
H_c	coercive magnetizing force; coercivity
H_{ci}	intrinsic coercivity
P_c	permeance coefficient
F	magnetomotive force; m.m.f.
i_a, i_b, i_c	motor phase stator currents
u_a, u_b, u_c	motor phase stator voltages
$\underline{a}$	special operator $e^{j2\pi/3}$
$\underline{i_s}$	current stator space vector
$\underline{i_s^s}$	current stator space vector expressed in the stator oriented reference frame
$\underline{i_s^r}$	current stator space vector expressed in the rotor oriented reference frame
$\underline{u_s}$	voltage stator space vector
$\underline{u_s^s}$	voltage stator space vector expressed in the stator oriented reference frame
$\underline{u_s^r}$	voltage stator space vector expressed in the rotor oriented reference frame
α, β	real and imaginary axis denomination of the stator oriented reference frame

d, q	real and imaginary axis denomination of the rotor oriented reference frame
i_α, i_β	real and imaginary component of the current space vector in the stator oriented reference frame
i_d, i_q	real and imaginary component of the current space vector in the rotor oriented reference frame
u_α, u_β	real and imaginary component of the voltage space vector in the stator oriented reference frame
u_d, u_q	real and imaginary component of the voltage space vector in the rotor oriented reference frame
θ	angle between stator and rotor oriented reference frames measured in electrical degrees
θ_r	mechanical rotor position measured in mechanical degrees
ω	angular speed between the stator and rotor oriented reference frames
P	number of pole pairs
ψ_m	magnetizing flux linkage
ψ_M	flux linkage produced by the permanent magnets
$\underline{\psi}_s^s$	stator flux linkage space vector expressed in the stator oriented reference frame
$\underline{\psi}_s^r$	stator flux linkage space vector expressed in the rotor oriented reference frame
ψ_d, ψ_q	real and imaginary component of the stator flux linkage space vector expressed in the rotor oriented reference frame
R_s	stator winding resistance
L_s	stator inductance
L_d	absolute motor inductance in the d-axis of a machine

L_q	absolute motor inductance in the q-axis of a machine
L^*	differential inductance
t_e	electromagnetic torque
T_m	magnet temperature
S_a	approximated d-current slope using polynomial interpolation
i_{dP}	d-current response upon a positive voltage pulse in the d-axis of the machine
i_{dN}	d-current response upon a negative voltage pulse in the d-axis of the machine
i_{qP}	q-current response upon a positive voltage pulse in the d-axis of the machine
i_{qN}	q-current response upon a negative voltage pulse in the d-axis of the machine
p_0	beginning of a voltage pulse switching command; beginning of an idle pulse
p_1	end of a voltage pulse switching command; end of an idle pulse
t_{resp}	current sensor response time
$t_{d(on)}$	transistor turn-on propagation time
$t_{d(off)}$	transistor turn-off propagation time
t_{DT}	inverter switching command dead time defined by the controller
t_{d1}	signal propagation delay time as a result of the applied circuitry between the controller and the PWM inverter input interface
t_{td}	total delay time between the beginning of the pulse switching command and the beginning of the effective voltage pulse in the machine

t_{pw}	voltage pulse width as defined by the controller switching commands
$t_{pw(eff)}$	effective voltage pulse width applied on the machine terminals
PWM_{prd}	Pulse Width Modulation Period
V_{dc}	Inverter dc link voltage

Appendix B - Abbreviations

PMSM	Permanent Magnet Synchronous Motor
SPMSM	Surface Permanent Magnet Synchronous Motor
IPMSM	Interior Permanent Magnet Synchronous Motor
IM	Induction Machine
PM	Permanent Magnet
PM machine	machine with permanent magnet excitation
a.c. machine	alternate current machine
E&HEV	Electric and Hybrid Electric Vehicles
PWM	Pulse Width Modulation
SVPWM	Space Vector Pulse Width Modulation
FOC	Field Oriented Control
SVFOC	Space Vector Field Oriented Control
CGS	Centimetre Gram Second (unit system)
m.m.f	magnetomotive force
PC	Personal Computer
GUI	Graphical User Interface
MCU	Motor Control Unit
FPGA	Field Programmable Gate Array
ADC	Analog Digital Converter
DMA	Direct Memory Access controller
EMIF	External Memory Interface

CAP	Capture Compare Unit
IGBT	Insulated-Gate Bipolar Transistors
PCB	Printed Circuit Board
LED	Light Emitting Diode
UART	Universal Asynchronous Receiver Transmitter
IrDA	Infrared Data Association
IrDA SIR	IrDA Serial Infrared data protocol

Appendix C - Paper Award

An IEEE Committee Prize Paper Award was received on November 11, 2013, in Vienna during the 39th IECON for the paper "Sensorless rotor temperature estimation of permanent magnet synchronous motor under load conditions", [82]. The paper was presented at the 38th IECON October 25-28, 2012, in Montreal. The content of the paper is a concise presentation of section 4.5 of the current thesis.

IEEE

Committee Prize Paper Award

The Electric Machines Technical Committee of the IEEE Industrial Electronics Society recognizes

Martin Ganchev, Christian Kral, Thomas Wolbank

with this Paper Award, Second Prize, for the technical competence displayed in the paper entitled:

Sensorless Rotor Temperature Estimation of Permanent Magnet Synchronous Motor under Load Conditions

presented at the 38rd IECON, October 25 – 28, 2012, Montréal, Canada

EMTC chairman

Prof. Andrea Cavagnino

IES President

Prof. Gerard André Capolino

References

[1] P. Waide and C. U. Brunner, “Energy-Efficiency Policy Opportunities for Electric Motor-Driven Systems,” 2011. [Online]. Available: www.iea.org. [Accessed: 13-Jul-2012].

[2] J. Puranen, “Induction Motor Versus Permanent Magnet Synchronous Motor In Motion Control Applications: A Comparative Study,” University Lappeenranta, 2006.

[3] J. D. Ede, K. Atallah, G. W. Jewell, J. B. Wang, and D. Howe, “Effect of Axial Segmentation of Permanent Magnets on Rotor Loss in Modular Permanent-Magnet Brushless Machines,” *IEEE Trans. Ind. Appl.*, vol. 43, no. 5, pp. 1207–1213, 2007.

[4] A. Fukuma, S. Kanazawa, D. Miyagi, and N. Takahashi, “Investigation of AC loss of permanent magnet of SPM motor considering hysteresis and eddy-current losses,” *IEEE Trans. Magn.*, vol. 41, no. 5, pp. 1964–1967, 2005.

[5] M. Kamiya, Y. Kawase, T. Kosaka, and N. Matsui, “Temperature distribution analysis of permanent magnet in interior permanent magnet synchronous motor considering pwm carrier harmonics,” *Electr. Mach. Syst. 2007. ICEMS. Int. Conf.*, pp. 2023–2027, 2007.

[6] D. A. Stone, P. H. Mellor, D. Howe, and K. Atallah, “Rotor loss in permanent-magnet brushless AC machines,” *IEEE Trans. Ind. Appl.*, vol. 36, no. 6, pp. 1612–1618, 2000.

[7] K. Yamazaki and A. Abe, “Loss Investigation of Interior Permanent-Magnet Motors Considering Carrier Harmonics and Magnet Eddy Currents,” *IEEE Trans. Ind. Appl.*, vol. 45, no. 2, pp. 659–665, 2009.

[8] K. Yamazaki, Y. Kanou, Y. Fukushima, S. Ohki, A. Nezu, T. Ikemi, and R. Mizokami, “Reduction of Magnet Eddy-Current Loss in Interior Permanent-Magnet Motors With Concentrated Windings,” *IEEE Trans. Ind. Appl.*, vol. 46, no. 6, pp. 2434–2441, Nov. 2010.

[9] K. Yamazaki, M. Shina, Y. Kanou, M. Miwa, and J. Hagiwara, “Effect of Eddy Current Loss Reduction by Segmentation of Magnets in Synchronous Motors: Difference Between Interior and Surface Types,” *IEEE Trans. Magn.*, vol. 45, no. 10, pp. 4756–4759, 2009.

[10] K. Yoshida, Y. Hita, and K. Kesamaru, “Eddy-current loss analysis in PM of surface-mounted-PM SM for electric vehicles,” *IEEE Trans. Magn.*, vol. 36, no. 4, pp. 1941–1944, 2000.

[11] T. Sebastian, “Temperature effects on torque production and efficiency of PM motors using NdFeB magnets,” *IEEE Trans. Ind. Appl.*, vol. 31, no. 2, pp. 353–357, 1995.

[12] J. Jae-Woo, L. Sang-Ho, H. Jung-Pyo, K. Ki-Nam, C. Hyoung-Jun, and M. Sang-Hoon, “Optimum design for eddy current reduction in permanent magnet to prevent irreversible demagnetization,” *Electr. Mach. Syst. 2007. ICEMS. Int. Conf.*, pp. 949–954, 2007.

[13] M. Ganchev, H. Umschaden, and H. Kappeler, “Rotor temperature distribution measuring system,” in *IECON 2011 - 37th Annual Conference of the IEEE Industrial Electronics Society*, 2011, pp. 2006–2011.

[14] M. Ganchev, B. Kubicek, and H. Kappeler, “Rotor temperature monitoring system,” in *The XIX International Conference on Electrical Machines - ICEM 2010*, 2010, pp. 1–5.

[15] R. Beguenane and M. E. H. Benbouzid, “Induction motors thermal monitoring by means of rotor resistance identification,” *IEEE Trans. Energy Convers.*, vol. 14, no. 3, pp. 566–570, 1999.

[16] H. Yahoui and G. Grellet, “Measurement of physical signals in rotating part of electrical machine by means of optical fibre transmission,” *Qual. Meas. Indispens. Bridg. between Theory Real. (No Meas. No Sci. Jt. Conf. - 1996 IEEE Instrum. Meas. Technol. Conf. IMEKO Tech. Comm. 7. Conf. Proc.*, pp. 591–596, 1996.

[17] Z. Hou and G. Gu, “Wireless rotor temperature measurement system based on MSP430 and nRF401,” *Electr. Mach. Syst. 2008. ICEMS 2008. Int. Conf.*, pp. 858–861, 2008.

[18] X. Xue, V. Sundararajan, and W. P. Brithinee, “The application of wireless sensor networks for condition monitoring in three-phase induction motors,” *2007 Electr. Insul. Conf. Electr. Manuf. Expo*, pp. 445–448, 2007.

[19] H. Hafezi and A. Jalilian, “Design and Construction of Induction Motor Thermal Monitoring System,” *Proc. 41st Int. Univ. Power Eng. Conf.*, pp. 674–678, Sep. 2006.

[20] G. Jianzhong, G. Hui, and H. Zhe, “Rotor temperature monitoring technology of direct-drive permanent magnet wind turbine,” *2009 Int. Conf. Electr. Mach. Syst.*, pp. 1–4, Nov. 2009.

[21] Z. Lazarevic, R. Radosavljevic, and P. Osmokrovic, “A new thermal observer for squirrel-cage induction motor,” *Qual. Meas. Indispens. Bridg. between Theory Real. (No Meas. No Sci. Jt. Conf. - 1996 IEEE Instrum. Meas. Technol. Conf. IMEKO Tech. Comm. 7. Conf. Proc.*, pp. 610–613, 1996.

[22] M. Kovacic, M. Vrazic, and I. Gasparac, “Bluetooth wireless communication and 1-wire digital temperature sensors in synchronous machine rotor temperature measurement,” in *Proceedings of 14th International Power Electronics and Motion Control Conference EPE-PEMC 2010*, 2010.

[23] C. Kral, A. Haumer, M. Haigis, H. Lang, and H. Kapeller, “Comparison of a CFD Analysis and a Thermal Equivalent Circuit Model of a TEFC Induction Machine With Measurements,” *IEEE Trans. Energy Convers.*, vol. 24, no. 4, pp. 809–818, 2009.

[24] S. Stipetic, M. Kovacic, Z. Hanic, and M. Vrazic, “Measurement of Excitation Winding Temperature on Synchronous Generator in Rotation Using Infrared Thermography,” *IEEE Trans. Ind. Electron.*, vol. 59, no. 5, pp. 2288–2298, 2012.

[25] D. D. Reigosa, F. Briz, P. Garcia, J. M. Guerrero, and M. W. Degner, “Magnet Temperature Estimation in Surface PM Machines Using High-Frequency Signal Injection,” *IEEE Trans. Ind. Appl.*, vol. 46, no. 4, pp. 1468–1475, 2010.

[26] D. Reigosa, F. Briz, P. Garcia-Fernandez, J. M. Guerrero, and M. Degner, “Magnet temperature estimation in surface PM machines during Six-step Operation,” *IEEE Trans. Ind. Appl.*, p. 1, 2012.

[27] C. Mejuto, M. Mueller, M. Shanel, A. Mebarki, M. Reekie, and D. Staton, “Improved synchronous machine thermal modelling,” *2008 18th Int. Conf. Electr. Mach.*, pp. 1–6, Sep. 2008.

[28] W. T. Martiny, R. M. McCoy, and H. B. Margolis, “Thermal Relationships in an Induction Motor under Normal and Abnormal Operation,” *Trans. Am. Inst. Electr. Eng. Part III Power Appar. Syst.*, vol. 80, no. 3, pp. 66–76, Apr. 1961.

[29] E. Odvářka, N. L. Brown, A. Mebarki, M. Shanel, S. Narayanan, and C. Ondrůšek, “Thermal modelling of water-cooled axial-flux permanent magnet machine,” in *5th IET International Conference on Power Electronics, Machines and Drives (PEMD 2010)*, 2010, pp. TU414–TU414.

[30] Y. Chun, W. Keyin, and W. Xiaonian, “Coupled-field thermal analysis of high-speed permanent magnetic generator applied in micro-turbine generator,” in *2005 International Conference on Electrical Machines and Systems*, 2005, pp. 2458–2461 Vol. 3.

[31] A. Boglietti, A. Cavagnino, and D. Staton, “Determination of Critical Parameters in Electrical Machine Thermal Models,” *IEEE Trans. Ind. Appl.*, vol. 44, no. 4, pp. 1150–1159, 2008.

[32] A. Boglietti, A. Cavagnino, D. Staton, M. Shanel, M. Mueller, and C. Mejuto, "Evolution and Modern Approaches for Thermal Analysis of Electrical Machines," *IEEE Trans. Ind. Electron.*, vol. 56, no. 3, pp. 871–882, 2009.

[33] C. H. Lim, J. R. Bumby, R. G. Dominy, G. I. Ingram, K. Mahkamov, N. L. Brown, A. Mebarki, and M. Shanel, "2-D lumped-parameter thermal modelling of axial flux permanent magnet generators," in *2008 18th International Conference on Electrical Machines*, 2008, pp. 1–6.

[34] C. Jungreuthmayer, T. Bauml, O. Winter, M. Ganchev, H. Kapeller, A. Haumer, and C. Kral, "A Detailed Heat and Fluid Flow Analysis of an Internal Permanent Magnet Synchronous Machine by Means of Computational Fluid Dynamics," *IEEE Trans. Ind. Electron.*, vol. 59, no. 12, pp. 4568–4578, 2012.

[35] T. Bauml, C. Jungreuthmayer, and C. Kral, "An innovative parametrization method for a thermal equivalent circuit model of an interior permanent magnet synchronous machine," in *IECON 2011 - 37th Annual Conference of the IEEE Industrial Electronics Society*, 2011, pp. 1746–1751.

[36] B.-H. Lee, K.-S. Kim, J.-W. Jung, J.-P. Hong, and Y.-K. Kim, "Temperature Estimation of IPMSM Using Thermal Equivalent Circuit," *IEEE Trans. Magn.*, vol. 48, no. 11, pp. 2949–2952, Nov. 2012.

[37] R. Wrobel, P. H. Mellor, and D. Holliday, "Thermal Modeling of a Segmented Stator Winding Design," *IEEE Trans. Ind. Appl.*, vol. 47, no. 5, pp. 2023–2030, Sep. 2011.

[38] D. M. Ionel, M. Popescu, M. I. McGilp, T. J. E. Miller, S. J. Dellinger, and R. J. Heideman, "Computation of Core Losses in Electrical Machines Using Improved Models for Laminated Steel," *IEEE Trans. Ind. Appl.*, vol. 43, no. 6, pp. 1554–1564, 2007.

[39] D. M. Ionel and M. Popescu, "Finite-Element Surrogate Model for Electric Machines With Revolving Field—Application to IPM Motors," *IEEE Trans. Ind. Appl.*, vol. 46, no. 6, pp. 2424–2433, Nov. 2010.

[40] P. Milanfar and J. H. Lang, "Monitoring the thermal condition of permanent-magnet synchronous motors," *IEEE Trans. Aerosp. Electron. Syst.*, vol. 32, no. 4, pp. 1421–1429, 1996.

[41] G. D. Demetriades, H. Z. D. La Parra, E. Andersson, and H. Olsson, "A Real-Time Thermal Model of a Permanent-Magnet Synchronous Motor," *IEEE Trans. Power Electron.*, vol. 25, no. 2, pp. 463–474, 2010.

[42] A. Specht and J. Bocker, “Observer for the rotor temperature of IPMSM,” in *Proceedings of 14th International Power Electronics and Motion Control Conference EPE-PEMC 2010*, 2010.

[43] X. Xi, C. Changming, and Z. Meng, “Dynamic Permanent Magnet Flux Estimation of Permanent Magnet Synchronous Machines,” *IEEE Trans. Appl. Supercond.*, vol. 20, no. 3, pp. 1085–1088, 2010.

[44] R. J. Parker, *Advances in Permanent Magnetism*. Wiley, 1990.

[45] R. J. Parker, “Permanent Magnet Guidelines,” *MAGNETIC MATERIAL PRODUCERS ASSOCIATION*, 1998. [Online]. Available: www.intemag.com/pdf/MMPAPMG-88.pdf. [Accessed: 09-Jan-2013].

[46] P. Campbell, *Permanent magnet materials and their application*. Cambridge University Press, 1996.

[47] Arnold, “Temperature Effects on Magnet Output,” *TN 0303 June 2003*, 2003. [Online]. Available: www.arnoldmagnetics.com. [Accessed: 15-Jan-2013].

[48] Magkraft, “Magkraft,” 2013. [Online]. Available: http://www.rare-earth-magnets.com/c-4-neodymium-magnets.aspx. [Accessed: 16-Jan-2013].

[49] A. LLC, “Magnet Guide & Tutorial,” *www.Allianceorg.com*. [Online]. Available: http://www.allianceorg.com/pdfs/Magnet_Tutorial_v85_1.pdf. [Accessed: 14-Jan-2013].

[50] M. H. Wlmer, J. F. Liu, and P. C. Dent, “Current Status of Permanent Magnet Industry in the United States,” in *Proceedings of 20th International Workshop on Rare Earth Permanent Magnets and Their Applications*, 2008, vol. 2, pp. 1–6.

[51] S. Constantinides and D. Gulick, “NdFeB for High Temperature Motor Applications,” *www.arnoldmagnetics.com, SMMA Fall Technical Conference*, 2004. [Online]. Available: http://www.arnoldmagnetics.com/Technical_Papers_and_Presentations.aspx. [Accessed: 18-Jan-2013].

[52] “Magnaworks Technology.” [Online]. Available: http://www.magnaworkstechnology.com/. [Accessed: 15-Jan-2013].

[53] http://www.advancedmagnetsource.com, “Magnetic Characteristics SmCo5 / Sm2Co17.” [Online]. Available: http://www.advancedmagnetsource.com/SmCo.pdf. [Accessed: 17-Jan-2013].

[54] Magnetic-Materials-Producers-Association, “Standard Specifications for Permanent Magnet Materials,” *MMPA STANDARD*. [Online]. Available: http://www.magnetsim.com/mmpa_standards.php?menu_id=30. [Accessed: 17-Jan-2013].

[55] B. S. Constantinides, “A Manufacturing and Performance Comparison Between Bonded and Sintered Permanent Magnets,” *Arnold Magnetic Technologies*, 2006. [Online]. Available: http://www.arnoldmagnetics.com/.

[56] S. Constantinides, “Magnet Selection,” 2003. [Online]. Available: http://www.arnoldmagnetics.com/.

[57] S. Kozawa, “Trends and Problems in Research of Permanent Magnets for Motors,” *Sci. Technol. Trends*, vol. September, pp. 40–54, 2010.

[58] P. Vas, *Vector control of AC machines*. Clarendon Press, 1990.

[59] P. Vas, *Electrical Machines and Drives: Space Vector Theory Approach*. O.U.P., 1992.

[60] P. Vas, *Sensorless vector and direct torque control*. Oxford University Press, 1998.

[61] R. H. Park, “Two-reaction theory of synchronous machines generalized method of analysis-part I,” *Trans. Am. Inst. Electr. Eng.*, vol. 48, no. 3, pp. 716–727, Jul. 1929.

[62] B. Sneyers, D. W. Novotny, and T. A. Lipo, “Field Weakening in Buried Permanent Magnet AC Motor Drives,” *IEEE Trans. Ind. Appl.*, vol. IA-21, no. 2, pp. 398–407, Mar. 1985.

[63] A. Consoli and A. Abela, “Transient Performance of Permanent Magnet AC Motor Drives,” *IEEE Trans. Ind. Appl.*, vol. IA-22, no. 1, pp. 32–41, Jan. 1986.

[64] S. Ebersberger and B. Piepenbreier, “Identification of differential inductances of permanent magnet synchronous machines using test current signal injection,” in *International Symposium on Power Electronics Power Electronics, Electrical Drives, Automation and Motion*, 2012, pp. 1342–1347.

[65] M. Ganchev, “Design and Implementation of an Operating System for the TMS320C6713 DSP Used in Motor Test Unit for Monitoring and Controlling Both Permanent Magnet Synchronous and Induction Motors,” Diploma Thesis at the Institute of Energy Systems and Electric Drives, Vienna University of Technology, 2005.

[66] A. Yoo and S.-K. Sul, “Design of Flux Observer Robust to Interior Permanent-Magnet Synchronous Motor Flux Variation,” *IEEE Trans. Ind. Appl.*, vol. 45, no. 5, pp. 1670–1677, 2009.

[67] G. Wang, Z. Li, G. Zhang, Y. Yu, and D. Xu, “Quadrature PLL-Based High-Order Sliding-Mode Observer for IPMSM Sensorless Control With Online MTPA Control Strategy,” *IEEE Trans. Energy Convers.*, vol. 28, no. 1, pp. 214–224, Mar. 2013.

[68] Y. A.-R. I. Mohamed and T. K. Lee, “Adaptive Self-Tuning MTPA Vector Controller for IPMSM Drive System,” *IEEE Trans. Energy Convers.*, vol. 21, no. 3, pp. 636–644, Sep. 2006.

[69] M. N. Uddin and M. A. Rahman, “High-Speed Control of IPMSM Drives Using Improved Fuzzy Logic Algorithms,” *IEEE Trans. Ind. Electron.*, vol. 54, no. 1, pp. 190–199, Feb. 2007.

[70] C. B. Butt, M. A. Hoque, and M. A. Rahman, “Simplified Fuzzy-Logic-Based MTPA Speed Control of IPMSM Drive,” *IEEE Trans. Ind. Appl.*, vol. 40, no. 6, pp. 1529–1535, Nov. 2004.

[71] S. Kim, Y.-D. Yoon, S.-K. Sul, and K. Ide, “Maximum Torque per Ampere (MTPA) Control of an IPM Machine Based on Signal Injection Considering Inductance Saturation,” *IEEE Trans. Power Electron.*, vol. 28, no. 1, pp. 488–497, Jan. 2013.

[72] C.-T. Pan and S.-M. Sue, “A Linear Maximum Torque Per Ampere Control for IPMSM Drives Over Full-Speed Range,” *IEEE Trans. Energy Convers.*, vol. 20, no. 2, pp. 359–366, Jun. 2005.

[73] A. Consoli, G. Scarcella, G. Scelba, and A. Testa, “Steady-State and Transient Operation of IPMSMs Under Maximum-Torque-per-Ampere Control,” *IEEE Trans. Ind. Appl.*, vol. 46, no. 1, pp. 121–129, 2010.

[74] H. A. Toliyat and S. G. Campbell, *Dsp-Based Electromechanical Motion Control*. CRC PressINC, 2004.

[75] Semikron, “Modules – Explanations – SKiiP,” 2007. [Online]. Available: http://www.semikron.com/skcompub/ko/skiip_complete_data_sheet.pdf. [Accessed: 24-Aug-2013].

[76] Semikron, “SKiiP 132GD120-3DU INTEGRATED - Datasheet,” 2007. [Online]. Available: http://www.datasheet4u.com/datasheet/S/K/I/SKIIP132GD120-3DU_SemikronInternational.pdf.html. [Accessed: 24-Aug-2013].

[77] ON Semiconductor, “MC34151, MC33151 High Speed Dual MOSFET Drivers - Data Sheet,” 2013. [Online]. Available: http://www.onsemi.com. [Accessed: 04-Sep-2013].

[78] Ratioplast-Optoelectronics GmbH, “T05 SE 660 KR 001 Phopto-Klemme 660nm Sender - Data Sheet,” 2013. [Online]. Available: http://www.ratioplast.com. [Accessed: 04-Sep-2013].

[79] Ratioplast-Optoelectronics GmbH, “T05 EM 660 KR 001 Photo-Empfänger 660nm 5MBit/s - Data Sheet,” 2013. [Online]. Available: http://www.ratioplast.com. [Accessed: 04-Sep-2013].

[80] M. Ganchev, C. Kral, and T. Wolbank, “Compensation of speed dependency in sensorless rotor temperature estimation for permanent magnet synchronous motor,” in *2012 XXth International Conference on Electrical Machines*, 2012, pp. 1612–1618.

[81] M. Ganchev, C. Kral, and T. M. Wolbank, “Compensation of Speed Dependence in Sensorless Rotor Temperature Estimation for Permanent-Magnet Synchronous Motor,” *IEEE Trans. Ind. Appl.*, vol. 49, no. 6, pp. 2487–2495, Nov. 2013.

[82] M. Ganchev, C. Kral, and T. Wolbank, “Sensorless rotor temperature estimation of permanent magnet synchronous motor under load conditions,” in *IECON 2012 - 38th Annual Conference on IEEE Industrial Electronics Society - (the paper received the Second Prize Paper Award of the Electrical Machines Technical Committee of the IEEE Industrial Electronics Society)*, 2012, pp. 1999–2004.

[83] M. Ganchev, C. Kral, and T. Wolbank, “Hardware and software implementation of sensorless rotor temperature estimation technique for Permanent Magnet Synchronous Motor,” in *2012 Electrical Systems for Aircraft, Railway and Ship Propulsion*, 2012, pp. 1–6.

[84] Emanuel Aichhorn, “Development of a new trigger & read procedure for the ADS8422 ADC based on the EDMA3 controller of the C6747 microcontroller,” Diploma Thesis, University of Applied Sciences Technikum Wien, 2010.

[85] T. M. Wolbank, J. L. Machl, and H. Hauser, “Closed-Loop Compensating Sensors Versus New Current Derivative Sensors for Shaft-Sensorless Control of Inverter Fed Induction Machines,” *IEEE Trans. Instrum. Meas.*, vol. 53, no. 4, pp. 1311–1315, Aug. 2004.

[86] M. A. Vogelsberger, S. Grubic, T. G. Habetler, and T. M. Wolbank, “Using PWM-Induced Transient Excitation and Advanced Signal Processing for Zero-Speed

Sensorless Control of AC Machines," *IEEE Trans. Ind. Electron.*, vol. 57, no. 1, pp. 365–374, Jan. 2010.

[87] T. M. Wolbank, J. L. Machl, and H. Hauser, "Prediction and measurements of a current derivative sensor response for voltage pulses applied to induction machines," *J. Appl. Phys.*, vol. 93, no. 10, p. 6656, 2003.

[88] R. Leidhold, "Position Sensorless Control of PM Synchronous Motors Based on Zero-Sequence Carrier Injection," *IEEE Trans. Ind. Electron.*, vol. 58, no. 12, pp. 5371–5379, Dec. 2011.

[89] D. J. T. Siyambalapitiya, P. G. McLaren, and P. P. Acarnley, "A Rotor Condition Monitor for Squirrel-Cage Induction Machines," *IEEE Trans. Ind. Appl.*, vol. IA-23, no. 2, pp. 334–340, 1987.

[90] Z. Lazarevic, R. Radosavljevic, and P. Osmokrovic, "A novel approach for temperature estimation in squirrel-cage induction motor without sensors," *IEEE Trans. Instrum. Meas.*, vol. 48, no. 3, pp. 753–757, 1999.

[91] J. Dymond, R. Ong, and N. Stranges, "Instrumentation, testing and analysis of electric machine rotor steady-state heating," *Rec. Conf. Pap. IEEE Inc. Ind. Appl. Soc. Forty-Eighth Annu. Conf. 2001 Pet. Chem. Ind. Tech. Conf. (Cat. No.01CH37265)*, pp. 297–303, 2001.

[92] M. Ganchev, H. Umschaden, and H. Kappeler, "Sistema de medição da temperatura de rotores," *Electr. Mod. (EM), Bras.*, vol. 445, pp. 140–145, 2011.

[93] C. D. Knutson and J. M. Brown, *IrDA Principles and Protocols: The IrDA Library. Volume 1*. MCL Press, 2004.